NANOWIRE QUANTUM DOT PHOTODETECTORS

NANOWIRE QUANTUM DOT PHOTODETECTORS

By

PAUL KUYANOV, B.Eng,

A Thesis Submitted to the School of Graduate Studies in Partial Fulfillment of the Requirements for the Degree Doctor of Philosophy

McMaster University

Doctor of Philosophy (2017) McMaster University
(Department of Engineering Physics) Hamilton, Ontario

TITLE: Nanowire Quantum Dot Photodetectors

AUTHOR: Paul Kuyanov, B.Eng, (McMaster University)

SUPERVISOR: Dr. Ray R. LaPierre

Abstract

InAs/GaAs quantum dots (QDs) embedded within InP/GaP nanowires (NWs) were grown on Si substrates by Au-assisted and self-assisted vapor-liquid-solid (VLS) growth using molecular beam epitaxy (MBE). The morphology and structure of the NWs was characterized using scanning electron microscopy (SEM) and transmission electron microscopy (TEM). The samples were analysed using photoluminescence (PL) and photocurrent measurements to study the properties of NW-based QDs.

The composition of $InAs_xP_{1-x}$ QDs embedded within InP NWs was varied from x = 0.25 to x = 1, demonstrating the tuning of quantum confined energy levels. PL measurements demonstrated an emission peak that shifted towards lower energy levels as the As composition was increased. This result was also observed for QD absorption peaks through wavelength-dependent room temperature photocurrent measurements. InP NWs were successfully passivated with an AlInP shell, which was demonstrated through PL analysis.

The growth mechanism of patterned self-assisted GaP NWs on Si was studied through SEM and TEM analysis. It was found that for large V/III flux ratios the Ga seed particle reduced in volume throughout growth, which led to a smaller NW diameter. Conversely, for small V/III flux ratios the Ga seed particle increased in volume throughout growth, resulting in larger NW diameters. The dependence of V/III flux ratio on NW growth was characterized, allowing the tuning of NW diameter.

GaP NWs with p-i-n junctions were fabricated on a Si substrate with GaAs QDs embedded within the intrinsic region. To the author's knowledge, this is the first time such a device was demonstrated. The device demonstrated diode characteristics as expected for a p-n junction. Wavelength-dependent photocurrent measurements demonstrated the absorption of light within GaAs QDs, which was collected through electric field dependent tunneling and thermionic emission. The absorption of light extended beyond the bandgap of GaP due to the GaAs QDs.

Acknowledgements

First of all, I would like to thank my supervisor, Dr. Ray LaPierre for all of his support and encouragement throughout the years. He gave me plenty of opportunities in my undergraduate degree to satisfy my curiosity for research, which led me down the path towards a Ph.D. degree. As a supervisor, he is nothing short of terrific. Throughout the toughest times in the lab, some comical and some not so much, he was always there to guide me and help me overcome all of the challenges. He kept me on track and focused throughout my research, and I appreciated the fact that I could always reach him almost immediately for a discussion, whether in person or by email. I would also like to thank my committee members, Dr. Preston and Dr. Kitai, for their guidance throughout my degree.

Behind every great supervisor is a great research group, and I am very appreciative of all the support everyone in the LaPierre Group, both past and present, has given me. I would like to thank Chris Haapamaki, Jonathan Boulanger, Andrew Chia and Sandra Gibson for introducing me to the group, and teaching me all the skills I needed to get started. I would also like to thank Mitch Robson, Robin Yee, Junpeng Zhang, Brendan Wood, Aziz Rahman, Simon McNamee, Paige Wilson, Hadi Tavakoli, Nebile Isik, Azadeh Zavareh, and everyone else in the group for all the great discussion we had, and the memories we shared together. I will remember our adventures fondly, from conference trips, to group lunches and the many other outings that we had.

Throughout my research at McMaster I had plenty of help from the technical staff. I could not have done my research without the training and support of Doris Stevanovic, Zhilin Peng, and Shahram Tavakoli. They kept the equipment in this department working, and I knew that I could always count on them for help with my own projects and repair tasks. I have spent countless hours at the Canadian Centre for Electron Microscopy, and would like to thank Carmen Andrei and Chris Butcher for training me and putting up with all of my questions.

I have a lot of gratitude to give to my family. I would like to thank my Mom and Dad, Marina Kuyanova and Alexander Kuyanov, for always being there for me. I could always count on their advice and support when I needed it most. They believed in me throughout all of the steps in my degree and gave me a very happy place to come home to when I needed to unwind from a long day at the lab. Thank you to Jela and Rajko Gavranic who provided a second home that I was always welcome in.

The university experience is not complete without a little bit of help from my friends, and I cannot begin to start thanking everyone who kept me sane throughout my studies. I have so many stories and adventures with all of you, and I am looking forward to many more. I would like to give a special shout-out to the Ottawa crew. It was always a blast having you over! Thanks to everyone from the long running Wednesday Evening Beer group as well. It was great to have good company for some “serious thinking” at the Phoenix.

Finally, I would like to give a special thank you to my lovely fiancée, Vanja Gavranic. This thesis would not be possible without your support honey! Thank you for all the love you have given me throughout those years. I could not be happier to have you by my side.

I dedicate this work to my family and friends

List of Figures

1. Background

1.1 Introduction

The semiconductor age of modern electronics began in 1947 at Bell Labs, where John Bardeen, Walter Brattain, and William Shockley first demonstrated the transistor. Since then, the semiconductor transistor has replaced the vacuum tube as the technology of choice in computing, and the demand for cheaper and more efficient components has been steadily growing. Not long after the transistor was developed, the first practical Si solar cell was demonstrated in 1954 at Bell Labs. The semiconductor found applications in the computing, energy, and telecommunications industries, and became an indispensable tool in fundamental research. With the constant reduction in the size of device features, the field of nanotechnology was born, which was first conceptualized by the physicist Richard Feynman in his 1959 speech, “There’s Plenty of Room at the Bottom,” at Caltech. It is not long after this speech that the work by Wagner and Ellis [1] documented the growth of Si nano-whiskers in 1964, which started the field of nanowire (NW) research.

A NW refers to a high aspect ratio single crystal pillar, which typically has an epitaxial relationship with the substrate on which it is grown. NWs are most commonly fabricated, or grown, using a bottom-up approach with a wide range of deposition techniques, such as molecular beam epitaxy (MBE) [2], chemical vapour deposition (CVD) [3], metal-organic chemical vapour deposition

(MOCVD) [4], metal-organic vapour phase epitaxy (MOVPE) [5], vapour deposition [6], laser ablation [7], and sublimation [8]. A top-down approach can also be used, which involves reactive ion etching and a lithography-defined mask to remove the material from a thin-film device [9]. A wide selection of semiconductor materials is available for NW synthesis, ranging from Si [10] and Ge [11], to group III-V ternary materials (In, Ga, Al – As, P, Sb) [12–16], to oxides [17] and nitrides [18]. NWs can be epitaxially grown on a substrate of an identical material, such as Au-assisted InP NWs on a (111)B InP substrate [19], but also on a lattice-mismatched substrate, such as Ge [20]. In fact, the growth of NWs can be carried out without an epitaxial substrate, such as on carbon nanotube composite films [21] or even using the so-called aerotaxy technique [22]. One of the big advantages of NW structures is that, due to their small dimensions, the strain from lattice mismatch between NW and substrate is allowed to relax along the NW sidewalls, which makes growth on cheap Si substrates a possibility [23], the integration of which is explored in the work presented here. Several examples of NWs are presented in Figure 1.1, which includes scanning electron microscopy (SEM) and transmission electron microscopy (TEM) images.

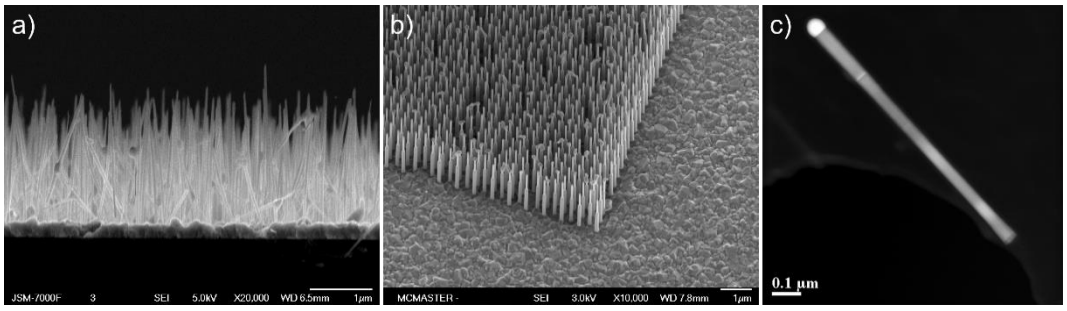

Figure 1.1: (a) SEM side-view of Au-assisted InP NWs on Si. (b) 30^o tilt SEM image of patterned Au-assisted InP NWs on Si. (c) Dark field TEM image of GaP NW with a small GaAs quantum dot.

The NW architecture offers a number of unique opportunities, such as the ability to integrate III-V devices with the well-established Si complimentary metal-oxide-semiconductor (CMOS) processing steps, create core-shell heterostructures not attainable with a thin-film approach, absorb specific wavelengths of light due to the properties of ordered arrays of NWs [24], and even explore new physics with the study of Majorana fermions within NWs [25]. Numerous NW based devices have been demonstrated, such as solar cells [26–31], photodetectors [32–34], lasers [35–37], light emitting diodes (LED) [38–40], transistors [41–43], and entangled-photon sources [44,45]. There are several review articles available for NW based photodetectors [46], solar cells [47] and entangled-photon emitters [48].

In this chapter the fundamentals of NW growth are introduced, covering the various growth techniques which utilize molecular beam epitaxy (MBE). The current status of NW research is summarized, with focus on some of the unique properties of NWs and their applications. The application that is the focus of this thesis is the infrared (IR) photodetector. Therefore, a summary of the current state-of-the-art detector technologies is provided, highlighting some of their limitations. A NW based IR photodetector is a promising solution to some of these limitations, and this chapter explores how these problems can be addressed. Section 1.4 describes the motivation behind the work presented in this thesis and provides an outline of its content.

1.2 NW Growth Mechanisms

The growth of NWs was first documented in the work by Wagner and Ellis [1], in which they described the growth of high aspect ratio Si nano-whiskers. The growth of nano-whiskers was described by the vapor-liquid-solid (VLS) process, by which a liquid metal seed particle is used as a sink for impinging growth species, resulting in epitaxial growth on semiconductor substrates. There are other NW growth regimes, such as the vapor-solid-solid (VSS) method [49]; however, this thesis focuses on VLS growth.

Figure 1.2 shows the Au-assisted VLS method, with the Au particles synthesized in situ. A thin (typically 1-5 nm) Au layer is evaporated onto a clean substrate (Figure 1.2a), and subsequently heated under vacuum inside a growth chamber (Figure 1.2b). Once the Au layer alloys with the substrate, it transitions to a liquid phase at the growth temperature and forms small droplets on its surface, with a random distribution of particles. For MBE growth, the growth species impinge on the semiconductor substrate, diffusing along the heated surface until they are absorbed by the Au droplet (Figure 1.2c). The concentration of the growth species within the Au droplet increases until it reaches supersaturation, leading to a thermodynamic driving force towards the formation of a solid crystal (Figure 1.2d). The crystallization occurs at the liquid-solid interface of the droplet to minimize the free energy of the system, resulting in a single crystal layer at the substrate. When the substrate is a single crystal material, such as GaAs or Si, the growth occurs epitaxially, i.e., one layer at a time, lifting

up the Au seed particle on top of the single crystal NW. Au-assisted NW growth on Si is the subject of Chapter 3.

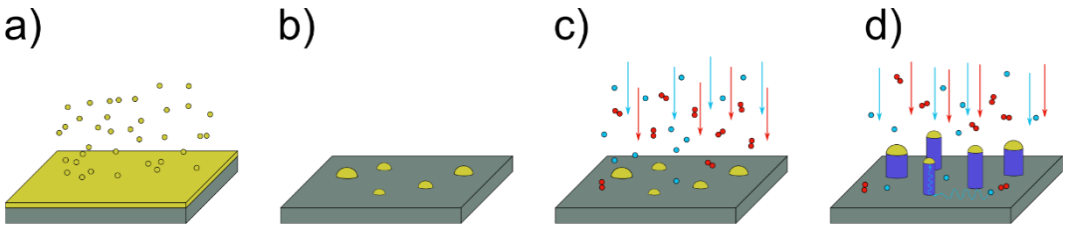

Figure 1.2: (a) A thin layer of Au is deposited on a clean substrate. For this work, the Au was deposited using e-beam evaporation on a (111) Si wafer. (b) The substrate is heated inside the MBE growth chamber, which melts the Au layer, resulting in droplets of Au dispersed along the surface. These are the seed particles for NW growth. (c) The growth species are supplied to the surface as either monomers or dimers, which are eventually absorbed by the Au seed particles. (d) Once a supersaturation is reached within the Au seed particle, there is preferential formation of the solid phase at the liquid-solid interface, resulting in epitaxial NW growth.

NW growth can proceed in either the axial growth regime, which refers to the VLS formation of material in the preferred growth direction of the NW below the seed particle, or the radial growth regime, which refers to the growth of material on the NW sidewall. A study of GaAs NWs by M.C. Plante and R.R. LaPierre [50] identified the growth conditions that promote one growth regime over another. High temperature growths at 600 ^{o}C with moderate V/III flux ratios result in axial growth, while low temperature and high V/III flux ratios promote radial growth. These findings allow the design of NW structures such as the radial p-n junction solar cell, and the growth of passivation shells, which are utilized in Chapters 3 and 6.

NW growth regimes are analyzed by plotting the NW height versus the NW top diameter, D (which is typically related to the seed particle in the case of purely axial growth), such as that shown in Figure 3.6. In order to model the

growth rate of VLS NWs, the various paths that material can take to reach the Au seed particle need to be considered. The material can be supplied to the Au droplet through the following ways: 1) direct impingement on the Au droplet; 2) diffusion of material along the substrate and subsequently along the NW sidewall, until it is absorbed by the droplet; and 3) re-emission of material from the substrate, leading to scenarios 1) or 2). Material impinging directly on the droplet is absorbed by the droplet, with the amount of material captured equal to the surface impingement rate of the material. The material diffusing along the surface and then the NW sidewall is dominated by the sidewall diffusion, with the NW growth rate having a 1/D relationship. Both of these growth regimes were studied for InP Au-assisted NWs by C.M. Haapamaki and R.R. LaPierre [19].

The Au-assisted VLS growth described above results in randomly arranged NW locations with a distribution of NW diameters and heights based on the conditions of the synthesis of Au droplets. The NW growth tends to be in the direction that minimizes the total free energy of the system [51], which is typically (111)B. Other directions are also observed, most notably the (001) direction of InP NWs [52]. One of the influencing factors proposed for the preferred growth direction is the strain between the substrate and the NW. Material systems with a larger lattice mismatch, such as InP and InAs NWs on Si, tend to manifest other, non-vertical (111) growth directions, as can be seen in Figure 3.1. On the other hand, more closely matched materials, such as GaP NWs on Si, have a tendency towards the vertical (111) directions, as shown in Figure 6.1 and other works [23]. The challenge of controlling the NW growth directions

goes beyond the lattice mismatch problem, however, with influences from surface preparation, thermal history, and the composition of the metal seed particle [51].

Au is the most commonly used metal seed particle for NW VLS growth, but many others have been utilized, such as Ti [53], Cu [54], Al [55], and Pt [56]. Au is an inert element with a relatively low melting point, making it the most popular material of choice for NW growth. A major disadvantage of Au is its incompatibility with Si processing steps, due to the formation of deep level traps within it [57], as well as the degradation of carrier lifetime [58], which is strong motivation for the shift away from Au-assisted NW growth techniques. An alternate method to using a Au seed particle is the self-assisted VLS growth regime. Instead of Au, a group III element present in the NW is used as a seed particle, such as Ga or In for GaAs or InP NWs.

Both Au and self-assisted NWs can be arranged into periodic arrays through various patterning approaches. Typically a thin (20-30 nm) oxide layer is deposited onto the growth substrate, and is patterned using a technique such as electron beam lithography (EBL) [16] or nano-imprint lithography [59], which opens up an array of holes in the oxide, defining the sites for NW growth. Periodic arrays of NWs ensure that the growth conditions for each NW are better controlled, resulting in tighter control of diameters and heights of NW ensembles. This is very important for creating high quality and predictable ensemble devices, as well as for modelling NW growth regimes. The self-assisted patterned NW growth regime is shown in Figure 1.3.

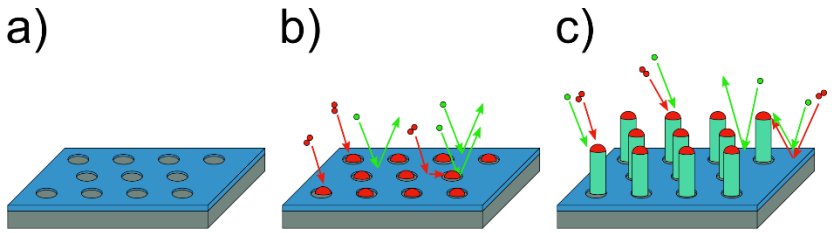

Figure 1.3: (a) The substrate has a thin oxide (20-30 nm) with a periodic pattern of openings defining the location of NWs. (b) For ternary group III-V growth, the impinging group III material collects in the oxide openings, resulting in the formation of droplets, which are the seed particles for NW growth. (c) Once a supersaturation of group V material within the group III droplet is reached, the NW growth is initiated.

For ternary III-V NWs, such as GaAs or InP, the impinging group III and group V species have a low sticking coefficient on the oxide, preventing the growth of a parasitic film and facilitating the collection of material within the oxide openings. Group V material typically has a high desorption rate on Si and SiO_x, while the group III material starts to accumulate within the SiO_x openings. In the VLS growth regime, the group III material forms a droplet either during the growth process or through a pre-deposition step [60]. Similarly to the case of Au-assisted NW growth, a critical concentration of group V material within the group III droplet is eventually reached, facilitating formation of a III-V layer at the solid-liquid interface.

Unlike with Au-assisted growth, in which the seed particle typically remains at a constant volume throughout the growth, the self-assisted group III seed particle can increase or decrease in volume, or be entirely consumed. This creates a new set of possibilities in NW growth, such as the control of NW diameter using the seed particle, which is the focus of Chapter 5, and the full consumption of the droplet for growth of a passivation shell, which is explored in Chapter 6.

1.3 NW Applications

1.3.1 Infrared Photodetectors

The majority of infrared (IR) photodetectors can be classified into either photon detectors or thermal detectors. Thermal detectors rely on the absorption of energy from IR radiation, which increases the temperature of the material. An example of such a device is a bolometer. Photon detectors rely on the absorption of an IR photon by the material, which results in a change of the charge distribution, such as the generation of an electron-hole pair. The resulting electrical charge can be detected by a circuit and related to the incident radiation, such as with a p-n junction diode operated in reverse bias. Photon detectors have a much higher sensitivity and response time compared to thermal detectors, but have a limited spectral range. Thermal detectors span a very long IR range with a very steady response. Their response time is very poor, due to their dependence on the heating and cooling of the material. The work presented in this thesis focuses on photon detectors.

One type of photon detector is a photo-sensitive resistor. Incident IR photons above the band gap of the material excite electrons into the conduction band and increase the conductivity of the device. Photo-resistivity measurements can be performed as a function of wavelength to characterize these devices. This type of detector is the focus of Chapter 3, in which the growth and characterization of an intrinsic InP NW based photodetector with InAsP QDs insertions is discussed. Another type of detector is based on a p-n junction, in which the photo-generated

electrons are separated across the depletion region of the junction and collected. By operating these devices in a reverse bias, the reverse saturation current can be related to the incident radiation. This type of detector is the focus of Chapter 6, in which the photocurrent collected from GaAs QDs embedded within the intrinsic region of a p-n junction is analyzed.

The most commercially successful photon detectors are mercury-cadmium-telluride (MCT) detectors. MCT is a group II-VI semiconductor, which has a composition-dependent direct bandgap. HgTe is a semi-metal which has a bandgap of -0.26 eV at room temperature, and CdTe is a semiconductor which has a bandgap of 1.49 eV at room temperature [61]. Detectors based on these materials have very high figures of merit, such as responsivity, and can cover a very broad range of wavelengths. Despite the success of these types of detectors, they have several drawbacks. MCT detectors are grown on lattice-matched CdZnTe substrates, which currently have an area limitation of approximately 50 cm^2, which is too small to accommodate large format arrays of detectors (2048x2048 pixels or larger) [62]. In addition, MCT has a different coefficient of thermal expansion from Si based readout circuits, leading to complications when employing techniques such as indium-bump bonding [63].

A technique for addressing some of the issues of MCT is to engineer a lower bandgap material through the use of quantum confined energy levels. This allows the use of materials such as GaAs, which has the advantage of a mature industry behind it. One example of a quantum well device is the GaAs/AlGaAs multiple quantum well focal plane array [64], in which the IR absorption takes place

between energy levels in the conduction band of the well. This is termed intersubband absorption (compared with interband absorption between the conduction and valence band of an MCT detector). The energy levels responsible for IR absorption can be easily tuned through changing the well dimensions and composition, leading to applications in multi-spectral absorption devices. The quantum well detector addresses some of the issues with the MCT detector, such as the small substrate area available, but has several limitations of its own. The quantum efficiency of the detector is low because optical transitions from normal incident light are forbidden in quantum wells. In addition, they also require an operating temperature below 70 K.

The quantum dot (QD) IR photodetector (QDIP) provides several advantages over the quantum well detector, such as the inherent sensitivity to normal-incidence light, higher operating temperature, and a lower dark current [65]. One example of a QDIP is the GaAs/InAs thin-film material system. MBE is used to grow a thin, lattice-mismatched layer of InAs on a GaAs substrate. Once a critical thickness of the layer is reached, the strain due to the lattice mismatch of the two materials can be relaxed by the formation of InAs islands, which is referred to as the Stranski-Krastanov (SK) growth technique [66]. The InAs QDs can be doped with an appropriate dopant, such as Si, in order to provide sufficient carriers for absorbing the incoming light, and surrounded by a GaAs conduction region. A schematic of such a device is shown in Figure 1.4 [65].

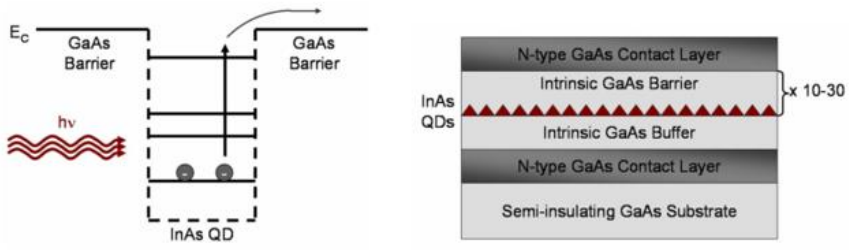

Figure 1.4: Band energy levels and schematic of an InAs/GaAs QDIP device. From Ref. [65].

In a QDIP device, the absorption of incoming IR light occurs when an electron at a lower energy state absorbs a photon, which promotes it to a higher energy state. From here, the excited electron can reach the GaAs conduction band through either field-assisted tunneling or thermionic emission over the barrier. The photo generated electrons that reach the conduction band change the conductivity of the device, which is measured and related to the intensity of incident light. These types of intersubband absorptions typically have a fairly small energy, falling into the mid-IR range. If this structure also has quantum confinement in the valence band (such as InP/InAsP quantum dots), there are transitions from valence band energy levels to conduction band energy levels.

A QDIP device presents several challenges that need to be addressed for effective competition with MCTs. First, the SK growth regime of QDs is an inherently stochastic process, which results in a large distribution of QD dimensions, leading to a spatial distribution of energy levels. This results in an increased detector absorption linewidth and reduced peak sensitivity as well as variations in the doping levels. For larger doping concentrations there are more carriers available for absorption, increasing the sensitivity of the detector.

However, too many charge carriers increase the dark current significantly by either thermionic emission or tunneling under an electric field.

1.3.2 NW Based Photodetector Devices

An alternative to the SK growth method is the use of NW arrays to grow QDs. Patterned arrays have good control over the NW diameter, which, for certain conditions, is determined by the size of the seed particle, such as with the InP and GaP NWs presented in Chapter 5. The VLS growth mechanism is driven by the supply of material to the seed particle, whether it is Au-assisted or self-assisted growth. To grow a QD section within a NW, the group V supply is switched from P_2 to As_2, which changes the composition of a NW from InP or GaP to InAs or GaAs. The abruptness of the interface is not atomically flat, and depends on how quickly the concentration of material can be replaced within the seed particle, which has been studied by K.A. Dick et al. for InAs/GaAs interfaces [67]. To form a QD within a NW, a higher bandgap material, such as InP and GaP, is replaced by a lower bandgap material, such as InAs and GaAs. After the desired length of the lower bandgap material is reached (typically <15 nm), the growth is switched back to the higher bandgap material, completing the QD. This growth technique solves the problem of non-uniform dimension and doping distribution of SK type of QDs because the NW-based QD dimensions are controlled by the seed particle diameter and growth time, as opposed to the strain relaxation process in the SK method.

The progress in the field of NW-based photodetectors can be broken down into research of two types of devices. The first is a single NW device, in which a NW is laid flat on a substrate, with both ends of the NW contacted. This type of device has applications in single photon detectors and nanowire-based lasers. The second type of device is a NW ensemble, in which a whole array of NWs is contacted at the top with a transparent contact layer, such as indium tin oxide (ITO) and at the bottom through the growth substrate. The applications of this type of device include photovoltaics and imaging systems.

One of the first important NW based devices was reported by H. Pettersson et al in 2016 [68]. They presented a device based on InAs NWs with InAsP insertions, with a single NW device showing a photocurrent peak close to 1200 nm. In 2009, W. Wei et al. presented vertical InAs NWs on Si, creating a heterostructure between Si and InAs [69]. This was an ensemble NW type of device, in which NWs were surrounded by a polymer and the tops were contacted with indium tin oxide (ITO). This device showed a strong photocurrent response to a broadband illumination source. External quantum efficiency measurements showed a peak efficiency of 20% at 1 μm, followed by several small peaks from 1.4 μm – 1.8 μm. This type of NW contacting scheme was studied in detail by A.C.E. Chia and R.R. LaPierre through their work on contact planarization of ensemble NWs [70]. Another noteworthy NW array device was reported by J. Scensson et al. in 2013, with InAsSb NWs grown on an InAs substrate [71]. The NWs were surrounded by a polymer and contacted by an opaque titanium/gold top contact. The device was illuminated by a broadband IR source passing

through the back of the InAs substrate. The photocurrent response showed a strong response between 4 μm and 5 μm. A further discussion on NW-based photodetectors is presented in Section 3.1.

1.3.3 QDs within NWs

The previous section summarized some of the achievements in fabricating NW-based photodetectors that demonstrate a response in the IR range. However, to compete with MCT detectors available on the markets, even further improvement in performance is required, with the QDIP type device being one of the candidates. Before studying the QDIP NW-based detector, it is important to highlight some achievements in the growth and characterization of QDs embedded within NWs.

One of the earliest published works on QDs embedded within NWs was by M. Tchernycheva et al. in 2007, who placed InAsP insertions within InP NWs on an InP substrate [72]. They performed photoluminescence (PL) on single NWs showing broad emission peaks at 1.6 μm and 1.2 μm, which were a function of InAsP composition. In addition, they observed sharp emission peaks at 1.401 μm and 1.412 μm, demonstrating QD-like behaviour. In 2009, M.H.W. van Weert et al. grew an $InAs_{0.25}P_{0.75}$ QD within an InP nanowire on an InP substrate [73]. The QD had an axial height of 10 nm, a diameter of 30 nm, and was passivated by an InP shell surrounding the NW. The emission showed a quantum dot energy level at 964.9 nm. In 2010 S.N. Dorenbos et al. grew InAsP QDs within InP NWs on an

InP substrate emitting at 1.3 μm, extending the device performance deeper into the IR range [74]. The PL emission showed QD behaviour, with a demonstration of single photon emission using a HeNe pump laser. In 2011 D. Dalacu et al. grew selective area InP NWs with InAsP QDs on an InP substrate [75]. They deposited a SiO_2 mask on the InP substrate, and used electron beam lithography to define the openings which determined the dimensions and the location of NWs. The QDs showed a sharp emission at 1.15 μm. Another important study by J.C. Harmand et al. in 2013 showed emission from InAsP QDs, embedded within InP NWs fabricated by MBE on an InP substrate, within the wavelength range from 1000 nm to 1500 nm [76].

The above summary highlights two important points about the work done thus far. The NWs were grown on III-V lattice-matched substrates and PL was measured at low temperatures, i.e., below 10 K. Such cooling is typically performed using a He flow cryostat, which is not feasible for an imaging device. Commercial devices typically operate at 70 K, but the goal of future device operation is above 140 K. To address these issues, the work presented in this thesis focuses on electrical measurements performed at room temperature, with devices grown on Si substrates.

1.4 Thesis Overview

The motivation behind the work presented in this thesis is to explore the feasibility of using NWs as an architecture for the QDIP type of photodetector.

The work presented here focuses on using an inexpensive Si substrate and operating the devices at room temperature. This thesis presents work undertaken in the growth and characterization of QDs within both the InP/InAsP and GaP/GaAs material systems. Working with NWs provides several advantages in the growth of III-V based QDs, discussed in the previous sections, but also leaves several unique challenges. The work presented here establishes the relevant NW growth mechanisms for III-V based devices on a Si substrate and studies the effect of changing some of the growth parameters. A better understanding of these material systems will help researchers create more efficient devices and overcome some of the obstacles presented above. Some of these obstacles are addressed in this work, demonstrating NW-based photodetector devices, which can collect electron-hole pairs generated within the QDs at room temperature.

The experimental methods used in this work are outlined in Chapter 2, including MBE, electron microscopy, PL, device processing details, and electrical measurements. Chapter 3 studies Au-assisted InP NWs with embedded InAsP QDs, grown on a Si substrate. The QD shape and composition is studied through electron microscopy, with a growth model presented for this material system. In addition, the QDs were studied through both PL and photocurrent measurements, showing the tunability of photocurrent from light absorbed with the QDs based on their composition. This work was previously published in Nanotechnology [77]. Chapter 4 presents a more in-depth study of the passivation of GaAs NWs. This work was previously published in the Journal of Applied Physics [78], with the author of this thesis contributing the PL work. The effectiveness of GaP as a

passivation of GaAs NWs was explored with both electrical and optical measurements performed on single NWs. Chapter 5 shifts the focus away from Au-assisted to self-assisted NW growth. A detailed study of self-assisted GaP NWs on a patterned Si substrate is presented, demonstrating the ability to tune the NW diameter based on the consumption or accumulation of group III material within the seed particle during VLS NW growth. This work was previously published in the Journal of Crystal Growth [15]. Chapter 6 uses the NWs grown in Chapter 5 to create a GaP-based photodetector on a Si substrate, presenting a p-n junction device. Furthermore, GaAs QDs are embedded within the intrinsic region of the p-n junction to study their electrical properties at room temperature. Chapter 7 presents the conclusions of the work in this thesis and suggestions on the future steps for these projects.

2. Experimental Method

2.1 Molecular Beam Epitaxy

MBE is an ultra-high vacuum semiconductor deposition technique, invented by Alfred Cho and John Arthur in 1971. The thin-film growth rate can be precisely controlled with abrupt changes in composition through the use of mechanical shutters. The high vacuum levels allow the mean free path of the molecular beams to be long enough that they can travel to the sample without any other interactions. The growth materials and the associated dopants are supplied in a molecular beam, where they interact with the substrate to epitaxially form precise thin films and structures. The material can be supplied through either evaporation or a gas source. Effusion cells with solid sources are resistively heated at operating temperatures between 850 ^{o}C and 950 ^{o}C for Ga, for example, forming beams of single atoms. Gas sources pass through a gas cracker that operates at a typical temperature of 950 ^{o}C, which strips the P and As from the hydrogen, resulting in beams of dimers or tetramers.

The system used at McMaster University is a SVT Associates gas-source MBE, illustrated in Figure 2.1. A sample is loaded into a custom made molybdenum holder and is placed in contact with a resistive heater and thermocouple. The temperature is also measured using a pyrometer. A hydrogen inductively coupled plasma (ICP) source is used to clean the sample surface before initiating growth. The MBE system has several effusion cells providing In,

Ga, Al, Sb and Si sources. The two gas sources available are arsine and phosphine (AsH_3 and PH_3) which provide P_2 and As_2 dimers once cracked. The molecular flux from the effusion cells is controlled by setting the temperature, which changes the evaporation rate of the supply material. Each effusion cell has a mechanical shutter, allowing for quick beam control. The molecular flux from the gas cracker is controlled by setting the gas flow rate with a valve turning the beam on and off.

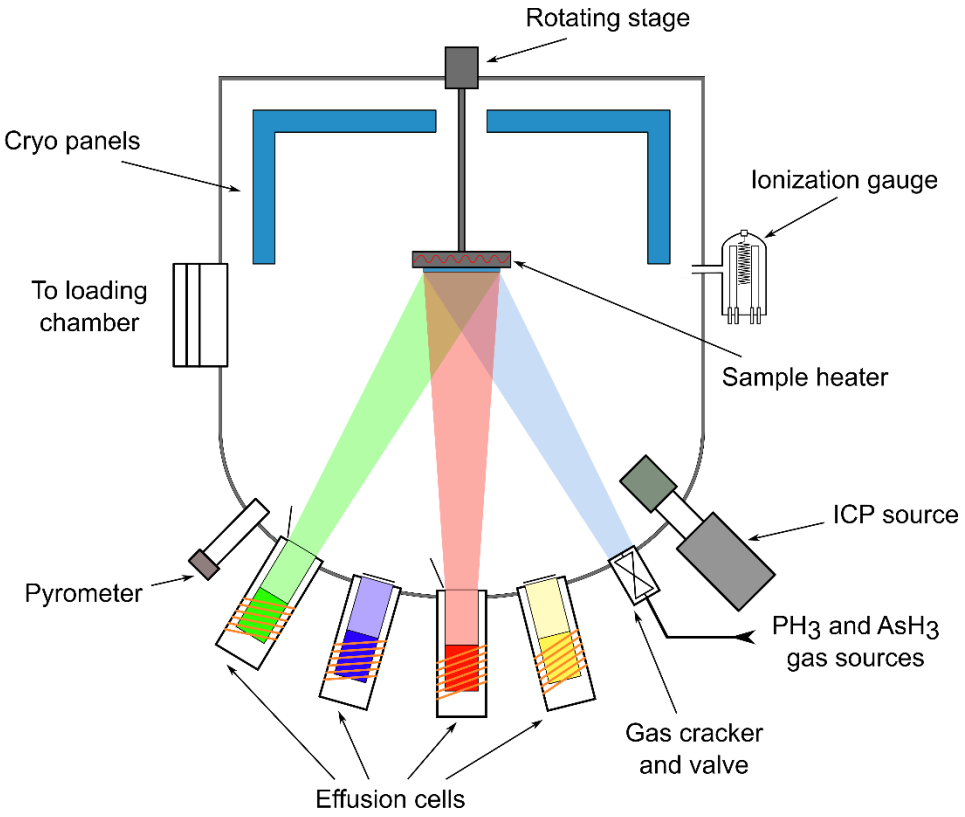

Figure 2.1: Illustration of the MBE system available at McMaster University in the Engineering Physics Department. The available effusion cell sources are Ga, In, Al, Sb, Be and Si. P_2 and As_2 sources are available from a hydride gas cracker. The sample can be heated to temperatures up to 600 ^oC for the NWs studied in this thesis.

2.2 Electron Beam Lithography

The two NW types studied in this thesis are the randomly arranged and patterned NWs, using both Au-assisted and self-assisted VLS growth regimes. For randomly arranged NW growth the processing technique is very simple, which is one of the advantages of this method. This is outlined in Section 3.2. There are numerous techniques for patterning a substrate for NW growth, which include but are not limited to EBL [16] and nano-imprint lithography [79]. The growth of self-assisted patterned NWs is outlined in Section 5.1.

Photolithography is a very powerful technique for transferring a desired pattern, such as a contact finger scheme for a solar cell, to a photo-sensitive polymer, also known as a photoresist (PR). A mask is used to selectively block UV light, which weakens (strengthens) the polymer chains within the positive (negative) PR. It is even possible to use a laser beam to raster over the PR to directly expose a pattern without the need for a mask. The feature sizes obtained are limited by the wavelength of light used. EBL overcomes this limit by using a rastering electron beam within a specialized scanning electron microscope (SEM) to define the pattern on a thin PR layer. The rastering electron beam deposits charge within the polymer, allowing the weak sections of the PR to be chemically developed. This is a serial process, which limits the total area that can be written in a reasonable amount of time. Figure 2.2 summarizes the steps taken in order to define a pattern on a Si substrate.

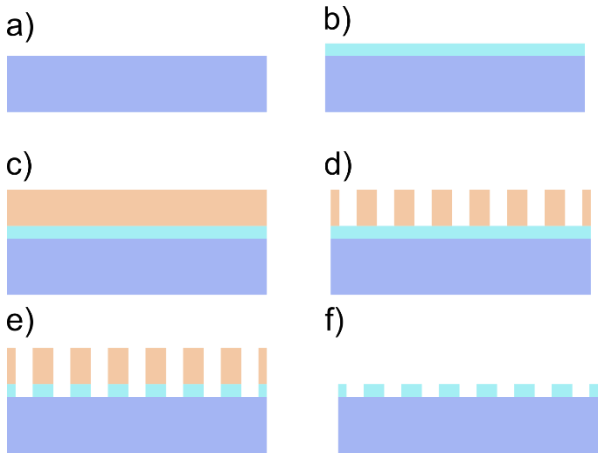

Figure 2.2: (a) The Si substrate is taken directly from the manufacturer and loaded into the oxide growth chamber. (b) A thin (typically 20-30 nm) SiO_x layer is grown using plasma-assisted CVD. (c) An e-beam sensitive PR is spin coated onto the sample. (d) e-beam pattern of various NW pitches and diameter is written and developed. (e) RIE is used to etch through the SiO_x, exposing the Si substrate. (f) The PR is removed.

The epi-ready substrate is received from the manufacturer (Figure 2.2a), which is Virginia Semiconductor[1] for this work, and loaded into a plasma-enhanced CVD system. 20-30 nm of high quality SiO_x is deposited by CVD (Figure 2.2b), which is the layer in which the pattern is defined. A thin PR (1:1 mixture of ZEP520A:Anisole) is spin coated at 6000 RPM for 1 min with an acceleration of 584 rpm/s and annealed at 180 ^oC for 3 min (Figure 2.2c). The pattern, which is described in detail in Section 5.2, is written using an EBPG 5000+ EBL system at the University of Toronto (Figure 2.2d). The pattern is then developed using a mixture of MIBK developer and isopropyl alcohol (45 mL: 5 mL) for 30 s. The sample is then dried with N_2.

The next step is performed at McMaster University inside a clean room. The developed pattern of openings in the PR exposes the sections of SiO_x which are

[1] https://www.virginiasemi.com (Accessed Sep 2017)

removed using reactive ion etching (RIE). An O_2 plasma is used for this, with an operating pressure of 320 mTorr (~50 mTorr base pressure) and a power of 100 W. The 30 nm oxide is etched for 95 s, which exposes the Si substrate underneath (e). Finally, the PR is removed by sonicating the sample for 5 min in a ZD-MAC PR removal chemical, followed by sonication in acetone and isopropanol for 3 min each (f). The final step, immediately prior to loading the sample within the MBE growth chamber, is a 25 s dip in a 1:10 solution of buffered hydrofluoric (HF) acid to deionized (DI) H_2O, which removes any remaining oxide within the pattern.

The EBL technique for growing patterned arrays of NWs requires some degree of troubleshooting in order to optimize the NW yield for different material systems. The work by S. Gibson, J. Boulanger, and R.R. LaPierre identified the opportunities and pitfalls of self-assisted patterned GaAs NW growth on Si [80].

2.3 Electron Microscopy

The first step in analysing NW samples is electron microscopy, which is used to study the morphology, crystal structure, and chemical composition of NWs. In 1925, Louis de Broglie proposed that electrons can be treated as waves with very small wavelengths, which was demonstrated independently by two research groups (Davisson and Germer and Thomson and Reid) in 1927 by carrying out electron-diffraction experiments [81]. After the wave-like nature of particles was demonstrated, the idea of using electrons for imaging was proposed by Ruska and

Knoll in 1932 in their paper, “Das Elektronenmikroskop” [82]. They calculated that for an accelerating voltage of 75 kV the resolution limit would be 2.2 Å, which was achieved 40 years later [83]. Two types of electron microscopes were developed: transmission and scanning electron microscopes (TEM and SEM). The lower accelerating voltage SEM could not compete with the resolution of the TEM, and therefore was geared toward observing surfaces of specimens [84].

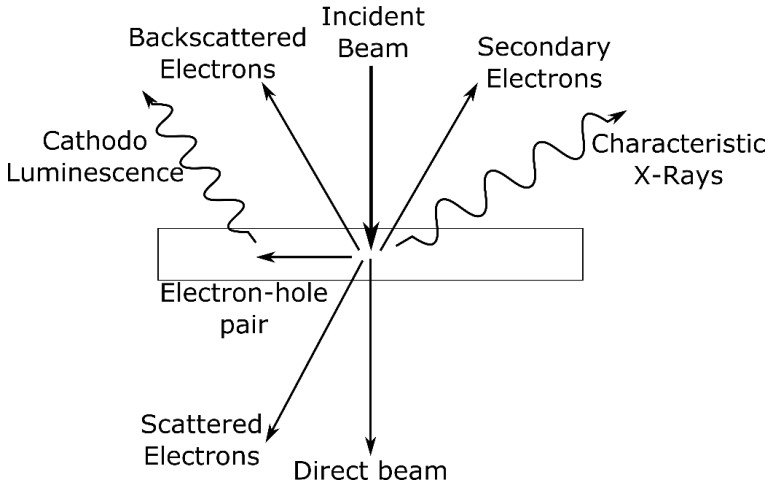

Figure 2.3: The interaction of an electron beam with a semiconductor sample. The backscatter electrons, secondary electrons, cathodoluminescence, and characteristic X-rays are used for SEM analysis. The direct beam, scattered electrons, and characteristic X-rays are used for TEM analysis.

2.3.1 Scanning Electron Microscopy

A Scanning electron microscope (SEM) generates a beam of electrons, from various sources, which is focused onto the sample. A technique for generating a beam of electrons consists of resistively heating either a tungsten wire, or a lanthanum hexaboride (LaB_6) crystal, which allows the electrons in the material to overcome the work function energy and escape through thermionic emission. Resistively heated sources are often inexpensive and do not require a high

vacuum, but are limited by their low brightness, limited lifetime, and large energy spread [85].

Another technique for generating electrons is to use field emission. The first type of field emission source is the cold field emitter (CFE), which relies on a very high applied electric field across a sharp cathode tip. The CFE emission is independent of the temperature of the tip, but requires that the surface of the tip is clean, which can be achieved with high vacuum levels. Even in the best conditions, the surface slowly degrades, requiring periodic high temperature "flashing" to clean it. The second type of source is a Schottky field emitter (SFE). In a SFE source, the electric field is used to reduce the work function of the tip for improved thermionic emission.

In SEM imaging, the incident electron beam enters the sample, scattering within an interaction volume, which depends on the beam energy, atomic number of the sample, and sample surface tilt. The electron beam undergoes many interactions within this interaction volume, resulting in either secondary electron emission, scattered electrons, or emission of characteristic X-rays (shown in Figure 2.3). An SEM image is formed by scanning the beam across the sample, and detecting the various electrons and X-rays that return from the sample.

Backscattered electrons (BSE) are electrons that enter the sample and undergo several scattering events that change their trajectory to high angles ($>90^{o}$), allowing them to escape from the entrance surface of the sample. The number of BSE increases with the atomic number (Z) of the sample, which is a result of a higher elastic scattering cross-sectional area. The number of BSE can be

expressed using the backscatter coefficient, η, defined as the number of BSE over the total number of incident electrons. The backscatter coefficient increases for higher Z materials, which leads to image contrast between different materials when imaging with BSE.

The incident beam of electrons can also undergo inelastic scattering, giving enough kinetic energy to allow outer shell electrons to escape. These electrons are called secondary electrons (SE), and are identified as electrons with energy less than 50 eV [85]. SE are produced along the full path of the incident electron beam, within the interaction volume. However, due to their low energy, they are attenuated fairly quickly through their own inelastic scattering events. Furthermore, SE must overcome the work function of the material at the surface to escape into vacuum, leading to a relatively shallow depth from which they can escape. The maximum depth of emission was determined to be roughly 5 nm for metals and 50 nm for insulators [85]. The yield of SE is increased with lower incident beam energies because a large part of the interaction volume is within the escape depth of the sample.

SE can be generated by both the incident beam and the backscattered beam, leading to two sources of SE, referred to as SE_1 and SE_2, respectively. The generation of SE_2 by BSE is a more probable process than from the incident beam, because BSE tend to approach the surface of the sample at larger angles, generating more SE electrons within the escape depth. In addition, the BSE beam undergoes many inelastic collisions, resulting in a lower energy, which leads to a more efficient transfer of energy to the ejected SE. For lighter materials, the SE_1

process dominates because the backscatter coefficient is low. For heavier materials the SE_2 process begins to catch up. The total yield of SE is fairly insensitive to the atomic number, with a value of roughly 0.1 with a beam energy of 20 keV [85]. A few notable exceptions are Au, which has a larger than normal yield of SE_2, resulting in a SE yield of 0.2, and C, which has a very small yield of SE_2, resulting in a SE yield of 0.05. Imaging using SE provides information on the morphology of the sample.

The most common electron detector is the Everhart-Thornley (ET) detector. The front of the ET detector is a scintillator, which converts high energy electrons to photons. These photons are guided through a quartz window out of the high-vacuum environment. A photo-multiplier tube is used to convert the photons back to electrons and generate a measurable signal. The high energy BSE can excite the scintillator by themselves. To detect the low energy SE, a large potential is applied across the scintillator to accelerate them to higher energies. A Faraday cage is used to separate the scintillator bias from the electron beam. By biasing the Faraday cage with a positive voltage, it is possible to more efficiently collect SE.

An incident high-energy electron can also penetrate the outer conduction/valence bands of the material and interact with the inner shell electrons. If there is enough energy transferred to the inner-shell electron, it can be ejected, ionizing the atom. The ionized atom eventually returns to the ground state by having an electron from a higher energy level occupy the empty state. This transition results in an emission of an X-ray equal to the difference between

the two energy levels, and so forms a unique fingerprint for different atoms. By measuring the energies of these X-rays, it is possible to identify the spatial distribution of different atoms. This technique can be performed by both scanning TEM and SEM. When analyzing NW samples with SEM, the number of X-rays emitted is relatively low, which makes it difficult to identify fine features such as the VLS seed particle on top of NWs and core-shell structures.

2.3.2 Transmission Electron Microscopy

TEM imaging can be performed with both TEM and scanning TEM modes (STEM). In order to effectively analyze semiconductor materials with TEM, the sample must be very thin, preferably less than 100 nm, which works very well with NW samples. Typical NW diameters presented in this thesis are 50-100 nm, and can be imaged directly, without any further processing or thinning. To prepare NW samples for imaging two techniques can be used: dispersion of NWs in solution, or focused ion beam (FIB) milling.

To prepare the TEM sample through a solution, a single NW pad is isolated by cleaving and submerged into a small amount (<1 mL) of isopropanol. The vial is then placed in a sonication bath for 3-5 min, depending on the NW diameter. Through the work presented in this thesis, it was found that NWs of diameters <50 nm can be removed from the substrate with 3 minutes of sonication, but NWs which have thick passivation shells or core-shell structures can require up to 5 minutes. The longer the sonication time, the more debris from the substrate

accumulates. A micro-pipette dropper is used to disperse the solution over a holey carbon grid from SPI Supplies[1], which is ready to be imaged as soon as the sample is dry. This dispersion technique captures a sample of all the NWs present on the NW pad. In some studies, such as that presented in Chapter 5, it is important to analyze specific NWs on a given array. In cases like this, FIB milling is used to cut out a select area containing the NWs in question, and prepare a thin TEM sample.

Figure 2.3 shows the important electron-material interactions. For TEM imaging, the direct beam, scattered beam, and the characteristic X-Ray emission are the interactions used for TEM analysis. Both elastic and inelastic scattering can occur within the sample. Electrons scattered by Coulombic interactions can undergo angular changes of a few degrees by interacting with the electron cloud, or scattered through very high angles by interacting with the nucleus. The Coulombic interaction with the nucleus is very important because it depends on the Z number of the atom, providing a means of chemical analysis of the sample.

The first type of TEM imaging mode is called bright-field imaging. As the incident electron beam passes through the sample and undergoes various scattering events, the direct beam loses intensity depending on sample thickness, crystal structure, defects, and the type of material. By allowing the direct beam to fall on either a phosphor screen or a CCD camera, it is possible to obtain a bright field image of the sample. An example of a typical bright field image of a gallium phosphide (GaP) NW is shown in Figure 2.4.

[1] http://www.2spi.com/category/grids-custom-holey-carbon/ (Accessed Sept 2017).

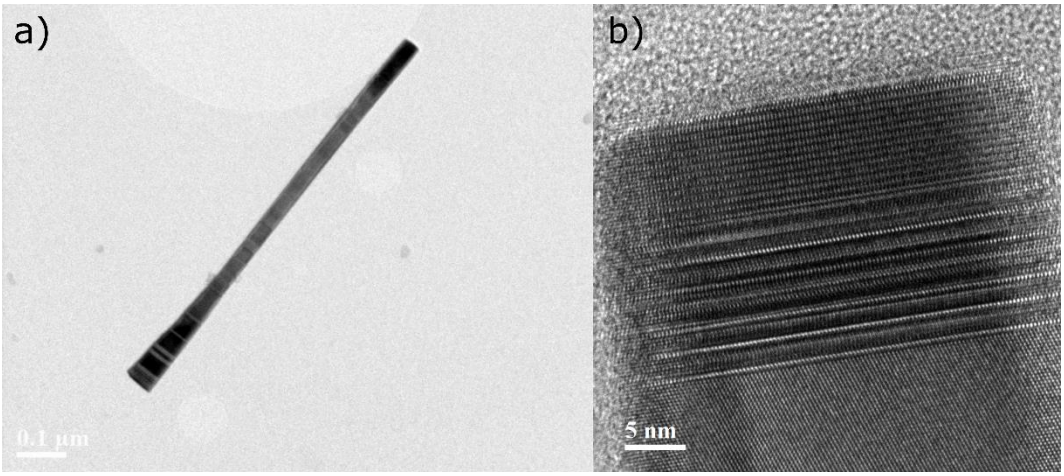

Figure 2.4: (a) A bright field image of a GaPNW oriented in the [011] zone axis. (b) A high resolution bright field image of a GaP NW oriented in the [011] zone-axis

Figure 2.4a shows a bright field image of a GaP NW on a holey carbon grid. The base of the NW is thicker than the middle and top sections, which results in a darker appearance of the NW at that spot. In addition, the NW is bent, which can be verified (not shown here) by mapping the [011] zone-axis angle along the length of the NW. This leads to the top and bottom to be darker than the middle in this image. The next set of features visible are a series of thin bands perpendicular to the [111] growth direction along the length of the NW. These are referred to as stacking faults, and occur when zincblende (ZB) and wurtzite (WZ) crystal phases alternate for several atomic layers. A discussion on stacking faults within GaAs NWs can be found in the work by M. Plante and R.R. LaPierre [86]. A magnified view of these stacking faults are shown in high resolution TEM in Figure 2.4b. Another feature visible in the bright field image is a series of wider bands perpendicular to the growth direction, which correspond to twin planes. Figure 2.4

(b) shows a high resolution image of the top of the same NW. This image shows two different crystal phases: WZ at the top of the NW, and ZB further away.

Crystallographic information can be obtained by a number of techniques using TEM. For a crystalline sample oriented in zone-axis, the incident electron beam is diffracted by the lattice planes. The diffracted beam interacts constructively and destructively, forming a diffraction pattern, similar to that formed from an optical grating. The pattern formed from a crystal lattice is a series of bright spots, which correspond to diffraction from specific crystal planes. This pattern is unique to the crystal structure of the sample, and contains a wealth of information. The diffraction pattern can be obtained from the whole sample, but it is often desirable to analyse small sections of the sample. There will inherently be inconsistencies in the crystal orientation along the length of sample that distort the diffraction pattern, and it is important to compare the crystal structures at different spots. To perform this kind of analysis, a selective area diffraction (SAD) aperture is placed in the first image plane after the sample, limiting the area of the sample from which the diffracted beam is collected.

Figure 2.5a shows a SAD pattern from a ZB GaP NW, which is the subject of Chapter 5. It is evident from the SAD pattern that there is a twin plane present. Figure 2.5b shows a SAD pattern from a WZ InP NW, which is studied in Chapter 3. The spacing and angle between the diffraction spots in these images can be measured and compared with catalogues of diffraction patterns from different crystal structures, such as that available in Ref [81].

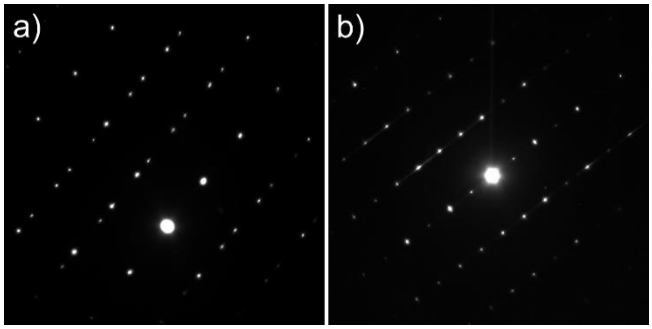

Figure 2.5: Examples of SAD patterns obtained in the middle of the NWs for (a) self-assisted GaP NWs and (b) Au-assisted InP NWs. The crystal structures are ZB in (a) and WZ in (b).

Another indispensable feature of the TEM is the scanning mode operation. In this mode, the electron beam is focused to a fine point and rastered over the sample, similar to SEM. The scanning mode operation can be used to look at the beam passing directly through the sample, referred to as the bright field mode. A more useful technique for studying structures with different material compositions is to look at the diffracted beam intensity in STEM mode. To do this, an electron sensitive ring detector is placed below the sample, such that the electrons diffracted at a high angle will intersect it. This ring detector is called the high angle annular dark field (HAADF) detector. The intensity of the diffracted beam depends on the size of the atom with which it interacts, with heavier atoms diffracting the electron beam at higher angles than lighter atoms. This provides Z-contrast over STEM images, allowing the analysis of dimensions of QDs embedded within NWs. An example of this imaging technique is shown in Figure 3.2a.

2.4 Micro-Photoluminescence

Photoluminescence is a radiative recombination process of excited electron-hole pairs (EHP). It is a useful technique for studying the band-structure of semiconductor materials. A continuous wave laser source is used to generate EHPs within the material, which quickly thermalize from their high energy state to the lowest available energy level within the band structure of the material. From here, the EHPs find either a radiative or a non-radiative path to recombine. By using a microscope objective to image the sample, focus the laser to a specific spot, and collect the luminescence from that spot, it is possible to study single NWs. This technique is referred to as micro-photoluminescence (μPL). The setup used in this work is shown in Figure 2.6.

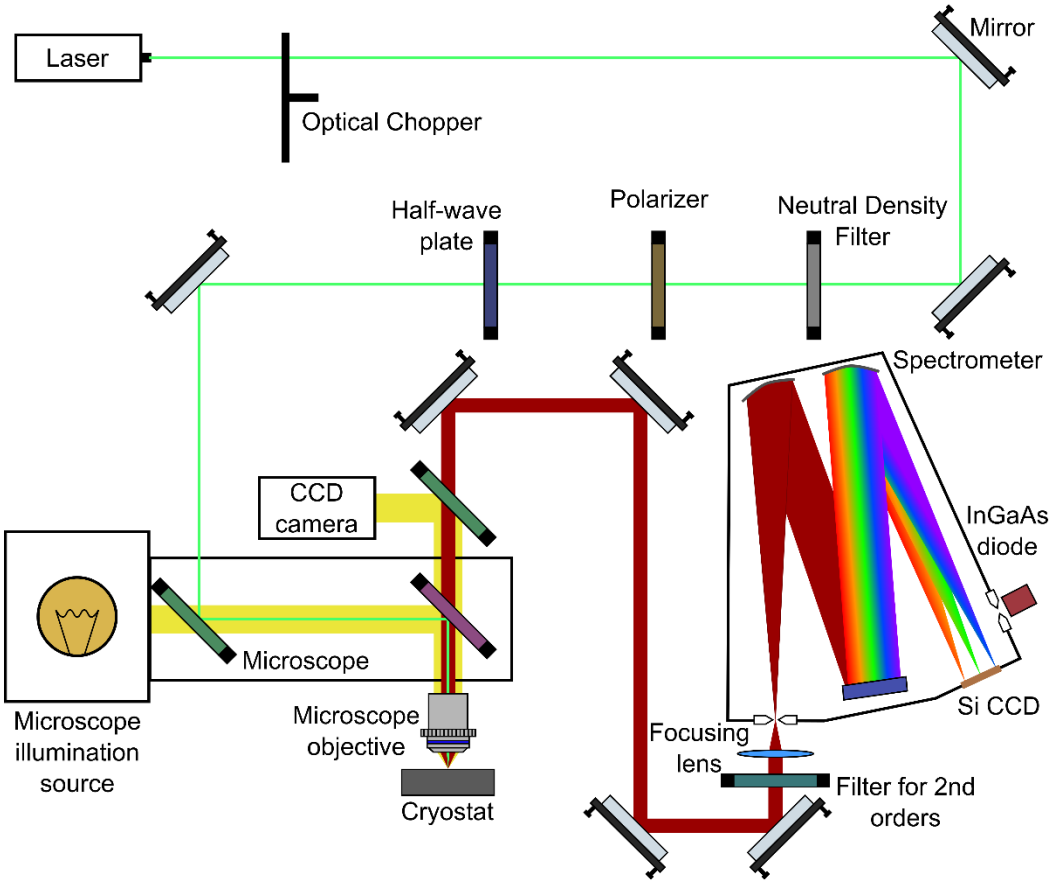

Figure 2.6: The low temperature μPL setup used for characterizing single NWs. The sample is cooled to a temperature below 10K inside the cryostat. The use of a microscope allows the excitation and collection of signal from single NWs dispersed over a Si substrate.

One of two continuous wave lasers is used for excitation. The first is a HeNe laser from Newport Corporation (R-30995) operating at 632.8 nm at a power of 17 mW. The second is a tunable Ar-ion laser from Melles Griot (35LAP431208) operating at 488 nm at a power of 130 mW. The lasers are linearly polarized with an extinction ratio of 500:1. The Ar-ion laser power output is tunable with a potentiometer, along with a series of neutral density filters (providing output from 0.01% to 33% of full power), which allows power-dependence experiments to be conducted.

A Czerny-Turner spectrometer from Horiba Jobin Yvon (iHR550) is used in this setup[1]. The spectrometer has a focal length of 0.55 m and an aperture of f/6.4. The resolution of the spectrometer is 0.025 nm when using a point detector with exit slits set to the smallest width. The resolution is reduced when using an array detector.

The optics are selected to accommodate an operating range of 520-2100nm. Two objective lenses are used to cover this range. The visible and near-IR range is covered by an Olympus 60x objective (LUCPLFLN 60x)[2], which has a transmission of greater than 80% from 380-800 nm. The objective has a numerical aperture of 0.7 and a working distance of 1.5-2.2 mm. The near and mid-IR range is covered by a Newport 36x reflective objective (50102-02)[3]. The objective has a numerical aperture of 0.52 and a working distance of 10.4 mm.

The spectrometer has two output ports, one with automated exit slits, for use with different detectors. The first detector is a back illuminated Si CCD array detector from Horiba Jobin Yvon (Symphony II, BIVS, 1024x256 pixels)[4]. The Si detector is liquid nitrogen cooled to reduce dark current. The second detector is an InGaAs diode detector from Electro-Optical Systems (IGA-1.9)[5], which is also liquid nitrogen cooled. The InGaAs diode is operated using a lock-in amplifier technique. The excitation laser light is modulated using an optical chopper from

[1] http://www.horiba.com/scientific/products/optical-spectroscopy/spectrometers-monochromators/ihr/ihr550-imaging-spectrometer-200/ (accessed July 2017).

[2] https://www.olympus-lifescience.com/en/objectives/ucplfln/ (accessed July 2017).

[3] https://www.newport.com/p/50102-02 (accessed July 2017).

[4] http://www.horiba.com/scientific/products/optical-spectroscopy/detectors/scientific-cameras-for-spectroscopy-cdd-ingaas-emccd/ccds/details/symphony-ii-ccd-detectors-214/ (accessed July 2017).

[5] http://www.eosystems.com/uv-visnir-detector-components.html (accessed July 2017).

New Focus (3501, now provided by Newport)[1], which provides a reference frequency to a Stanford Research Systems (SR810)[2] lock-in amplifier.

The PL emission intensity from semiconductor samples is reduced at room temperature due to the more probable non-radiative recombination processes in the presence of room temperature phonons. To overcome this limitation, the samples are cooled using liquid helium to below 10 K. The cryostat used in this work is a Janis ST-500[3] continuous flow cryostat. An evacuated transfer line is placed inside a helium dewar, which builds up pressure inside the vessel, forcing helium through the transfer line. The transfer line is connected to a tube within the cryostat, which winds around the sample stage, allowing the flowing helium to collect heat from the sample. The helium is collected in a closed loop system and recycled for future use. The cryostat is evacuated in order to obtain cryogenic temperatures, with a heat shield present to minimize the heating of the stage. The temperature at the sample stage is measured using a Si diode connected to a Lakeshore 331[4] temperature controller.

2.5 Device Processing

Once the NWs are characterized using electron microscopy and photoluminescence, they can be contacted electrically for further analysis. There are two approaches for this: contacting single NWs or ensemble devices. Single

[1] https://www.newport.com/f/phase-locked-optical-choppers (accessed July 2017).
[2] http://www.thinksrs.com/products/SR810830.htm (accessed July 2017).
[3] https://www.janis.com/ (accessed Sept 2017).
[4] https://www.lakeshore.com/products/Pages/default.aspx (Accessed Sept 2017).

NWs are sonicated in solution to remove them from the growth substrate and dispersed over an insulating Si substrate covered by a thick oxide layer. EBL or FIB deposition can be used to locate the individual NWs and make electrical contact to large metal pads. Ensemble devices can be processed using a planarization technique, studied in detail by A.C.E. Chia and R.R. LaPierre [70].

Creating a top contact to NWs is a challenge because sputtering or evaporation of metals or transparent conductive oxides does not coat NWs uniformly, leading to a very large sheet resistance for the contact layer. One technique for overcoming this is to use a transparent polymer to surround the NWs, and expose just the tip above the now planar surface. The transparent polymer used in this work is Cyclotene 3022-35[1], also known as bisbenzocyclobutene (BCB), from the Dow Chemical Company.

A small quantity of BCB is placed in a beaker under vacuum for approximately 1 min to draw out any gaseous impurities present. The sample is placed on a spinner bench, and the BCB is deposited on top of the NWs using a syringe. The sample is allowed to sit for 5 min in order for the BCB to uniformly cover the space between the NWs, and then spin-coated at 5000 rpm with a 300 rpm/s ramp rate for 77 s. The sample is soft baked at 100 ^{o}C for 90 s. It is then placed inside a nitrogen glove box, with an O_2 content of <1 ppm, and hard baked at 250 ^{o}C for 30 min, with a ramp rate of 250 ^{o}C/hr (approximate ramp time of 45 min). Through these processes, the BCB fully covers the NWs (depending on the NW height), and must be etched back using reactive ion etching (RIE) to expose

[1] http://www.dow.com/cyclotene/prod/302235.htm (Accessed Sept 2017).

the tips. The sample is etched with 1:1 O_2:CF_4 at a pressure of 180 mTorr (~50 mTorr base pressure) at 50 W. For GaP NWs with an average height of roughly 1.5 μm an etch time of 5 min is sufficient to expose the tips.

If the sample to be contacted is passivated, then the passivation shell is removed prior to further processing through either a wet chemical or RIE etch. Once the passivation shell is removed, the contact pattern is defined using standard photolithography procedures inside a clean room. Once the pattern is developed, 250 nm of indium tin oxide (ITO) is sputtered, followed by 25:50:225 nm of e-beam evaporated Ni:Ge:Au on an ITO area away from the NW pads. On the back side of the sample 250 nm of Al is sputtered. The sample is then annealed for 1 min at 400 ^{o}C.

2.6 Electrical Measurements

2.6.1 Current-Voltage (IV) Characterization

Electrical IV characterization is performed with either a two-point or a four-point probe configuration using a Keithley 2400 sourcemeter. The system is used to sweep the voltage while simultaneously measuring the current through the device. The setup allows for measuring the device in the dark or under a 1 sun (AM1.5G) illumination, using a Newport 96000 lamp. The sample is rested on an aluminum foil stage for the back side contact and is contacted using a precision controlled electrical needle probe. The samples are measured in the dark and

under illumination to extract properties such as diode characteristics, resistivity, and the response to illumination.

2.6.2 Photocurrent Measurements

Photocurrent measurement as a function of wavelength provides information about the absorption mechanisms within the samples. In the case of solar cells, this technique provides insight into some of the loss mechanisms in the absorption of light and the collection of the photogenerated carriers. In the case of characterizing QDs embedded within NWs [87], the absorption within the QDs is analysed, which occurs below the bandgap of the host material.

The iHR550 from Figure 2.6 is repurposed for the photocurrent measurement setup, shown in Figure 2.7. The broadband source is a quartz tungsten halogen (QTH) 100 W lamp (Newport 6333), which is focused onto the entrance slits of the spectrometer using a lens. A dielectric filter is used to remove diffracted second orders from the source. The dispersed light at the exit is collimated using another lens, and guided using a mirror onto the sample. An optical chopper from New Focus (3501, now provided by Newport) is used to modulate the excitation light, and also provides a reference signal to the SR810 lock-in amplifier from Stanford Research. The sample is biased using a Keithley 2400 source meter.

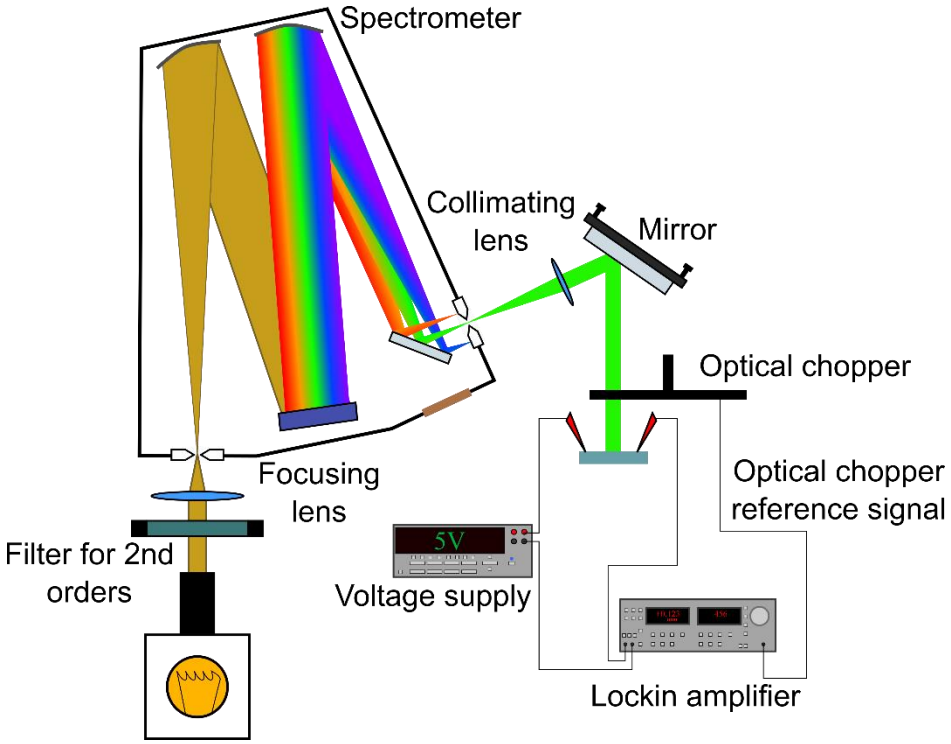

Figure 2.7: Photocurrent measurement setup. The iHR550 spectrometer is used to disperse broadband light from the illumination source. A lock-in amplifier is used to measure the small signals from NW samples.

The output spectrum from this system is a function of the response of individual optical components, such as the lenses, mirrors, and gratings as well as the spectrum of the QTH source itself. In order to obtain absolute values of external quantum efficiency (EQE) in the case of solar cells, or responsivity in the case of photodetectors, a wavelength calibrated power meter must be used. The Newport 2936-C power meter is placed at the location of the sample to measure the optical power incident on the sample. The range of the power meter used in this work is from 400 to 1100 nm, which is the limiting factor of the wavelength coverage of this setup.

3. InAsP QDs Embedded within InP NWs on Si

In this chapter the growth and characterization of InAsP QDs embedded within InP NWs is presented. Section 3.1 contains an introduction to this topic and outlines the motivation for this study. Section 3.2 summarizes the growth and device fabrication of the InP/InAsP NWs on Si. The NWs were grown using Au seed particles on an un-patterned substrate, which results in a random distribution of position and diameters of NWs. The 5 samples which were prepared are InP NWs without QDs and NWs with 15 $InAs_xP_{1-x}$ QDs added in the middle of the NWs during growth, with a composition of $x = 0.25, 0.5, 0.75$, and 1. Section 3.3 contains the analysis of these samples, with discussion on SEM and TEM results, PL, and electrical measurements. A growth model is presented, which uses the InAsP QD axial height and InP barrier height, as measured by HAADF STEM, to comment on the growth mechanisms of this system. This chapter contains work from "Photoluminescence and photocurrent from InP nanowires with InAsP quantum dots grown on Si by molecular beam epitaxy" by P. Kuyanov and R.R. LaPierre, published in Nanotechnology Vol 26, Issue 31 (2015) p. 315202 [87].

3.1 Introduction

QDs have been demonstrated in various applications such as infrared photodetectors or cameras [65,88]. Conventional techniques for fabricating semiconductor QDs include solution-based techniques [89] and the SK [66]

growth method. The SK method relies on the strain between two lattice-mismatched materials. Once a critical thickness is exceeded, the strain is relieved by the random formation of QDs. This type of growth typically results in a wetting layer which can lead to a continuum of unbound states within the absorption spectrum of the QDs [90]. In addition, the random nature of the dimensions and location of these QDs make this approach undesirable for some applications.

An alternative method for the growth of QDs is the use of group III-V semiconductor nanowires (NWs), such as large bandgap InP NWs containing smaller bandgap InAsP QD insertions [19,67,72,75,91–100]. Such an architecture can address many of the problems facing conventional methods of growing QDs, such as the presence of wetting layers, restrictions in material combinations due to lattice mismatch, or control of QD dimensions. Semiconductor NWs are typically grown using the vapor-liquid-solid (VLS) method by utilizing a Au seed particle for the collection of the impinging growth species [19,72,91,95–99], but can also be grown by self-assisted growth [93], selective-area epitaxy (SAE) [92], or Au-assisted SAE [75,94]. InP NWs with InAsP QDs have interband transitions within the infrared (IR) range, which is of particular interest for applications in photodectors and single photon sources.

Our previous work focused on the mechanisms of InAs QD growth within InP NWs using molecular beam epitaxy (MBE) [19]. The NWs were grown using randomly arranged Au seeds on a (111)B InP substrate. The present paper focuses on InP NWs with InAsP QD insertions grown by MBE on a Si (111) substrate.

The use of inexpensive Si (111) substrates could enable integration of III-V devices, such as photodetectors and single photon sources, with Si electronics. We demonstrate tuning of the peak photoluminescence (PL) emission from InAsP QDs by adjusting the alloy composition of the QDs. We also show that the peak absorption wavelength in photocurrent devices made from NW ensembles can likewise be tuned by the QD composition. Previous reports [72,91,93,98] have demonstrated the tuning of QD PL emission by adjusting the QD composition or dimensions, but none of these reports showed wavelength tuning of the photocurrent in electrical devices as reported here.

3.2 Experimental Details

InP/InAsP/InP axial NW heterostructures were grown by the Au-assisted vapor-liquid-solid (VLS) method in a gas source MBE system. Si (111) boron-doped wafers from Virginia Semiconductor with a resistivity <0.001 Ω-cm were submerged for 60 s in a buffered hydrofluoric (BHF) acid solution, removing the native oxide. The substrate was rinsed under flowing de-ionized (DI) water for 2 min, and dried using nitrogen. The substrate was then immediately transferred to an e-beam evaporation system where 1 nm of gold was deposited at room temperature at a rate of 1 Å/s. Prior to growth, the wafers were placed in a pre-deposition chamber where they were degassed for 15 min at 300 °C. After transferring the wafers to the MBE growth chamber, the substrates were heated to 420 °C under inductively coupled hydrogen plasma and P_2 overpressure for 10

min, leading to the formation of Au nanoparticles. The MBE system used solid source effusion cells for In and Al, while the group V species were As_2 and P_2 derived from the dissociation of phosphine (PH_3) and arsine (AsH_3) in a gas cracker operating at 950 ^{o}C. NWs were grown with InP/InAsP/InP axial heterostructures, and encapsulated with an $Al_{0.1}In_{0.9}P$ shell. NW growth was initiated at 420 °C by opening the In shutter with a V/III flux ratio of 3.7. All segments were grown at a 2-D equivalent growth rate (group III impingement rate) of 0.14 nm/s. The first InP segment was grown for a duration of 25 min, followed by the InAsP QD segment. Each InAsP QD segment was grown by terminating the In supply, and immediately adjusting the P_2 and As_2 flux as required for each nominal composition ($InAs_{0.25}P_{0.75}$, $InAs_{0.50}P_{0.50}$, or $InAs_{0.75}P_{0.25}$) while maintaining the V/III flux ratio at 3.7. After waiting for a period of 25 s, the In shutter was re-opened to initiate growth of the InAsP QD. The purpose of the waiting period is to establish the desired concentrations of both P and As within the Au droplet prior to the growth of the QD, which reduces composition gradients at their interfaces. After growing the InAsP segment for a duration of 2 s, the In and As_2 flux were immediately terminated, and the P_2 flux was increased to restore the V/III flux ratio to 3.7. After a pause of 25 s, the In shutter was then opened to resume the growth of InP. NWs were grown with either a single QD, or the above process was repeated to produce NWs with multiple QDs. The InP barriers between QDs were grown for a duration of 5 s. QDs were grown with nominal compositions (based on this film calibrations) of $InAs_{0.25}P_{0.75}$, $InAs_{0.50}P_{0.50}$ and $InAs_{0.75}P_{0.25}$. A sample consisting of 4 InAs QDs

was also grown, as discussed in the *Growth Model* section. The nominal compositions were based on thin film calibrations. After growing the QDs, the axial structure was terminated with InP of 10 min duration. The NWs were passivated with a larger bandgap shell of nominal composition $Al_{0.1}In_{0.9}P$, similar to that reported previously [100]. The growth was terminated by cooling the sample under a P_2 overpressure.

The NW morphology and density were determined by a JEOL 7000F scanning electron microscope (SEM). The NW structure was investigated in a JEOL 2010 high resolution scanning transmission electron microscope (TEM) in bright field or high angle annular dark field (HAADF). The NWs were removed from their growth substrate for TEM investigation by sonication in a methanol solution. The solution was then transferred to the TEM holey carbon grid. Chemical composition was determined in the TEM by energy dispersive X-ray spectroscopy (EDX) using $K_{\alpha 1}$ transitions.

The NWs were removed from their growth substrate for micro-photoluminescence (μPL) by sonication in methanol followed by random dispersion onto a Si substrate covered by thermally grown 300 nm thick silicon dioxide. PL was measured at room temperature or at 10 K in a liquid helium flow cryostat. Individual NWs were examined using a 36× reflective objective with N.A. 0.52. A He-Ne laser (λ=632.8 nm) with polarization parallel to the NW length was used as the excitation source with irradiance of 320 W/cm^2. Spectra were collected by a 0.55 m Horiba Jobin Yvon spectrometer and dispersed onto a LN_2 cooled Si CCD detector or InGaAs photodiode.

3.3 Results and Discussion

3.3.1 SEM

A representative SEM image is shown in Figure 3.1 for the sample with 4 QDs with nominal composition of InAs. The NW morphology was rod-shaped with some tapering near the NW tip. SEM images similar to Figure 3.1a and b were used to estimate the surface density, height and diameter of the NWs. The average and standard deviation of the NW surface density was (6±3) x 10^8 cm^{-2}, obtained by inspecting plan view SEM images across the entire sample surface. The average and standard deviation of the NW diameter, averaged over 83 NWs in cross-sectional SEM images similar to Figure 3.1b obtained across the entire sample surface, was 60 ± 10 nm. Similarly, the average and standard deviation of the NW height, obtained from the same 83 NWs, was 2.6 ± 0.3 µm. These length measurements are under-estimated because they neglect the possible tilt of the NWs out of the plane of the SEM image. SEM images such as Figure 3.1 indicated that 23% of NWs grew preferentially in the vertical direction (orthogonal to the substrate surface). The remaining NWs grew in various tilted directions. Similar results (density, diameter, length, morphology, growth directions) were obtained for all of the samples with different QD compositions.

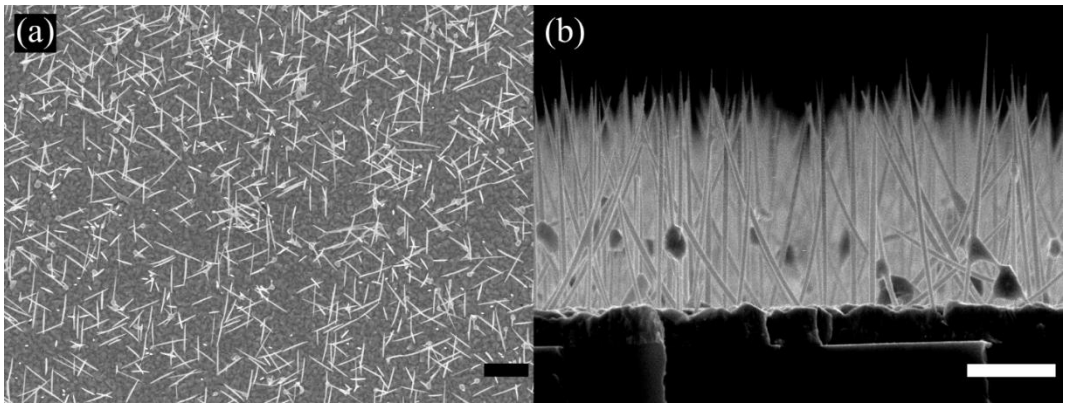

Figure 3.1: (a) Plan-view, and (b) cross-sectional SEM image of NWs containing 4 QDs with nominal composition of InAs. Scale bar is 2 μm in (a) and 1 μm in (b).

3.3.2 TEM

Figure 3.2a shows a HAADF TEM image of a single InP NW containing 15 QDs with nominal composition of $InAs_{0.25}P_{0.75}$. The QDs, indicated by red arrows in Figure 3.2a, are visible as a bright contrast in the HAADF TEM image. The average height of the QDs along the growth direction, estimated directly from TEM images in over 90 QDs among 6 NWs for each of the samples, was 4 ± 1 nm, 6 ± 2 nm and 6 ± 1 nm for the nominal composition of $InAs_{0.25}P_{0.75}$, $InAs_{0.50}P_{0.50}$ and $InAs_{0.75}P_{0.25}$, respectively. The inset in Figure 3.2b shows a selected area diffraction pattern obtained using a 75 nm aperture centered in the field of view of Figure 3.2b. The diffraction pattern indicates a wurtzite crystal structure. Bright field TEM images, as in Figure 3.2b, showed alternating dark and bright contrast stripes crossing the NW, indicating the presence of stacking faults (short zincblende insertions) within the primarily wurtzite crystal structure, which is also evident as streaking between diffraction spots in the wurtzite

diffraction pattern. A significant number of NWs had the stacking faults isolated to the InP segments above and below the QDs region, with the InAsP QD region of the NWs being nearly stacking-fault-free. The termination of the stacking faults in the InP segment beneath the QDs is indicated in Figure 3.2a and b by the lower, right-hand green arrow in both images. A stacking fault located in the QD region is indicated in Figure 3.2a and b by the left-hand green arrow in both images. Formation of stacking faults is a function of droplet geometry, growth conditions, and material selection.

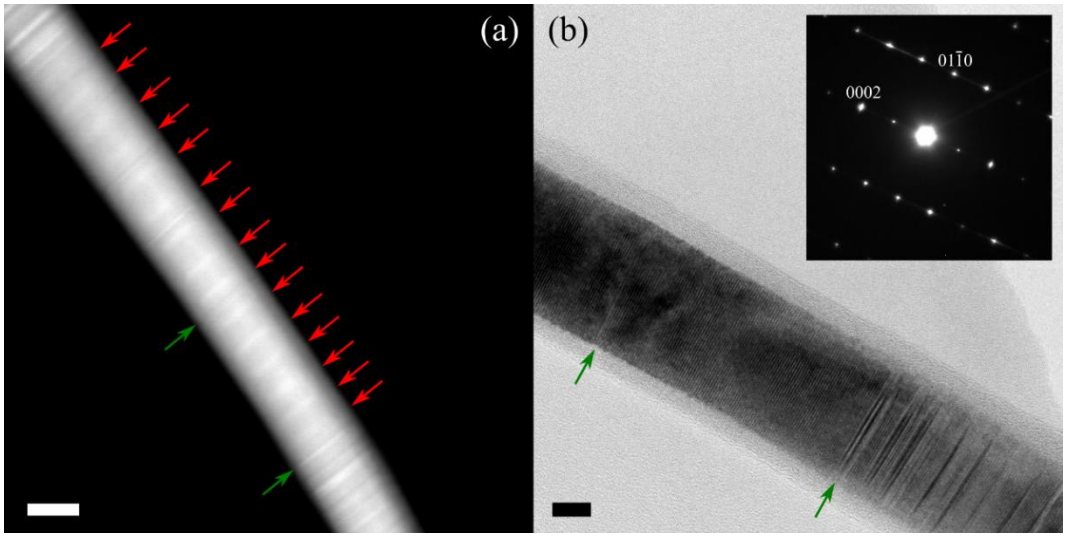

Figure 3.2: (a) HAADF image of InP NW with 15 QDs of nominal composition $InAs_{0.25}P_{0.75}$. (b) Bright field TEM image of the same NW. Scale bars are 20 nm and 10 nm for (a) and (b), respectively. Inset in (b) shows a selected-area diffraction pattern. The red arrows in (a) indicate the location of the QDs, and the green arrows in both images indicate the identical stacking faults.

3.3.3 EDX

EDX linescan measurements were performed along the length and diameter of the NWs. Figure 3.3a and b show a representative EDX linescan along the axis and diameter, respectively, of a NW containing a single QD with nominal

composition of InAs, superimposed on a HAADF TEM image. The linescans shows an increase in As counts and decrease in P counts, coincident with the bright contrast in the HAADF TEM images, indicating the presence of the QD. The linescan in Figure 3.3b shows the presence of excess P near the NW edge and a small amount of Al, due to the $Al_{0.1}In_{0.9}P$ shell encapsulating the QD. The thickness of the $Al_{0.1}In_{0.9}P$ shell, as measured from the HAADF TEM images in 23 NWs among all of the samples (with nominal QD composition of $InAs_{0.25}P_{0.75}$, $InAs_{0.50}P_{0.50}$, or $InAs_{0.75}P_{0.25}$), was 8 ± 3 nm. More detailed studies of AlInP shells were presented in Ref. [100].

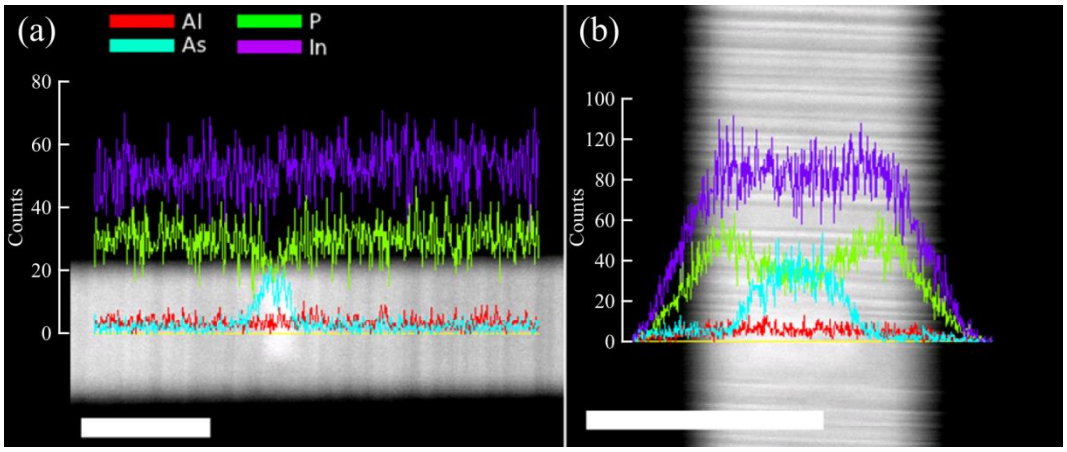

Figure 3.3: HAADF image of single QD (bright region) with nominal composition of InAs, and a superimposed EDX linescan along (a) the NW axis and (b) the NW diameter. Scale bar is 50 nm.

3.3.4 InAsP Composition

In addition to the QD samples, InP/InAsP heterostructures were grown containing long InAsP segments without any AlInP shell. The long InAsP segments were used to examine the interface between InP and InAsP, as well as obtain an estimate for the InAsP alloy composition. A representative TEM image

and the associated EDX linescan are shown in Figure 3.4 for an InP/$InAs_{0.75}P_{0.25}$ NW heterostructure. Similar results were obtained for NW segments with nominal composition of $InAs_{0.25}P_{0.75}$ or $InAs_{0.50}P_{0.50}$. The absolute As composition determined by EDX for the three samples (with nominal $InAs_{0.25}P_{0.75}$, $InAs_{0.50}P_{0.50}$, or $InAs_{0.75}P_{0.25}$ segments) was 32%, 49% and 85%, in reasonable agreement with the nominal composition of 25%, 50% and 75%, respectively. The samples exhibited a gradient in composition across the heterostructure interface over a length of less than ~15 nm. Similar results have been observed in the growth of InAs/GaAs NWs grown by metalorganic vapor phase epitaxy [67]. Although the dimensions of the QDs were too small to accurately determine composition by EDX, the composition gradient in Figure 3.4, which is on the same scale as the QD dimensions, indicates that each QD may have an inhomogeneous composition along the NW length.

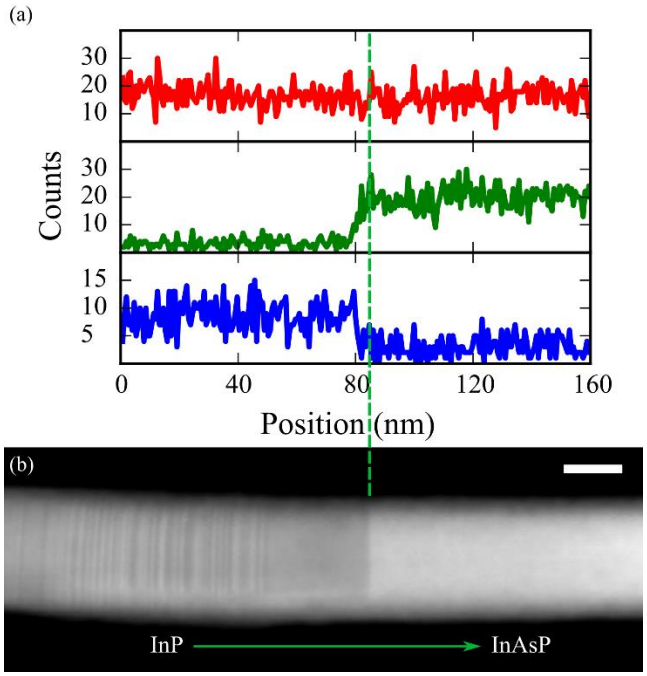

Figure 3.4: (a) EDX linescan for InP/InAs$_{0.75}$P$_{0.25}$ NW heterostructure; In: red, As: green, P: blue. (b) HAADF image of the NW. The scale bar is 20 nm.

3.3.5 Growth Model

To investigate the growth method of the QDs, a sample with 4 InAs QDs was grown with growth durations of 5, 7.5, 12.5 and 17.5 s. The InP barrier between each QD had a growth duration of 40 s. A representative HAADF TEM image of a NW is shown in Figure 3.5 (growth is from left to right), with the bright areas corresponding to the InAs QDs (confirmed by EDX measurements, not shown). TEM images, similar to Figure 3.5, were used to determine the InAs and InP segment lengths. Figure 3.6 shows the measured segment lengths versus NW diameter, measured over 25 NWs, for the 4 InAs QDs and the 3 InP segments between the QDs. The diameter was measured at the position of the first QD, and was found to be identical for the other segments in each NW. The uncertainty of the QD length and diameter was +/- 1 nm.

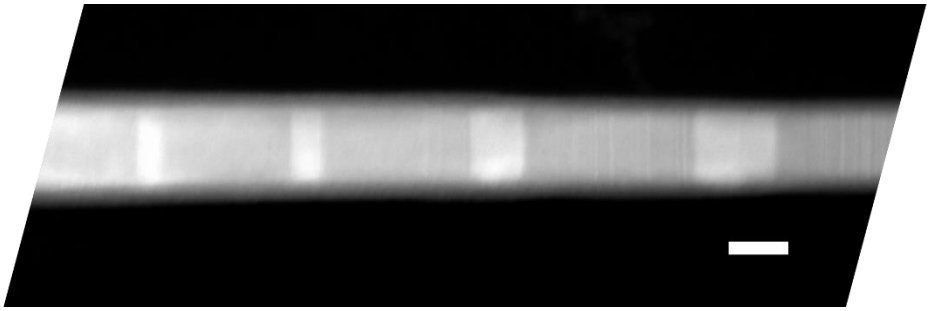

Figure 3.5: HAADF TEM image of InAs QDs (bright regions) grown for t = 5, 7.5, 12.5 and 17.5 s (left to right). The scale bar is 20 nm.

Our previous study of InAs NWs grown by MBE indicated that the growth rate of NW segments is dominated by two effects: (1) the purging of group III material from the Au droplet during the gas switching sequence at each interface, and (2) the growth is group V limited, such that an increase in group V impingement on the Au droplet results in a larger axial growth rate of the NWs [19].

Using a simple material conservation principle, the contribution of the first of these effects to the length of the NW segment, L, was expressed as [19]:

$$L = C\Delta X_{In} D \quad (1)$$

where D is the Au droplet diameter, ΔX_{In} is the fractional change in atomic concentration of In atoms in the droplet due to purging during each growth interruption (estimated to be 14% from Ref. [19]), and C=1.18 for InAs and 1.07 for InP [19]. The parameter, C, depends only on the material densities and the equilibrium In concentration in the droplet, X_o, which we assume is the same as

Ref. [19]. We expect that ΔX_{In} depends primarily on the dwell time at each interface (25 s), which was the same here as Ref. [19]. Eq. (1) predicts a linear increase in NW length with droplet diameter, which is indeed observed in Figure 3.6. However, Eq. (1) only predicts the NW growth that occurs during the growth interruption (due to the purging of material from the Au droplet, which is acting as an In reservoir) and does not predict the increasing InAs segment length with the growth duration as seen in Figure 3.6. Figure 3.6 clearly shows that the length of the InAs segments increases with their growth duration (black = 5 s of InAs, red = 7.5 s of InAs, green = 12.5 s of InAs, blue = 17.5 s of InAs and purple/light blue/yellow = 40 s of InP).

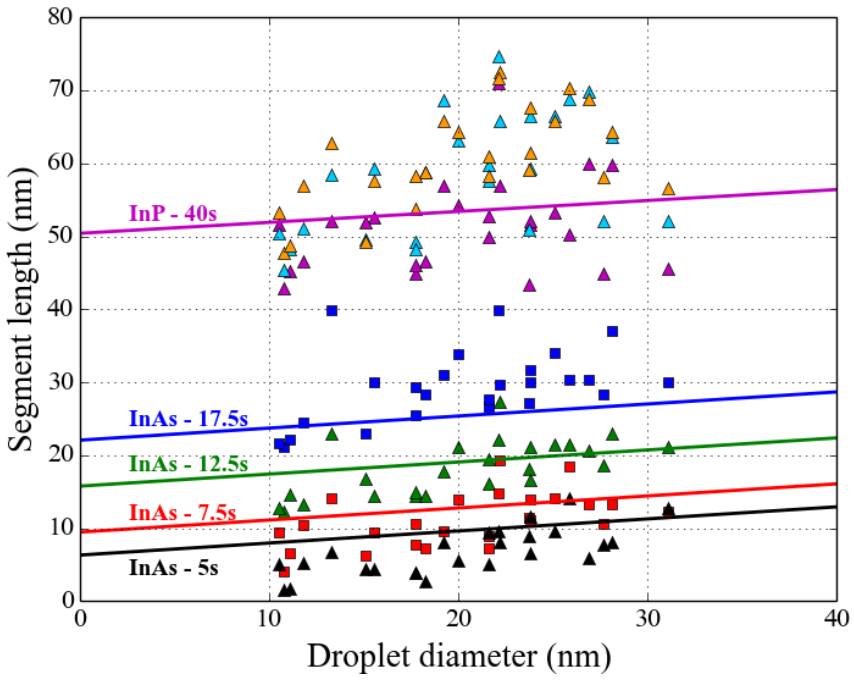

Figure 3.6: Segment length versus droplet diameter for different growth durations; black triangles: 5 s growth of InAs QD; red squares: 7.5 s growth of InAs QD; green triangles: 12.5 s growth of InAs QD; blue squares: 17.5 s growth of InAs QD. The InP 40 s segments between QDs are further subdivided into the first (purple triangle), second (light blue triangle) and third (yellow triangle) segments.

In our previous work [19], we reported a model for growth of vertically oriented InP NWs, containing InAs QDs, on InP (111)B substrates. In that case, we described the growth of InAs QDs as being due primarily to purging of In from the Au droplet as well as by direct impingement of adatoms on the Au droplet. Recent analysis [101], however, has shown that, besides the directly impinging group V flux on the droplet, a secondary source of group V flux can arise due to desorption from the substrate surface between NWs. We recently elaborated this growth model to explain the growth of InAs NWs [102]. In the present paper, we adjust our previous growth model of InAs QDs [19] to account for this secondary flux of group V material. Note that, because the NW growth is group V limited, adatom diffusion does not play a significant role (the diffusion length of group V material is negligible), as described previously [102].

Assuming the growth to be group V limited, the simplest time dependence of NW length arises by modifying Eq. (1) to include the directly impinging group V flux (L_o):

$$L = L_o + C\Delta X_{In} D \quad (2)$$

In the simplest model, L_o is given by FRt where F is the group III impingement rate, R is the V/III flux ratio, and t is the growth duration. However, this flux is insufficient to account for the large growth rates observed in Figure 3.6. For example, for our InP segments, using the same growth parameters as Ref. [17,19], F = 0.14 nm/s, R = 3.7 and t = 40 s resulting in a segment length of only 21 nm, which is less than half of that observed in Figure 3.6. Hence, to

sustain such a large NW growth rate, an additional source of group V material to the droplet must arise. In Ref. [19], we previously considered this contribution to arise from adatom diffusion. However, as mentioned above, we now consider the NW growth to be group V limited and the group V diffusion length to be negligible. Instead, the additional source of group V material is explained in terms of re-evaporation of the incident flux from the substrate surface surrounding each NW; i.e., group V material impinging on the substrate surface can re-evaporate and impinge on the Au droplet [101,102]. The NW length can now be expressed as:

$$L = FR't + C\Delta X_{In}D \tag{3}$$

where R' is the modified V/III flux ratio due to both direct impingement on the droplet and the re-evaporation flux from the substrate surface. Note that there may also be a contribution due to re-evaporation from the sidewalls of adjacent NWs.

The lines in Figure 3.6 are fits to the data using Eq. (3) with $R' = 9$ and $\Delta X_{In} = 0.14$. This represents a 2.4-fold increase in group V impingement on the droplet compared to the directly impinging flux alone (R=3.7). The increased group V impingement has been observed to be at least 2.1 for the growth of GaAs NWs [101], which agrees well with our results. The dispersion in the data of Figure 3.6 is likely due to the random positioning of the NWs. This random positioning results in different adatom collection areas surrounding each NW; i.e., each NW will collect different group V material desorbing from the substrate surface or the

surface of adjacent NWs. The various tilt directions of the NWs will also result in different impingement rates of the scattered or directly impinging molecular beams. Less scatter in the data would be expected from a periodic array of vertical NWs, achieved in selective-area epitaxy. This simple model does not fit the shorter InAs segments as well, indicating the presence of growth time dependent effects, such as incubation time of growth, which were not investigated in this study.

3.3.6 Photoluminescence

To reduce carrier depletion of the NWs and prevent non-radiative recombination on the NW sidewalls due to surface states, it is necessary to encapsulate the NWs in a shell of larger bandgap material. Perhaps the most studied material system is GaAs NWs passivated using various III-V materials, including AlInP [103], GaP [78,104], InGaP [105] and AlGaAs [106]. The passivation of InAs QDs is usually achieved using an encapsulating shell of InP [72,75,91–99]. In the present study, the InP/InAsP/InP axial NW structure was encapsulated in a larger bandgap shell of $Al_{0.1}In_{0.9}P$, as described previously [18]. The effectiveness of the surface passivation in the present study was assessed by measuring μPL from single InP NWs grown with and without the $Al_{0.1}In_{0.9}P$ passivation shell (Figure 3.7). TEM and selected-area diffraction measurements (not shown) indicated that the crystal structure of these InP NWs was similar to the long InP segments at the base of NWs in the QD samples; i.e., they are primarily wurtzite with short zincblende insertions (stacking faults). The InP NW with an AlInP passivation shell showed a peak PL intensity which was more than

one order of magnitude greater than that from an unpassivated InP NW, demonstrating the effectiveness of the passivation.

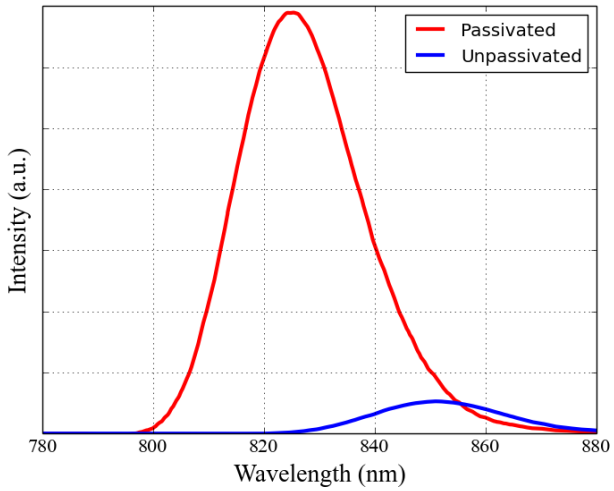

Figure 3.7: 10 K μPL of passivated and unpassivated single InP NWs.

The μPL on unpassivated single InP NWs showed a μPL peak located at 850 nm (1.46 eV), corresponding to the wurtzite crystal structure as described previously in Ref. [107]. The passivated NWs in this study exhibited a blue shift in the PL peak position from 850 nm to 825 nm (a 46 meV shift), which could be attributed to the lattice mismatch strain of the core-shell InP/AlInP structure. Similar strain-related blue shifts were observed with GaAs/GaP [78,104], GaAs/InGaP [105] and InAs/InP [108] core-shell NWs.

The μPL from single InP NWs containing QDs were measured at 10 K. Four samples were investigated, containing either 15 $InAs_{0.25}P_{0.75}$ QDs (similar to Figure 3.2), 15 $InAs_{0.50}P_{0.50}$ QDs, 15 $InAs_{0.75}P_{0.25}$ QDs, or 4 InAs QDs (similar to Figure 3.5). The NWs were passivated with $Al_{0.1}In_{0.9}P$ shells. No PL was

detectable from QDs in NWs without passivation. Figure 3.8 shows the μPL spectra of the above mentioned samples. In addition, the PL of the single passivated InP NW without QDs from Figure 3.7 is included in Figure 3.8 for comparison. All of the QD samples showed emission above 900 nm, which can be attributed to the QDs. This emission was absent from the InP NWs without any QDs. The emission wavelength from QDs is typically achieved by adjusting the QD dimensions via the quantum confinement effect [91,93,98]. Here, we report the tuning of PL emission wavelength by adjusting the alloy composition of the QD. The PL emission from the InAsP QDs shifted towards higher wavelength with increasing As composition, as would be expected from the decreasing bandgap energy of the alloy. From a simple finite quantum well model [109], the expected electron to heavy-hole interband transition wavelengths were estimated for the four samples. The calculated interband emission wavelengths for the $InAs_{0.25}P_{0.75}$, $InAs_{0.50}P_{0.50}$, $InAs_{0.75}P_{0.25}$ and InAs samples were 880–950 nm, 950-1150 nm, 1000-1400 nm, and 1000-1700 nm, respectively, in reasonable agreement with the observed PL emission. Cathodoluminescence (CL) measurements, reported elsewhere [110], indicated localized emission due to the QDs.

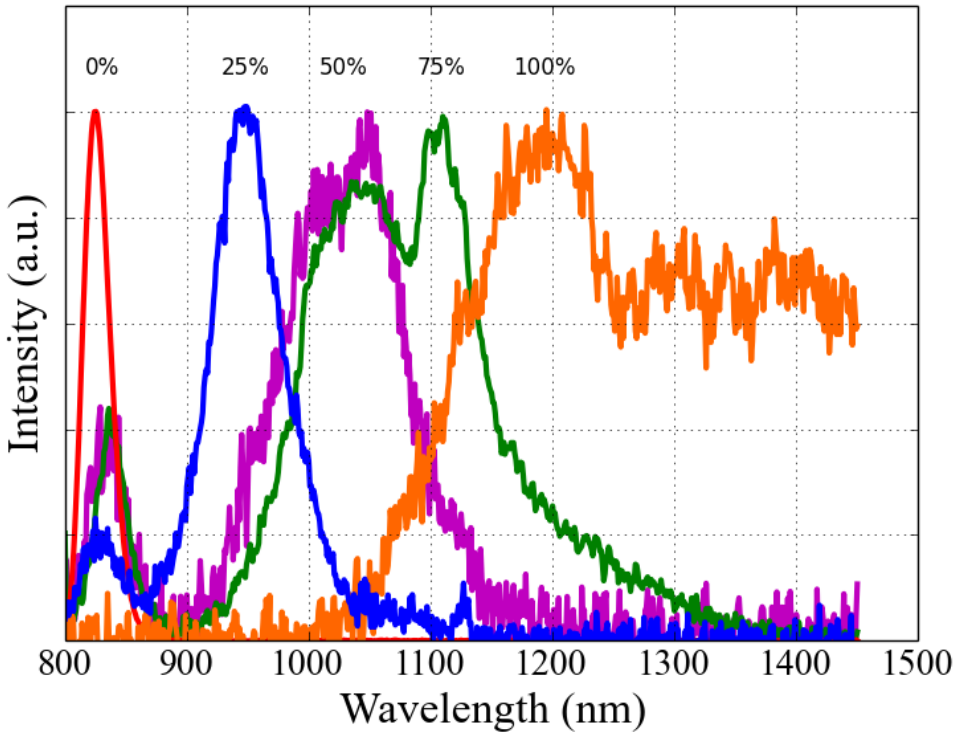

Figure 3.8: 10 K μPL spectra (normalized) obtained from single InP NWs with no QDs (0% As, red), 15 $InAs_{0.25}P_{0.75}$ QDs (25% As, blue), 15 $InAs_{0.50}P_{0.50}$ QDs (50% As, purple), 15 $InAs_{0.75}P_{0.25}$ QDs (75% As, green), and 4 InAs QDs (100% As, orange; as used in Figure 3.5 and 3.6). Some of the samples show double peaks, which indicates that emissions from several energy levels are observed.

Room temperature μPL was also measured on NW ensembles from the same samples. The room temperature μPL, shown in Figure 3.9, demonstrated PL emission that shifted with As composition of the QDs, in a manner similar to Figure 3.8. The room temperature emission was observed at higher wavelengths than the 10 K emission, as expected from the temperature dependence of the bandgap according to the Varshni equation [111].

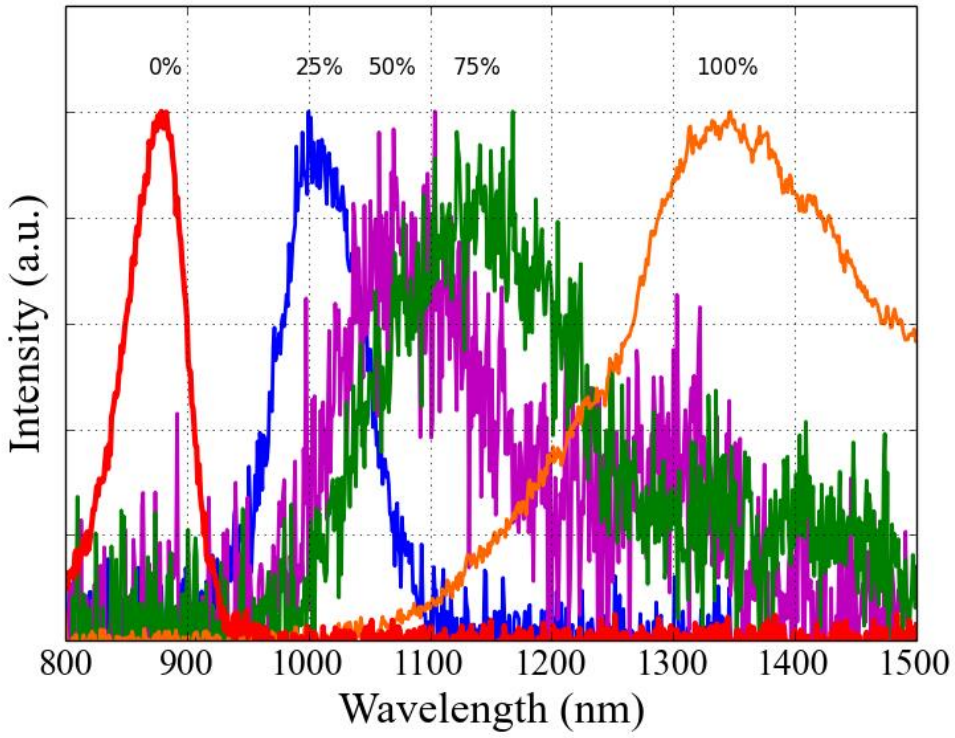

Figure 3.9: Room temperature μPL (normalized) obtained from NW ensembles containing no QDs (0% As, red), 15 $InAs_{0.25}P_{0.75}$ QDs (25% As, blue), 15 $InAs_{0.50}P_{0.50}$ QDs (50% As, purple), 15 $InAs_{0.75}P_{0.25}$ QDs (75% As, green), and 4 InAs QDs (100% As, orange; as used in Figure 3.5 and 3.6). The yield and quality of NWs between the five samples varies, which results in smaller signal to noise levels for some of the samples.

The large linewidth of the PL emission in single NWs containing 15 QDs can probably be attributed to variations in composition among the 15 QDs. Similar broadening of the PL emission has been observed in multiple QD InAsP/InP NWs [72,91,93]. As mentioned earlier, the dimensions of the QDs were too small to accurately determine their composition by EDX. Nevertheless, some variation within each QD composition can be expected due to the gas switching sequence. As described earlier, each InAsP QD segment was grown by terminating the In supply, immediately adjusting the P_2 and As_2 flux as required for each nominal QD composition, and then waiting for 25 s before re-opening the In shutter for 2

s. The reverse procedure was then used for the inverted interface. During these gas switching sequences, In is purged from the Au droplet, as explained earlier in the growth model, probably resulting in compositionally graded interfaces. Further work is required to precisely control the gas switching sequence and therefore the QD composition and abruptness of the interfaces. As discussed earlier, the AlInP encapsulating shell is not lattice-matched to the InP/InAsP core, likely resulting in inhomogeneous strain on the QDs. This strain may be an additional source of broadening in the QD emission. Stacking faults and surface defects have also been documented as contributors to linewidth broadening [93,94].

In addition to the variation of QD composition within a single NW, there is also a variation in QD dimensions (and likely composition) among the multiple NWs of each growth. This is evident, for example, by the scatter of QD dimensions in Figure 3.6. As described earlier, the dispersion in the data of Figure 3.6 is likely due to the random positioning of the NWs. This random positioning results in different adatom collection areas surrounding each NW; i.e., each NW will collect different group V material desorbing from the substrate surface or the surface of adjacent NWs. The various tilt directions of the NWs will also result in different impingement rates of the scattered or directly impinging molecular beams, affecting the QD dimensions among the NWs.

3.3.7 Electrical Measurements

Photodetectors consisting of a single InAs NW [112,113], a single InAs/InAsP heterostructured NW [68], or a single InP NW containing an InAsP QD [99] have been reported. InAs [69] and InAsSb [114] ensemble photodetectors have also been reported [69]. Here, we report ensemble photodetectors based on InAsP multiple (15) QDs embedded in InP NWs. Devices were fabricated by planarizing NW ensembles with cyclotene using a procedure described previously [70]. 250 nm of Al was sputtered on the bottom of the Si substrate. Indium tin oxide (ITO) contact pads of 250 nm thickness and 0.2 cm diameter were sputtered onto the sample to contact the exposed tops of the NWs. To reduce the contact resistance of the electrical probe to the ITO, a smaller diameter (0.1 cm) metal contact dot consisting of 25 nm of Ni, 50 nm of Ge and 200 nm of Au was deposited by e-beam evaporation on top of the ITO pad. This left an aperture area of 0.024 cm^2 through which incident light could pass through the ITO to the NWs. Based on the average NW density of $6x10^8$ cm^{-2}, this aperture area contained ~$1.4x10^7$ NWs. The samples were annealed at 400 ^oC for 30 s using a rapid thermal annealer. The typical ITO sheet resistance was measured to be 20-40 Ω/□. The devices were mounted on a copper foil for electrical measurements. The device schematic is shown in the inset of Figure 3.10b.

Spectrally-resolved photocurrent was measured at room temperature by illuminating the devices with a 100 W quartz tungsten halogen lamp (Newport QTH6333) dispersed by an iHR550 spectrometer and modulated by an optical chopper. Photocurrent was measured by a Keithly 2400 source meter and a

Stanford Research Systems SR810 lock-in amplifier. I-V measurements were performed in the dark and under illumination. The inset of Figure 3.10a shows a typical I-V curve measured from the $InAs_{0.25}P_{0.75}$ QD sample under dark conditions and illumination (λ=600 nm). For the photocurrent measurements, an arbitrary bias of 1V was applied across the NWs (between the NW top contact and the bottom Si contact). Figure 3.10a shows the photocurrent measured as a function of illumination wavelength for the sample with no QDs. The structure below 600 nm in Figure 3.10a is due to variation in the incident light spectrum.

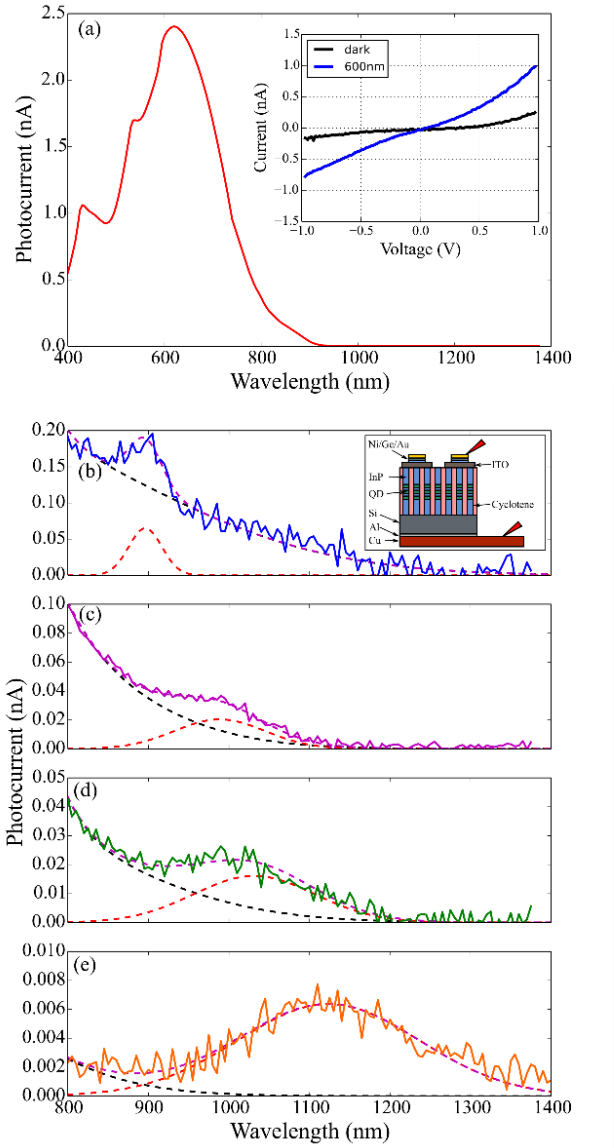

Figure 3.10: Room temperature spectrally-resolved photocurrent measurements obtained from InP NWs with (a) no QDs, (b) 15 $InAs_{0.25}P_{0.75}$ QDs, (c) 15 $InAs_{0.50}P_{0.50}$ QDs, (d) 15 $InAs_{0.75}P_{0.25}$ QDs, and (e) 4 InAs QDs. The total photocurrent (purple dashed line) is deconvolved into a background contribution (black dashed line) and a QD contribution (red dashed line). Inset in (a) shows I-V measurements for the $InAs_{0.25}P_{0.75}$ QD sample for dark and light illumination (λ=600 nm). Inset in (b) shows the device structure with the red probes indicating the photocurrent measurement.

Figure 3.10 b-e shows the photocurrent as a function of illumination wavelength for the four samples: $InAs_{0.25}P_{0.75}$, $InAs_{0.50}P_{0.50}$, $InAs_{0.75}P_{0.25}$, and

InAs QDs. The photocurrent from the QD samples below 800 nm in Figure 3.10 b-e was similar to that shown in Figure 3.10a. For each of the samples, similar results were obtained among the 2 to 3 contacts per sample that were measured. The peak photocurrent from the $InAs_{0.25}P_{0.75}$, $InAs_{0.50}P_{0.50}$, $InAs_{0.75}P_{0.25}$ and InAs QDs consecutively decreased. This variation of the photocurrent among the samples is probably due to carrier escape from the QDs becoming less probably as the depth of the QD potential increases with increasing As content.

The photocurrent below 900 nm in all of the samples can be attributed to background absorption due to the InP barriers between the QDs, similar to that measured elsewhere [115], as well as the AlInP shell surrounding the QDs, as shown in Figure 3.10a. In addition, we expect some weak background absorption below 1100 nm due to the Si substrate. The variation in background signal among the samples might be due to variation in the number of NWs actually contacted under each contact pad, which depends on the local NW density and the thickness of the embedding cyclotene (which determines how many NW tips were exposed for contacting). The total photocurrent was deconvolved into a background contribution (black dashed line), and a supposed QD absorption (red dashed line). Adding these two photocurrents gives the total photocurrent indicated by the purple dashed line, which overlays the measured data. As expected, the absorption due to the QDs red-shifted with the As composition of the QD; i.e., as the As composition of the QD consecutively increased from $InAs_{0.25}P_{0.75}$, $InAs_{0.50}P_{0.50}$, $InAs_{0.75}P_{0.25}$ and InAs, the peak of the QD absorption shifted to longer wavelengths in accordance with a decreasing bandgap energy of the QDs.

This absorption at longer wavelengths was absent in the InP NWs without any QDs. Therefore, we can clearly ascribe the excess absorption at long wavelengths as due to the QDs. These results indicate the possibility of tuning the absorption by changing the alloy composition of the QDs.

3.4 Conclusions

InP NWs with InAsP QDs were grown on Si substrates using molecular beam epitaxy with randomly positioned Au droplets acting as seed particles. PL showed that the QDs emitted in the infrared range, with the possibility of tuning the emission peaks by changing the composition of the QDs. Devices were fabricated for spectrally-resolved photocurrent measurements. The devices showed response in the infrared range at room temperature due absorption in the QDs. This work shows the potential of using an inexpensive Si substrate as the base for growing InAsP QDs within InP NWs for various optoelectronic applications, particularly wavelength-dependent photodetectors.

4. Surface Passivation of GaAs Nanowires by GaP

The subject of passivating NWs is widely studied, and is a necessary step in fabricating devices, from solar cells to single photon emitters. The previous chapter presented a passivation scheme, which employed a larger bandgap material (AlInP) to separate the charge carriers within a smaller bandgap core (InP) away from the surface states. The effectiveness of this passivation scheme was analysed using μPL, showing an improvement in PL peak intensity of the passivated NWs compared with InP NWs without a passivation shell.

The work presented in this chapter expands on the previous passivation analysis by looking at single GaAs NWs passivated by a GaP shell. Both the electrical and optical properties of the passivation shells are studied, with a NW diameter dependent model presented. This chapter contains work from "Surface passivation of tellurium-doped GaAs nanowires by GaP: effect on electrical conduction," by A. Darbandi, P. Kuyanov, et al., published in the Journal of Applied Physics Vol 115, Issue 23 (2014) p. 234305 [78]. This work was the result of a collaboration with the group of Simon Watkins at the Simon Fraser University. The author of this thesis was responsible for the μPL work presented in this chapter.

4.1 Introduction

Semiconductor NWs are potential candidates for development of optoelectronic devices including LEDs, field effect transistors, and solar cells [10,41,116,117]. Of particular interest, NW arrays are promising structures to be employed in photovoltaic devices because of their potential to achieve higher photoconversion efficiency compared to their planar counterparts [118,119]. The advantages of NWs over thin films include reduced reflectivity and enhanced light trapping due to the NWs' particular geometry [120,121]. In addition, interface misfit dislocations at heterostructure NWs can be inhibited and thus desirable bandgap engineering can be achieved [122,123]. In addition, NWs with a coaxial structure may provide efficient carrier collection as a result of decoupling the light absorption and carrier extraction length scales [124].

GaAs is the second most widely used material in the semiconductor industry after silicon [125] due to its direct bandgap and high electron mobility. However, the higher surface recombination velocity of GaAs compared to most other III-V semiconductors is a drawback. This is caused by surface states in the midgap of GaAs, which pin the surface Fermi level at midgap. As a result, a depletion region is created at the surface of the semiconductor. Surface states limit the electrical and optical properties of NWs because of a larger surface-to-volume ratio in NWs than in bulk GaAs [126]. The effect of sidewall depletion on the electrical conductivity of tellurium doped GaAs NWs was reported previously [127].

Several studies have been done to improve the electrical and optical properties of GaAs NWs by means of surface passivation. Ammonium polysulfide $(NH_4)_2S_x$ solution has been employed for sulfur passivation of GaAs thin films [128] and NWs [129]. Unfortunately, sulfur passivation does not provide long-term surface stability. Core-shell passivation of GaAs NWs with a wide bandgap semiconductor holds the promise of increased surface stability. Wide bandgap surface passivation introduces a new surface layer that moves the GaAs surface states away from the midgap by chemical bonding at the passivation interface. As a result, the Fermi level in the GaAs core becomes unpinned.

Various studies have been performed to passivate GaAs NWs with binary and ternary III-V alloys. $Al_xGa_{1-x}As$ with a bandgap between 1.6 and 1.9 eV has shown a surface recombination velocity of 2–10 x 10^3 cm s^{-1} for passivated GaAs NWs, which is an order of magnitude lower than unpassivated NWs [130]. An InGaP passivation shell has shown an improvement of GaAs NWs photoluminescence (PL) intensity of up to 3 orders of magnitude [105]. An improvement of about one order of magnitude in PL intensity was obtained for GaAs NWs cladded in $Al_xGa_{1-x}As$ [130,131]. Although many studies have been carried out to determine the effects of surface passivation on the optical properties of GaAs NWs, less information is available on the effects on electrical conduction in GaAs NWs. Recently, an improvement of about 2 orders of magnitude was observed in bulk-measured AlInP passivated GaAs NWs [103]. In this report, we present data on the radial passivation of GaAs core NWs with a GaP shell. The effectiveness of surface passivation was measured on free-standing GaAs single

NWs using the nanoprobe technique inside a scanning electron microscope [132]. Nanoprobe measurements cut down the unwanted effect of chemical residues from photolithography and contact deposition processes. Both electrical and optical characterizations are employed to assess the passivation effects in this work. Data are presented for the cases of partially relaxed and lattice-matched passivation shells on the NW sidewall depletion width.

4.2 Experimental Details

Growth of Au-assisted GaAs NWs was carried out in a vertical MOVPE reactor at a pressure of 50 Torr using H_2 as the carrier gas with a flow of 3 standard liters per minute (SLM). Prior to growth, a gold layer of 2.5 nm was coated on a (111)B Si-doped (3×10^{18} cm^{-3}) GaAs wafer using vacuum evaporation deposition. Au nanoparticles were formed subsequently by annealing the substrate at 550 ^{o}C for 1 min under H_2 and tertiarybutylarsine (TBAs) overpressure in the MOVPE reactor. This gives a NW diameter dispersion in the range of 20–700 nm. Trimethylgallium (TMGa) and TBAs were used as the group III and V precursors at flow rates of 17 and 160 µmol/s, respectively, to grow GaAs NWs at 400 ^{o}C. Te-doping was obtained by introducing H_2-diluted diethyltellurium (DETe) during the growth with a molar flow of 0.05 µmol/min. GaAs NWs were grown for 300 sec, which gives an average length of 4.2 µm. Two samples with different thicknesses of GaP shell were grown for this study. After the growth of the GaAs core, the GaP shell was then grown by switching on

the triethylgallium (TEGa) source, since TEGa promotes lateral growth [133]. The flow rates of TEGa and tertiarybutylphosphine (TBP) were set to 4.2 and 430 μmol min^{-1}, respectively (see Ref. [133] for shell growth details). A DETe flow similar to that of the GaAs core was used in the GaP shell, and the growth continued for 100 sec (type A) and 50 s (type B) at 400 ^{o}C.

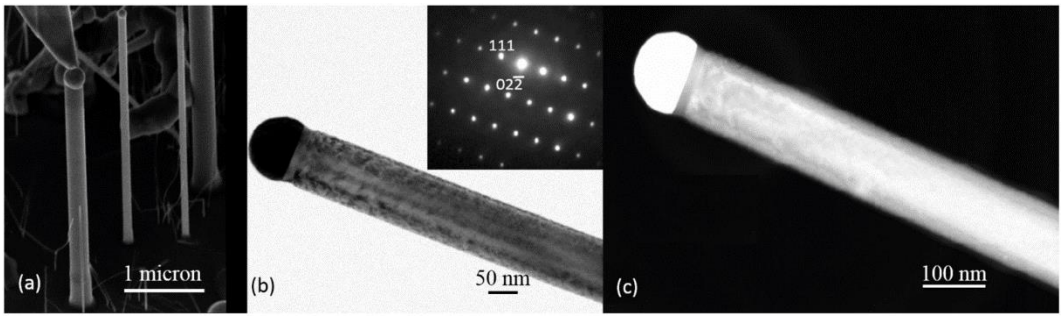

Figure 4.1: (a) SEM image of the tungsten nanoprobe contacting the tip of a free standing GaAs NW. (b) BF TEM image of type A GaAs/GaP NW with a core radius of 70 nm and shell thickness of 20 nm. The inset is the corresponding SAD pattern across the middle of the NW. (c) STEM image of type A GaAs/GaP NW. From Ref. [78]

The electrical properties of the free-standing NWs were examined by contacting the Au nanoparticle (NP) at the tip of each NW with a tungsten nanoprobe. This procedure, shown in Figure 4.1a, was carried out inside a scanning electron microscope. The optical properties of GaAs single NWs were assessed with low temperature photoluminescence measurements. NWs were transported to silicon substrates and the positions of individual NWs were located by an optical microscope. The PL excitation was provided with a HeNe laser at wavelength of 633 nm.

4.3 Results and Discussion

For a given core radius in strained core-shell NW heterostructures, there exists a critical shell thickness beyond which misfit dislocations will form. According to the calculations described in Ref. [134] in GaAs/GaP core-shell NWs, the critical shell thickness for core radius larger than 100 nm is 8 nm. Figure 4.1c shows the scanning transmission electron microscope image of a GaAs/GaP NW (type A). The vapor-solid grown GaP shell has a thickness of 20 nm. Theory shows that this leads to the formation of misfit dislocations in GaAs NWs for a core radius bigger than 15 nm. A bright field (BF) TEM image of the same GaAs/GaP NW is shown in Figure 4.1b. The observed contrast indicates the presence of edge dislocations at the core-shell interface. High resolution TEM measurements (not shown) indicate an average spacing of D_e 35 ± 5 nm. These dislocations relieve the axial strain due to lattice mismatch by a percentage given by $\frac{b}{\epsilon D_e}$, where b is the magnitude of the edge dislocation Burger's vector, equal to 0.39 nm, and ε is the GaAs/GaP lattice mismatch strain equal to 0.035. Therefore, the type A NWs were 31 ± 4% relaxed. The corresponding selected area diffraction (SAD) pattern of the middle of a GaAs/GaP core-shell NW is shown in the inset of Figure 4.1b. NWs were grown along (111) and the incident electron beam, along (110), is perpendicular to the NW growth axis. The magnitude of the axial strain relaxation, 31% x 0.035 = 0.01, is beyond the SAD detector resolution; hence, no double spots are seen in Figure 4.1b.

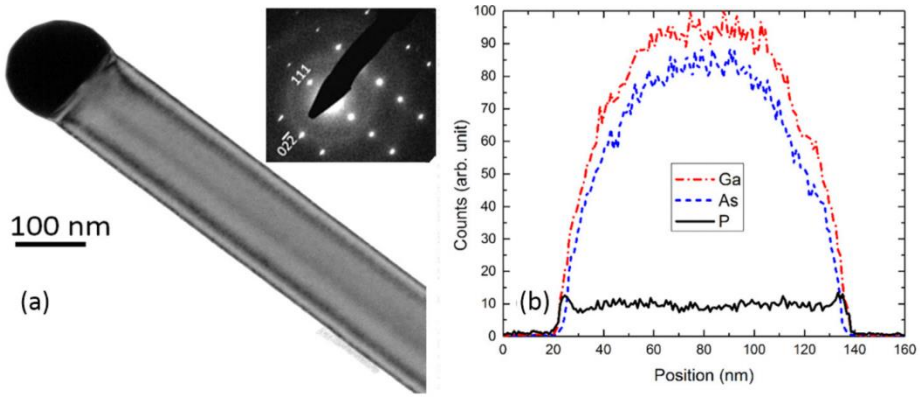

Figure 4.2: (a) BF TEM image of type B GaAs/GaP NW with a core radius of 125 nm and shell thickness of 7 nm. The inset shows the corresponding SAD pattern. (b) EDS line scan taken across the middle of type A NW. The EDS spectra are normalized to the Ga peak. From Ref. [78].

In order to provide a comparative study of the effect of misfit dislocations on the charge carrier transport, a coherent radial GaAs/GaP NW sample, type B, was grown with an estimated GaP shell thickness of 7 nm. This shell thickness corresponds to coherent GaP shell growth on the GaAs core. A BF TEM image of a representative type B NW is shown in Figure 4.2a. The image contrast is due to the NW facets, and the inset shows the corresponding SAD pattern from the middle NW. No evidence of dislocations is observed in these images. An energy dispersive X-ray spectroscopy (EDS) line scan taken across the middle of the GaAs/GaP NW of type A is shown in Figure 4.2b. The EDS spectra are normalized to the Ga peak. A phosphorus peak is evident at the NW edges indicating the GaP shell around the GaAs core NW.

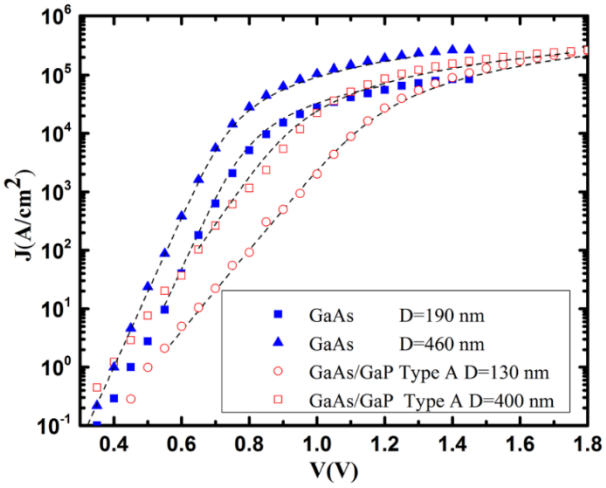

Figure 4.3: Current density vs. applied voltage for unpassivated and passivated GaAs NWs. From Ref. [78].

Representative current density vs. applied voltage (J-V) characteristics of unpassivated GaAs NWs and GaP passivated type A NWs (20 nm shell) are shown in Figure 4.3. J-V curves are illustrated for the thinnest and the thickest measured NWs for each sample. The measured current densities are normalized to the length of the corresponding NWs. The observed rectification is due to the Schottky contact at the Au-NP/NW interface. The I-V characteristics of the metal-semiconductor diode, including the NW resistance (R) is given by $I_{diode} = I_0\left(e^{\frac{q(V-IR)}{nk_BT}} - 1\right)$, where n is the diode ideality factor and I_0 is the saturation current. Least squares fits of this equation to the measured data are shown in Figure 4.3 with the dashed curves. The experimental data were recovered from fitting with less than 5% error. The ideality factor of unpassivated GaAs NWs from this fitting is around n = 1.25, while the passivated GaAs NWs show a somewhat higher ideality factor of around 1.6 as seen from the slope of the J-V

curves in Figure 4.3. This is attributed to the presence of a residual GaP axial neck, which is not completely suppressed under these shell growth conditions. The GaP neck introduces a resistance in series with the NW resistance; however, its corresponding electrical contribution is negligible due to the tellurium doping and short length of this neck segment (less than 1% of total NW length). The current densities of the GaAs/GaP NWs converged at approximately 200 kA cm^{-2} for all measured NWs with radii ranging between 60 and 250 nm. In the case of unpassivated GaAs NWs, however, the limiting current densities have a wide dispersion between 70 and 200 kA cm^{-2} for NWs with radii in the range of 75–375 nm. This is due to the depleted NWs side-walls that reduce the effective neutral cross-sectional area as discussed below.

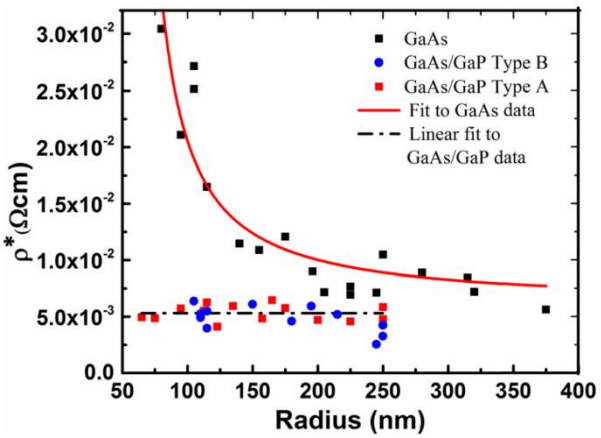

Figure 4.4: Resistivity vs. NWs radius for unpassivated and passivated GaAs NWs. Inset shows the ideality factor of GaAs and GaAs/GaP NWs. From Ref. [78].

The resistances of the NWs were extracted by fitting the measured I-V data to the diode equation. The apparent resistivity ($\rho^* = R\frac{\pi r_{NW}^2}{l}$) of the NWs was then calculated using the NWs cross-sectional area and their corresponding lengths.

Figure 4.4 shows ρ^* vs. NW radius for both unpassivated and passivated GaAs samples. Sidewall depletion has a significant impact for small diameter NWs. This can be seen from the increase of the apparent resistivity with decreasing NW diameter for unpassivated GaAs NWs. The effective radius of unpassivated GaAs NWs is then given by $r - l_d$, where l_d is the depletion width. Hence, the bulk resistivity can be written in the form [127]:

$$\rho^* = \frac{\rho}{1 - 2\left(\frac{l_d}{r}\right) + \left(\frac{l_d}{r}\right)^2}$$

Fitting the measured ρ^* of unpassivated GaAs NWs to Eq. (1) gives a bulk resistivity of $\rho = 0.00596 \pm 0.0007$ Ωcm, which corresponds to an n-type doping level of $n=3x10^{17}$ cm^{-3} assuming no compensation by acceptors. The obtained depletion width is $l_d = 46 \pm 3$ nm, which is in agreement with the calculated theoretical width of $l_d = \sqrt{\frac{2\epsilon V_s}{qn_0}} = 43 \pm 4$ nm, where ε and V_s are permittivity and surface potential of the GaAs NWs [14].

Passivation of GaAs NWs with a GaP shell results in a decrease in the surface state density in GaAs NWs and as a result the depletion region was removed and the Fermi level became unpinned. This can be observed from the consistent values of ρ^* for GaAs/GaP NWs for all diameters (see Figure 4.4). The average apparent resistivities for type A (20 nm shell thickness), and type B (7 nm shell thickness) GaAs/GaP NWs are 0.0053 ± 0.0002 Ω cm and 0.0048 ± 0.0003 Ω cm, respectively. These values approach the bulk resistivity of the unpassivated GaAs NWs. This is evidence that: (1) The depletion width l_d is negligible so that

$\rho_{NW}^{*} = \rho_{bulk}$ (see Eq. (1)), and (2) doping of the GaP shell makes negligible contribution to charge carrier transport in these structures.

Comparable apparent resistivities of type A NWs (20 nm shell thickness) and type B (7 nm shell thickness NWs) in Figure 4.4 indicate that the misfit dislocations had negligible impact on the effectiveness of surface passivation. In general, misfit dislocations act as trapping sites for electrons and holes. These trapping sites limit the charge carriers' mobilities and increase the recombination velocity. However, in the case of type A NWs (20 nm shell), the magnitude of the axial strain relaxation is 1%. This introduced a small level of edge defects so that the transport properties are not disturbed even though the corresponding GaP cap has a thickness of 2.5 times the critical thickness.

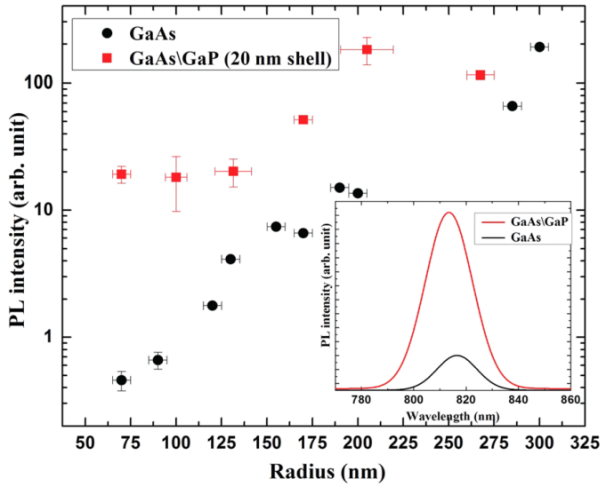

Figure 4.5: Integrated PL intensity as a function of NWs radius for unpassivated GaAs and core-shell GaAs/GaP NWs. Inset is a representative PL spectrum for a 350 nm NW before and after passivation. From Ref. [78].

The effect of passivation on the optical properties of GaAs NWs after passivation was assessed by means of low temperature μPL measurements. μPL was carried out for both unpassivated and type A passivated NWs (20 nm shell).

A representative low temperature μPL spectrum for an average size NW (350 nm) before and after GaP passivation is shown in the inset of Figure 4.5. The peak intensity of uncapped GaAs NWs observed at 816 nm corresponds to the bulk bandgap energy of 1.52 eV at 10 K. A 6 meV blueshift in PL emission was obtained upon passivation, which is attributed to the induced axial strain at the GaAs/GaP interface. Detailed μPL measurements were performed on single NWs with various diameters. Figure 4.5 shows the integrated PL intensity vs. radius of NWs for unpassivated GaAs and passivated core-shell (20 nm shell thickness) NWs. PL intensity was normalized to the length of the NWs and the background noise was subtracted. The diameter dependence of the PL intensity for uncapped GaAs NWs is due to carrier depletion at the NWs sidewalls. The calculated depletion width of l_d = 46 nm introduces a critical diameter (100 nm) below which no PL signal is detectable and the PL intensity is enhanced by increasing the NWs diameter. It is clear that the surface passivation shows a greater impact on small size NWs. This is confirmed by the experimental data for GaAs/GaP NWs shown in Figure 4.5 in which each data point is representative of an average of two measurements. The PL intensity of GaAs NWs was improved on average by a factor of 7 upon passivation with a GaP shell. The effect of surface passivation is stronger for NWs with diameters smaller than 200 nm. The PL intensity increases with GaAs/GaP NW diameter and it tends to converge to the intensity observed for uncapped NWs with diameters larger than 500 nm. A similar diameter dependence of μPL has been observed for AlGaAs capped GaAs NWs [130]. Our results agree well with the observations of PL peak enhancements by factors of 14

and 2 for lattice-matched $Al_{0.52}In_{0.48}P$ (Ref. [135]) and GaAsP [136] capped GaAs NWs, respectively.

4.4 Conclusion

Au-assisted MOVPE grown GaAs(Te) NWs were passivated using a GaP shell. The current-voltage characteristics of free-standing coherently strained GaAs/GaP NWs were measured individually. A diameter-independent apparent resistivity of 0.0048 Ω cm was obtained, which is an order of magnitude improvement in NWs conductivity compared to uncapped GaAs NWs for diameter less than 100 nm. This is evidence of Fermi level unpinning and a reduction of side-wall surface states density. Similar results with an average apparent resistivity of 0.0053 Ω cm were achieved for GaAs/GaP NWs with a passivation shell of 2.5 times the critical shell thickness. For confirmation of the GaP passivation effect, low temperature μPL measurements were carried out for both uncapped and passivated GaAs NWs. An average improvement by a factor of 7 in the integrated μPL intensity of GaAs/GaP NWs was observed.

5. Growth and Characterization of Self-Assisted NWs

This chapter expands the understanding of the growth methods of self-assisted GaP NWs on patterned Si. More specifically, the effects of varying the V/III flux ratio on the NW growth rate in both the axial and radial direction are studied. The current state of GaP NW research is introduced in Section 5.1.1. Section 5.1.2 outlines the experimental details of the study presented in this chapter. The NWs were arranged in a hexagonal pattern using an EBL patterned SiO_x layer, with periodic holes exposing the Si substrate. Each sample contained 25 100 µm x 100 µm pads, with a varying pitch of 360, 440, 520, 600, and 1000 nm, and a varying oxide hole diameter ranging from 55 to 135 nm. The focus of this study is to attempt the control of NW diameter through varying the V/III flux ratio. At a smaller group V impingement rate the Ga seed particle collected more Ga, increasing in volume, which led to a larger NW diameter. Conversely, at a larger group V impingement rate, the material within the Ga seed particle was used up more quickly than the supply of impinging Ga, reducing the volume of the particle, resulting in a smaller NW diameter. This behaviour was investigated through SEM and TEM analysis in Section 5.1.3. The pitch and diameter dependence on the morphology and dimensions of the NWs were used to further investigate the growth mechanism for this material system. This chapter contains work from “Control of GaP nanowire morphology by group V flux in gas source molecular beam epitaxy” by P. Kuyanov, J. Boulanger, and R. R. LaPierre published in the Journal of Crystal Growth, volume 462 (January 2017) p. 29 [15].

Further unpublished analysis was performed on the data presented for this study, and is summarized in Section 5.2. First the diameter along the length of each NW was measured in SEM to visualize the shape of the NWs. These data are presented for all samples, with a brief discussion on some of the findings. These data expand the understanding of the NW growth model, and will help with creating a model for the evolution of the Ga droplet under changing V/III flux ratios.

5.1 Introduction

Group III-V semiconductor NWs have many promising optoelectronic device applications, ranging from solar cells [31,137,138] to photodetectors [139–141]. Traditionally, NWs are synthesised by the VLS method using metal seed particles, most commonly Au, deposited on Si [142] or III-V [143–145] substrates. The location and size of the metal seed particles can be randomly distributed, or controlled through the use of a patterned oxide mask. Using a metal seed particle is convenient for controlling the composition and morphology of NWs, but leads to several issues, such as the incompatibility of Au with Si due to formation of deep level defects [57], and incorporation of Au into III-V NWs that degrades the carrier lifetime [58]. Self-assisted NW growth avoids foreign seed particles by using an element of the NW itself (such as Ga for growth of GaAs NWs). The use of a patterned oxide layer on the substrate allows the control of NW position and

diameter. Extensive research has been conducted on patterned self-assisted GaAs NWs [146–154], but relatively little has been done on GaP NWs.

Some of the earliest GaP NWs were synthesised using laser ablation [7,155], sublimation [8], and vapor deposition [6] resulting in very long and curved NWs. Notable work by Hiruma et al [156] and Borgström et al [157] paved the way towards VLS synthesis of III-V NWs, with Dick et al [158] and Svensson et al [159] demonstrating epitaxially grown vertically aligned GaP NWs. From here, work was done on Au-assisted GaP NWs, including the fabrication of heterostructures [160,161] and patterned arrays [162–164]. Very little work has been done on self-catalyzed GaP NWs [165,166], and even less on self-assisted selective-area growth, with only a few reports on GaAsP NWs [153]. This work demonstrates the growth of self-assisted selective-area GaP NWs on Si, and highlights the methods of controlling their morphology via V/III flux ratio.

5.1.1 Experimental Details

Self-assisted GaP NWs were grown by the VLS method in a gas source molecular beam epitaxy (GS-MBE) system. 24 nm of SiO_x was deposited using plasma-enhanced chemical vapor deposition (PE-CVD) on a Si (111) boron-doped wafer from Virginia Semiconductor with a resistivity of <0.001 Ω-cm. 120 nm thick ZEP 520A photoresist was patterned using a VISTEC EBPG 4200+ electron beam lithography (EBL) system operating at 100 kV. The pattern consisted of hexagonal arrays of holes with pitch of 360, 440, 520, 600 and 1000

nm and hole diameter ranging from 55 to 135 nm. This patterning technique was previously used for growth of InAs [167] and GaP/GaAs [80] NWs. After the photoresist was developed, the exposed SiO_x was removed by reactive ion etching (RIE). The RIE etching parameters were 320 mTorr of CF_4 gas at 100 W, an etch rate of 0.7 nm/s, and an etch duration of 65 s, ensuring that the exposed oxide was completely removed to form an array of holes. The photoresist was then stripped, and a final buffered HF (10:1 DI H_2O:10% BHF) dip was performed immediately prior to loading in the MBE chamber. The BHF etch rate was 0.37 nm/s for a duration of 20 s, ensuring that any residual native oxide was removed from the bottom of the holes, and leaving a SiO_x mask thickness of about 17 nm. Prior to the MBE growth, each sample was submitted, under ultra-high vacuum conditions, to a 15 min degas at a temperature of 300 °C in a preparation chamber. Surface cleaning was then performed in the MBE chamber using an inductively coupled hydrogen plasma source at a substrate temperature of 550 °C for 10 minutes. The GS-MBE system uses a hydride (PH_3 and AsH_3) gas cracker operating at 950 °C to supply P_2 and As_2, and an effusion cell for Ga. The growth was initiated by setting the growth temperature to 600 °C and simultaneously opening the Ga and P_2 sources at a V/III flux ratio of 2 for 7 min and 15 s, forming a GaP NW base. The V/III flux ratio was then changed to 1, 3, 4, 5 and 6 for various samples, and the growth resumed for 14 min and 30 s. The Ga impingement rate was 0.125 μm/h. Periodic $GaAs_{0.3}P_{0.7}$ marker layers were introduced to study the growth progression using transmission electron microscopy (TEM) analysis, similar to work done on Au-assisted GaAs and GaP

NWs [168]. Upon completion of the growth, the samples were cooled with P_2 for scanning electron microscopy (SEM) analysis, and also repeated without P_2 to analyze the Ga droplet at the end of the growth with transmission electron microscopy (TEM). SEM characterization was performed using a JEOL 7000F system operated at 5 kV. A JEOL 2010F high resolution scanning TEM was used to characterize individual NWs removed from the substrate by a Zeiss NVision40 focused ion beam (FIB).

5.1.2 Results and Discussion

Figure 5.1 shows a matrix of 30° tilted SEM images of all samples grown in this study with various V/III flux ratios and pitches. In this set of images, the oxide hole diameter was between 58 – 111 nm. In all cases, there was no deposition on the oxide surface between the NWs. Only a few (<2.3 μm^{-2}), small (<100 nm) GaAs crystallites were observed by SEM (not shown) on the oxide surface outside the patterned regions. These crystallites may have formed due to pinholes in the oxide that were opened during the final BHF etch. Figure 5.2 shows a 30^o tilted SEM image at higher magnification for the sample grown at a V/III flux ratio of 4, which illustrates the two classifications of NWs observed in the samples. “Type A” NWs are those which maintained their Ga droplet throughout the entire growth, as we will show through TEM analysis, resulting in very tall NWs. On the other hand, “type B” NWs lost their Ga droplet early in the

growth resulting in much shorter NWs. As a result, the type A and type B NWs resulted in a dichotomy of NW lengths, as seen in Figure 5.2.

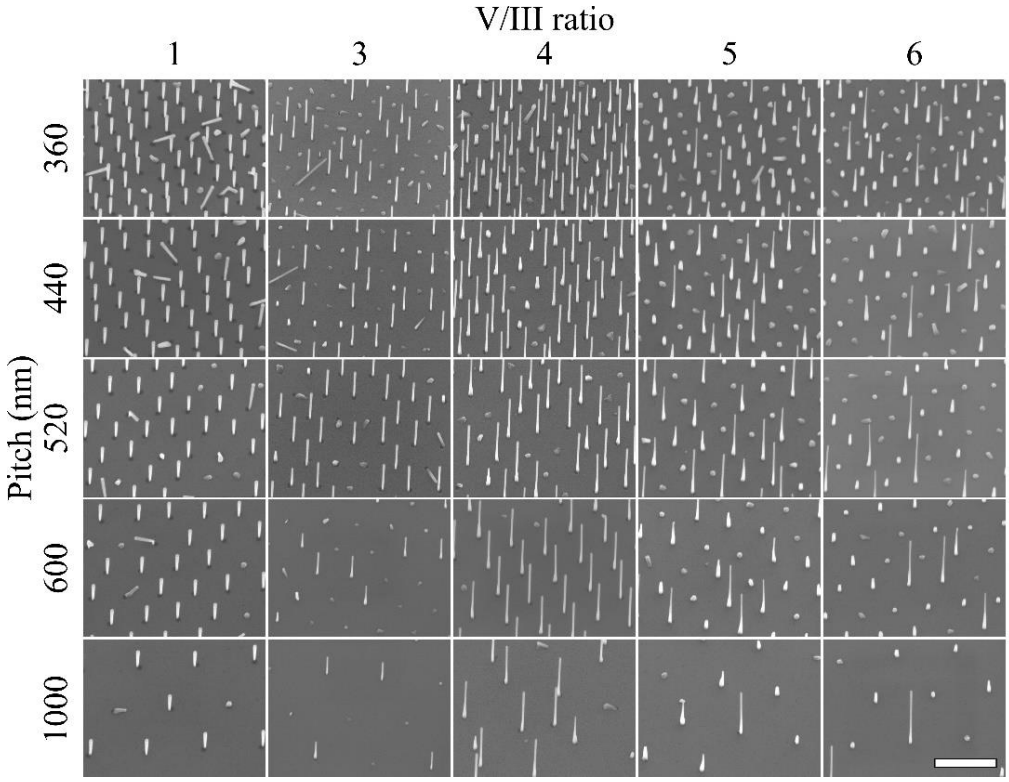

Figure 5.1: 30^{o} tilted SEM images of all samples grown in this study with various V/III flux ratios and pitches. Scale bar is 1 μm.

SEM was used to analyze the height and diameter of the type A and type B NWs in the matrix of samples displayed in Figure 5.1. The NW diameter was measured immediately below the Ga droplet for type A NWs, or at the top of the NWs if the droplet was missing as in type B NWs. The pitch and hole diameter had a minor influence on the NW height and diameter, which will be discussed in detail later. Figure 5.3 shows the NW height versus top diameter for the various V/III flux ratios and a pitch of 360 nm, averaged over all the oxide hole diameters. Solid lines indicate type A NWs, and dashed lines indicate type B NWs. 2196

NWs were measured for Figure 5.3 (over 165 NWs per V/III flux ratio), and the error bars represent the standard deviation of the measurements. The V/III flux ratio of 1 had only type A NWs present, as indicated in Figure 5.3.

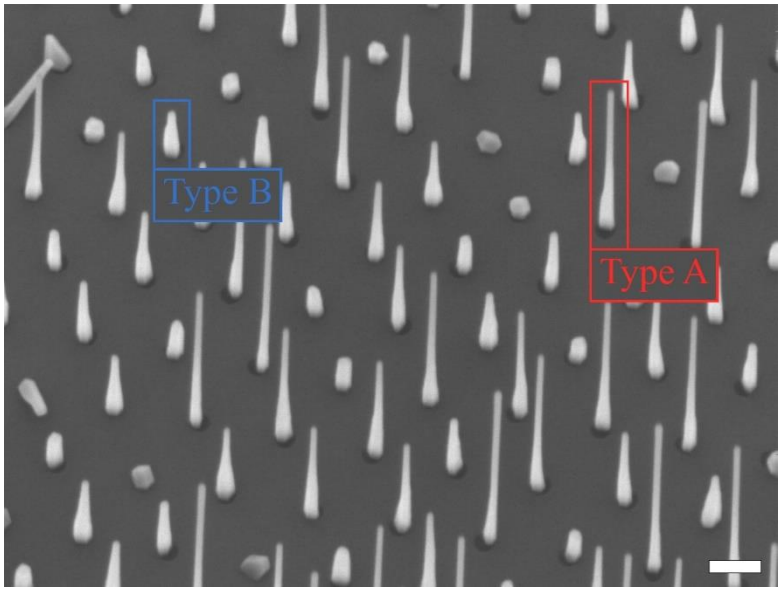

Figure 5.2: 30^o tilted SEM image with a V/III flux ratio of 4. The two types of NWs are indicated. Scale bar is 200 nm.

Remarkably, the type A NWs and type B NWs in Figure 5.3 showed a different height versus diameter trend. While the type A NWs showed an increasing height with diameter, the type B NWs showed the opposite trend. This difference in height versus diameter trend is indicative of different growth mechanisms, as will be explained later. As the V/III flux ratio increased from 1 to 6, the height of the type A NWs increased, as seen qualitatively in Figure 5.1 and quantitatively in Figure 5.3. It has been shown previously that the growth of self-assisted III-V NWs is limited by the supply of group V material [101,102] to the

Ga droplet. Therefore, the increase in NW height with increasing V/III flux ratio can be simply explained by an increase in group V supply to the Ga droplet.

The type A NWs for a V/III flux ratio of 1 showed a reverse tapered morphology. Conversely, the type A NWs for a V/III flux ratio of 3 showed negligible tapering. Finally, the type A NWs for higher V/III flux ratios showed increasingly positive tapering as shown, for example, in Figure 5.2 for a V/III flux ratio of 4. The NW top diameter is determined by the Ga droplet. Therefore, the reverse tapered morphology for a V/III flux ratio of 1 indicates an accumulation of Ga in the droplet, and therefore increasing NW diameter, with growth duration. Similar observations were made previously by Plissard et al [169] for GaAs NWs. The change in morphology from reverse tapering to positive tapering indicates consumption of the Ga droplet with increasing V/III flux ratio. This is consistent with the decrease in NW top diameter with V/III flux ratio observed in Figure 5.3 for the type A NWs.

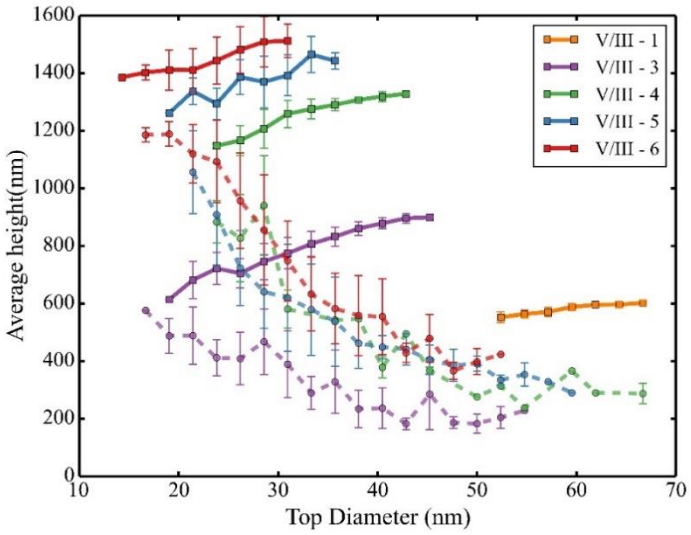

Figure 5.3: NW height versus top diameter for various V/III flux ratios, for a pitch of 360 nm and averaged over the oxide hole diameters. Lines are a guide to the eye. Solid lines indicate type A NWs with a Ga droplet, and dashed lines indicate type B NWs without a droplet.

To confirm the nature of the type A and type B NWs, TEM analysis was performed on selected NWs prepared by focused ion beam (FIB) milling. Figure 5.4 shows high angle annular dark field (HAADF) images of NWs along the [112] (Figure 5.4a-b) or [011] (Figure 5.4c-e) zone-axis for various V/III flux ratios. Selected area electron diffraction patterns, such as that shown in Figure 5.4a for the V/III flux ratio of 1 obtained along the [011] zone axis, indicated that all NWs had the zincblende crystal structure. The darker bands crossing the NWs are planar twin defects or GaAsP marker layers, as discussed later. Figure 5.4a reveals the reverse tapered morphology for the V/III flux ratio of 1, with the Ga droplet clearly visible at the top of the NW. Figure 5.4b reveals a typical type A NW for a V/III flux ratio of 3, where less tapering was observed and a smaller Ga droplet is evident at the top of the NW. Finally, Figure 5.4c shows a type A NW

for a V/III flux ratio of 4 with an even smaller Ga droplet. Figure 5.4a-c therefore shows a consecutively smaller Ga droplet with increasing V/III flux ratio, consistent with the decreasing NW top diameter observed in Figure 5.3. As the V/III flux ratio increased, the fraction of type B NWs without a Ga droplet increased. For example, Figure 5.4d-e shows two type B NWs for a V/III flux ratio of 4. The type B NWs showed a faceted tip, revealing that the Ga droplet was consumed entirely sometime during NW growth.

The interplay between NWs with and without a metal droplet on top has been studied in Ref. [170], showing that InP NWs grown by selective-area MOVPE exhibit both selective area epitaxy (SAE) and VLS growth regimes, depending on growth conditions. The NW axial growth rate is reduced with increased V/III flux ratio, which is attributed to the loss of the In droplet in a group V rich environment. We see a similar effect with increased V/III flux ratio; i.e., a greater yield of type B NWs resulted from the loss of the Ga droplet, as will be discussed later.

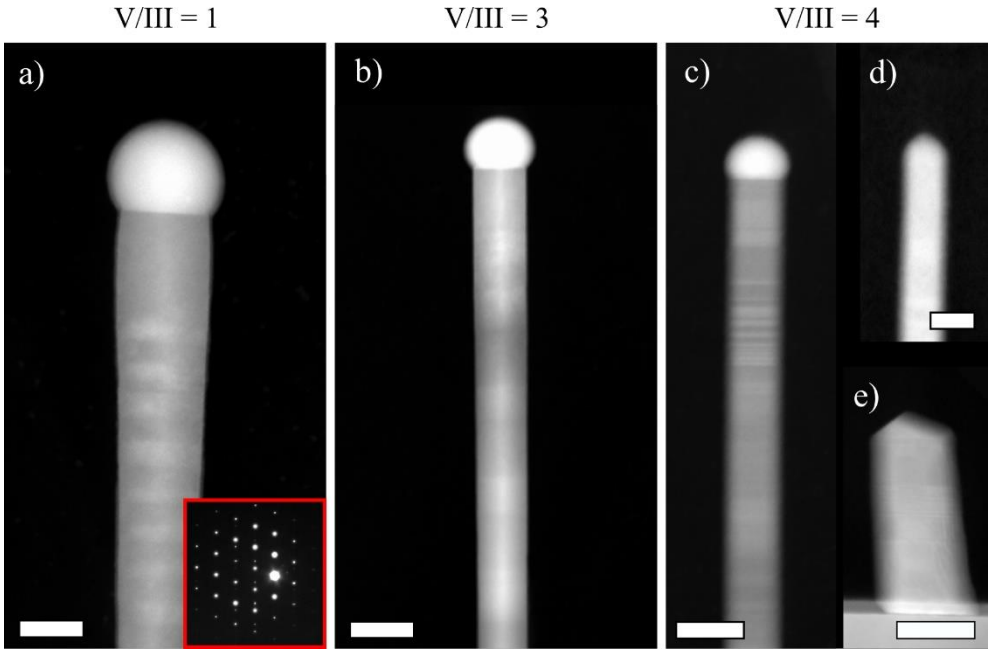

Figure 5.4: HAADF images near the top of NWs for the indicated V/III flux ratios. Scale bars are 40 nm for (a-c), 20 nm for (d), and 80 nm for (e). Inset in (a) shows the selected area electron diffraction pattern for the NW.

The length between GaAsP marker layers were measured in TEM, along the [112] zone axis, to determine the NW length versus growth time shown in Figure 5.5. The growth rate was approximately constant for a given V/III flux ratio. The base of the NWs, grown with a V/III flux ratio of 2, was implemented identically in all samples. It can be seen in Figure 5.5 that the growth rate is identical in all samples for this base segment. The V/III flux ratio was then changed to 1, 3, 4, 5 or 6 for the remainder of the growth. The average growth rate was 0.29, 0.58, 0.86, 1.18, 1.07, and 1.39 nm/s for a V/III flux ratio of 1, 2, 3, 4, 5 and 6, respectively. Thus, the growth rate is roughly proportional to the V/III flux ratio, as expected for group V limited growth.

Considering the directly impinging flux only, the expected growth rate for group V limited growth is equal to the Ga impingement rate (0.125 μm/h = 0.035 nm/s) multiplied by the V/III flux ratio. Thus, the actual growth rate of 0.24 nm/s for a V/III flux ratio of 1 is approximately a factor of 8 greater than the expected growth rate of 0.035 nm/s when considering the directly impinging flux only.

The additional flux can be attributed to desorption of group V material from the SiO_x surface surrounding the NWs [101,102]. The desorbed material may subsequently impinge on the Ga droplets contributing to axial NW growth. Previous studies [101,102] of patterned Ga-assisted GaAs NW growth on (111) Si grown by MBE showed that the axial and radial NW growth rates increased with increasing pitch. We showed that growth material is supplied by a secondary flux of both Ga and As desorbing from the oxide surface between the NWs which subsequently impinge on the liquid Ga droplet and NW sidewalls. We also showed that shading of the incident and scattered flux by neighboring NWs in the array, and competition for material between neighboring NWs, strongly affects the axial and radial NW growth rates. Krogstrup et. al. [150] estimated the diffusion length for Ga and As adatoms on thermal oxide at T = 630 °C, showing that the diffusion lengths are negligible. Due to the large vapor pressure of P under our growth conditions, its diffusion length on oxide or the NW sidewalls is also expected to be negligible. Therefore, the re-emission of Ga and P from the oxide surface both contribute to the NW growth, and is consistent with the lack of growth on the oxide surface between the NWs. However, the large reservoir of Ga in the droplet means that axial NW growth is group V limited. Thus, our

observed boost in the axial NW growth rate with V/III flux ratio is attributed to the desorption of P from the oxide surface followed by impingement on the Ga droplet.

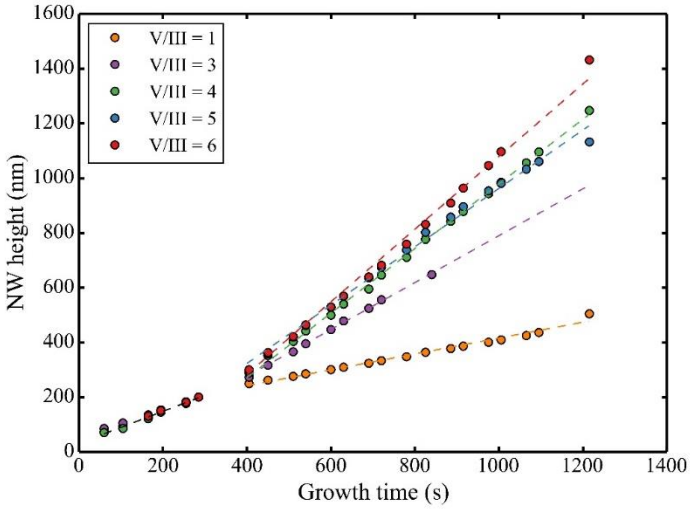

Figure 5.5: NW length versus growth time for a pitch of 360 nm and hole diameters between 97-136 nm. Dashed lines represent the lines of best fit for different V/III flux ratios.

The average axial growth rate of type A NWs was calculated from the total NW height, as measured by SEM, divided by the total growth time, as shown in Figure 5.6a, as a function of pattern pitch and V/III flux ratio. As discussed previously, the axial growth rate increased with V/III flux ratio, as expected for group V limited growth. The average axial growth rate had no significant dependence on pitch for a V/III flux ratio of 1 and 3, but a slightly positive dependence for larger V/III flux ratios. As mentioned earlier, this dependence of axial NW growth rate with pitch was previously attributed to shadowing and competition among neighboring NWs for group V flux re-emitted from the oxide

surface [101,102]. These effects increase with decreasing pitch, meaning a lower axial growth rate at small pitches, as observed. These effects are also more significant for larger V/III flux ratios where the NW height is greater (see, for example, Fig. 4d of Ref. [102]).

The average growth rate of the NW top diameter for the type A NWs is shown in Figure 5.6b, as a function of pattern pitch and V/III flux ratio. Unlike the axial growth rate, the radial growth rate decreased with V/III flux ratio. As discussed previously, this is attributed to the decrease in volume of the Ga droplet with increasing V/III flux ratio. On the other hand, the radial growth rate increased with pattern pitch. The radial growth of the NWs occurred by vapor-solid deposition of GaP on the NW sidewalls. This radial growth of the NWs is group III limited (as in conventional thin film deposition by MBE) and is fed by the direct deposition of Ga on the NW sidewalls as well as the re-emission flux of Ga from the oxide surface. As the pitch increases, there is a larger surface area surrounding each NW and decreased competition and shadowing among neighboring NWs for the desorbed Ga flux, resulting in a higher radial growth rate, as observed [102]. The rate of consumption of the Ga droplet was also reduced with increasing pattern pitch due to the larger collection of Ga from the oxide surface surrounding each NW.

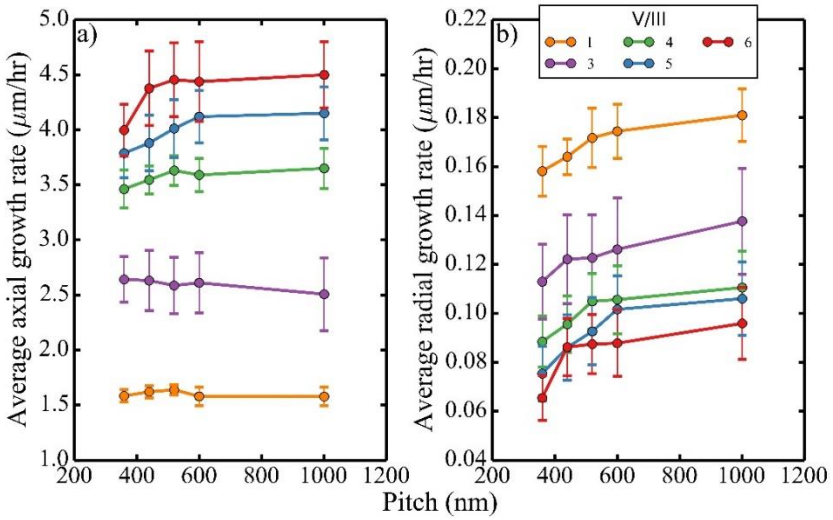

Figure 5.6: (a) Average axial and (b) average radial growth rate versus pitch of type A NWs for different V/III flux ratios. The hole diameter was between 56 - 136 nm for both (a) and (b). The error bars represent the standard deviation. Lines are a guide to the eye.

Next, we examined the dependence of growth on the oxide hole diameter, which was intentionally varied from 56 – 136 nm, as determined by SEM measurements. Figure 5.7a shows the yield of type A NWs (# type A NWs / # all NWs) versus the oxide hole diameter for various V/III flux ratios, averaged over all pitches. It is observed that the oxide hole diameter had a significant effect on the yield of type A versus B NWs. The larger oxide opening increases the area over which Ga adatoms are collected from the exposed Si surface. We therefore expect a larger droplet with increasing hole diameter, as demonstrated in Figure 5.7b. This larger droplet is less likely to be consumed over the growth duration, leading to a larger yield of type A NWs. This dependence of NW yield on hole diameter might be mitigated by a Ga pre-deposition step to completely pre-fill the hole prior to NW growth, which is the subject of future studies.

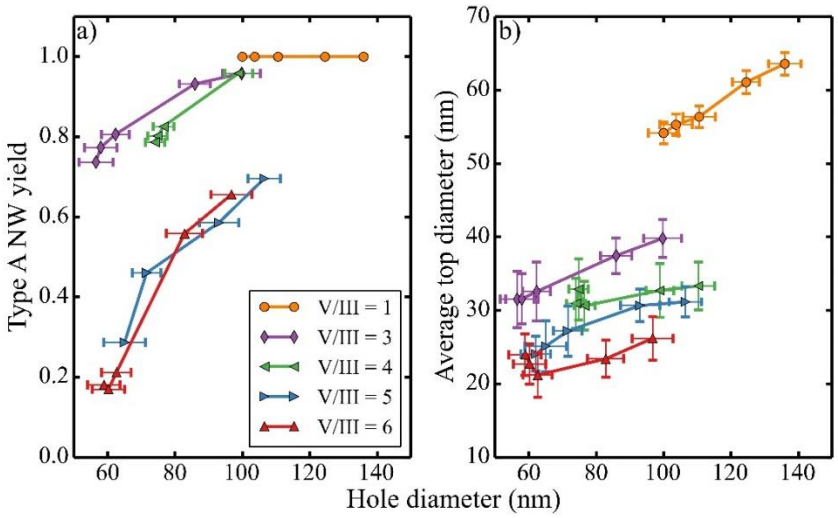

Figure 5.7: (a) Yield of type A NWs (# type A NWs / # all NWs) versus oxide hole diameter averaged over all pitches. (b) Average top diameter versus oxide hole diameter for type A NWs with a pitch of 360 nm. Lines are a guide to the eye.

The type A NWs were characterized by the presence of a Ga droplet at the top of the NWs, while the type B NWs were those NWs where the Ga droplet was consumed partway through growth. In addition, the type A NWs showed an increasing height with diameter (Figure 5.3), while type B NWs showed the opposite trend. This difference can be attributed to a change in growth mechanism of the NWs. For type A NWs with a Ga droplet, axial growth is dependent on the group V flux, either directly impinging on the droplet or desorbing from the oxide surface. In this case, the axial growth rate is dependent on the droplet volume, such that larger droplets will intercept more group V material desorbing from the oxide surface (i.e., the ratio of droplet surface area to NW top facet area increases). Once the Ga droplet is consumed, as in type B NWs, an inverse dependence of NW height with diameter is observed, signifying a change in growth conditions. The inverse diameter-height relation is a well-known signature

for growth that is limited by Ga collection and diffusion on the NW sidewalls [171].

5.1.3 NW Shape Analysis

The SEM data discussed earlier contained a wealth of information which was not analyzed in the published work presented above. The shape of the NWs was briefly discussed, but not fully explored. From the SEM images similar to those presented in Figure 5.1, the NW diameter was measured at very fine steps along the NW length. In order to visualize the data, the spot along the NW where each diameter was measured is plotted, with the colour bar representing the diameter in nm. The NWs for each pitch were sorted from shortest to tallest, with an example of the sample with pitch of 360 nm grown at a V/III flux ratio of 3 shown in Figure 5.8.

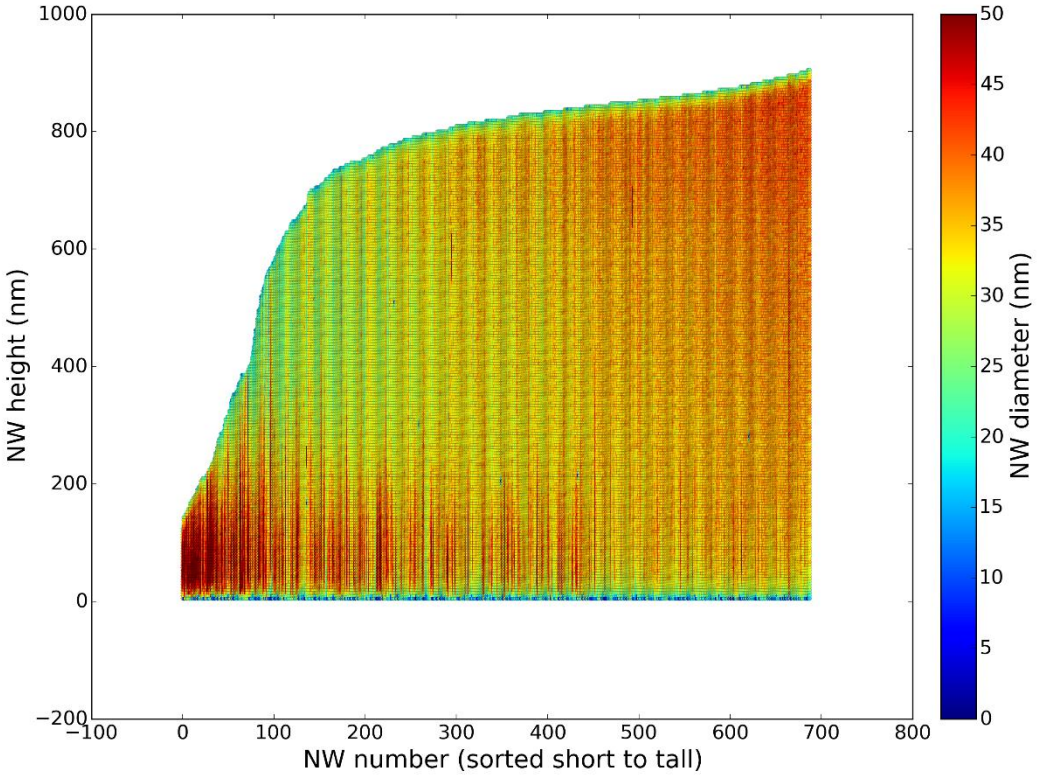

Figure 5.8: NW height with diameter measurements along the length, sorted from short to tall.

The first observation can be made by examining the NW diameter along the bottom of the NWs (100 nm above the base). The first 100 NWs have a large diameter of up to 50 nm, and are classified as type B NWs. For these NWs the Ga droplet was consumed early during the growth, resulting in both axial and radial growth. The taller NWs have a base diameter which is gradually decreasing, reaching a minimum for the tallest NWs, which are classified as Type A NWs. The transition between Type A and Type B NWs is gradual, which indicates that the consumption of the Ga droplet during growth happens randomly, influenced by localized growth conditions for each NW.

The measured diameter along the length of representative type A NWs for each sample (V/III flux ratios of 1, 3, 4, 5, and 6) are presented in Figure 5.9. NWs from samples with a V/III flux ratio of 1 and 3 show a reverse tapered shape, which is attributed to the low supply of P_2, leading to an increase in the Ga droplet volume throughout the growth time. The rest of the samples show a tapered morphology partway through the growth, until the NW diameter stabilizes. The rest of the data can be found in the Appendix.

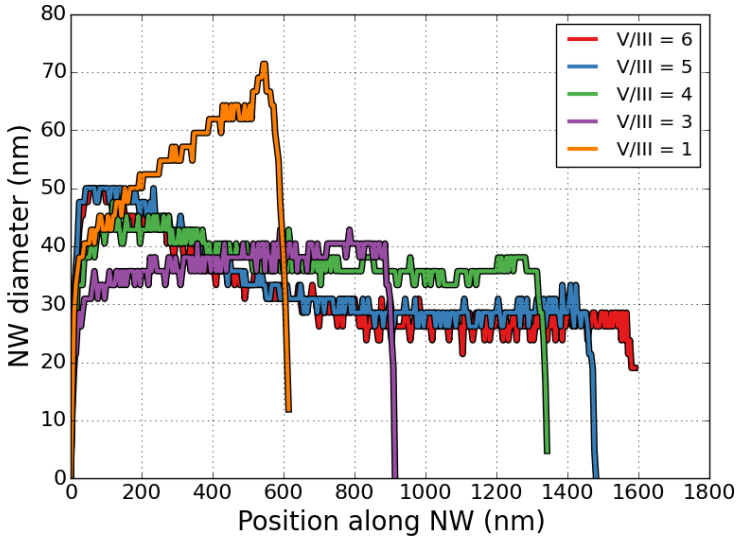

Figure 5.9: Diameter along length of NW for various V/III flux ratios.

5.1.4 Conclusion on GaP NWs

The growth of self-assisted selective-area GaP NWs using a gas source MBE system was investigated by the effect of V/III flux ratio on the consumption of the Ga droplet. By increasing the V/III flux ratio it is possible to reduce the Ga droplet volume, resulting in reduced diameter of the NWs. We further

investigated the effects of the oxide hole diameter, which influenced both the diameter of the NWs as well as the likelihood of the transition from type A to type B growth. By carefully controlling the preparation of the patterned oxide layer and selecting an appropriate V/III flux ratio, it is possible to control the diameter of the NWs.

5.2 Patterned Growth of InP NWs on Si

This section outlines the progress made in self-assisted InP NW growth on a patterned Si substrate. The Si substrate preparation used the same procedure as that for the GaP growths summarized earlier in this chapter. First, the effects of growth temperature and V/III flux ratio on the yield of NWs were investigated. The parameter space and results are summarized in Figure 5.10.

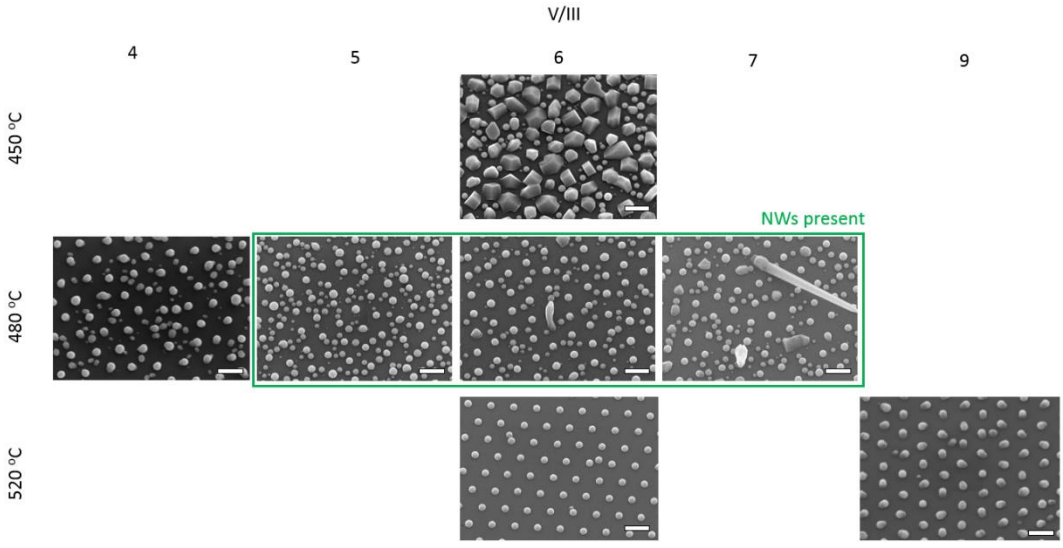

Figure 5.10: SEM images within the parameter space for temperature and V/III flux ratio of self-assisted InP NWs. The green box highlights the growth conditions which yielded NWs. Scale bars are 400 nm.

The temperature was varied from 450 ^{o}C to 520 ^{o}C at a V/III flux ratio of 6. At a lower temperature a large number of crystallites were formed, with droplets present on the oxide between the holes. This is attributed to the reduced desorption of group V material at a lower temperature, resulting in a larger concentration of P from the impinging P_2 flux. With enough P available, InP crystallites were formed. In this case, the crystallites formed facets that match some of the preferred NW growth directions for the (111) direction on Si, which is highlighted in Figure 5.11.

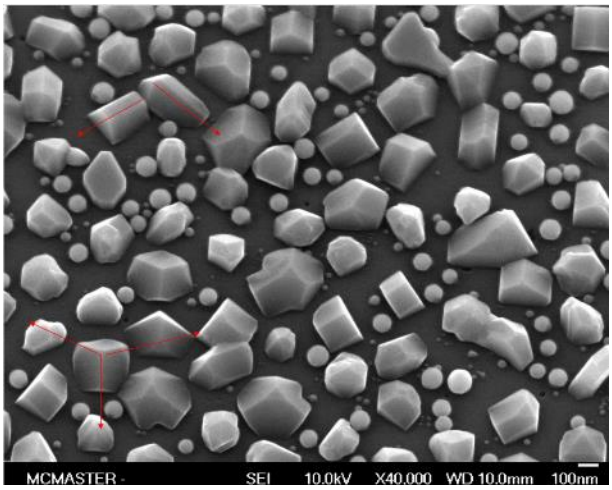

Figure 5.11: InP patterned growth at 450 ^{o}C with a V/III flux ratio of 6. Facet directions are highlighted, matching the preferred directions for epitaxial growth on a (111) Si substrate.

As the temperature was increased to 480 ^{o}C the number of crystallites was reduced, resulting in the formation of In droplets. The density of smaller droplets on the surrounding oxide was also reduced. As the temperature was increased further to 520 ^{o}C, virtually all crystallites and NWs disappeared leaving only In droplets present. The oxide was also free of any In droplets. Conversely to the

argument for low temperature growth, at a higher temperature the P desorption rate is increased, forming less InP crystals. Once the rate of desorption surpasses the rate of impingement, the growth of crystallites stops, leaving In droplets on the surface. Growth at this temperature has been repeated at different V/III flux ratios, summarized in Figure 5.12.

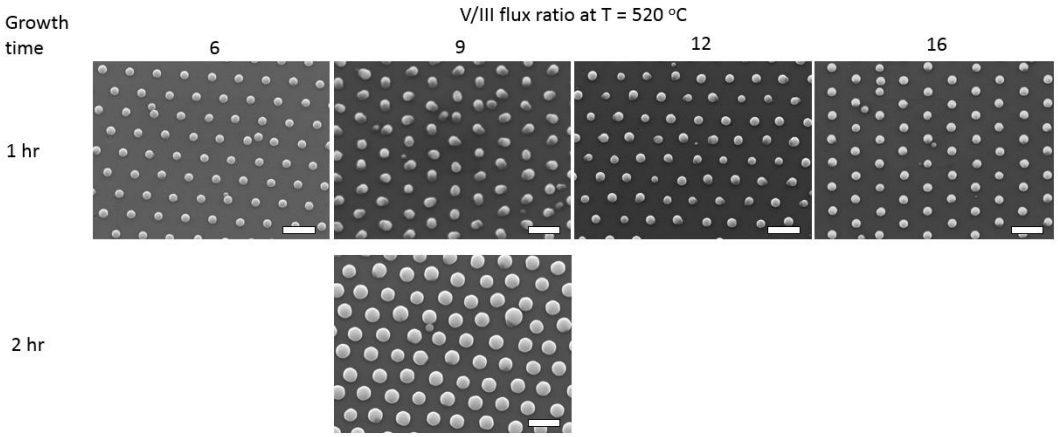

Figure 5.12: InP growth at T = 520 °C, at various V/III flux ratios. Scale bars are 400 nm.

At an increased V/III flux ratio an increase of crystallite or NW formation was expected. However, only In droplets were present for all V/III flux ratios. At a higher temperature, it is expected that the group V desorption is increased, which suggests that the desorption rate was much greater than the maximum impingement rate available from the MBE system used.

Figure 5.10 shows the presence of NWs at a temperature of 480 °C, as highlighted by the green box. Figure 5.13 shows detailed SEM images at a 30° tilt for the growth conditions which resulted in NWs. The inset in each plot shows an InP NW observed for each sample. The plots below each SEM image show the

dependence of NW yield on oxide hole opening. The NW yield was extremely low.

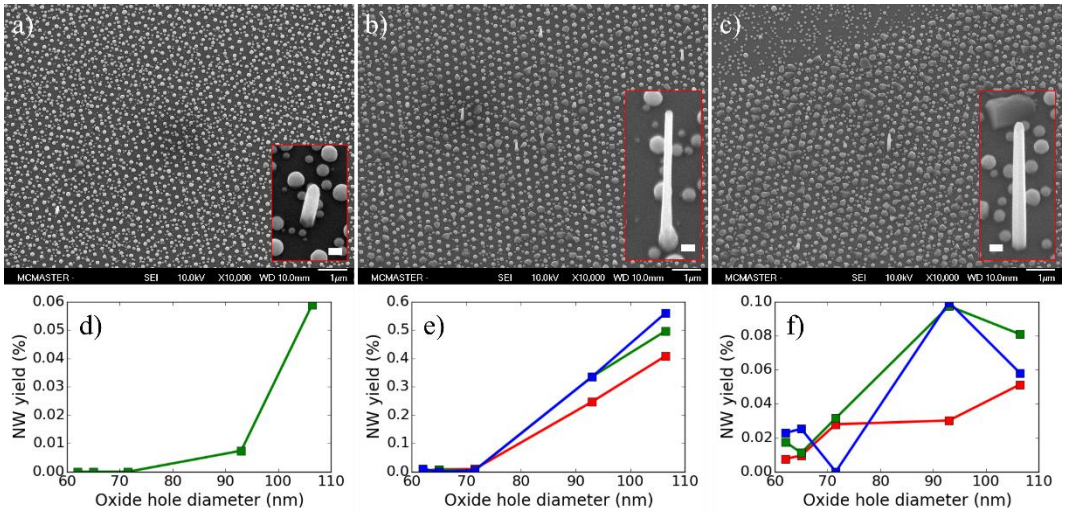

Figure 5.13: 30^o tilted SEM images of NWs grown at T=480 ^{o}C and V/III flux ratios of (a) 5, (b) 6, and (c) 7. The insets in each SEM image shows an example of the types of NWs obtained for each sample, with the scale bars representing 100 nm. (d), (e), and (f) show the measured NW yield as a function of oxide hole opening for samples grown at a V/III flux ratio of (d) 5, (e) 6, and (f) 7.

The highest NW yield was found at a growth temperature of 480 ^{o}C and a V/III flux ratio of 6. The measured NW yield shows a dependence on oxide hole diameter, with the highest yield obtained for the largest hole diameters for all samples. The oxide hole opening diameter influences the shape and volume of the seed particle, which has an influence on the formation of NWs. To further study the cause of the low NW yield, a cross-sectional TEM sample was prepared using FIB milling techniques for the sample grown at a V/III flux ratio of 6. Figure 5.14 presents a cross-sectional TEM image of an In droplet, showing a significant amount of InP material below the surface of the Si substrate. This could be a result of either In etching the Si throughout the NW growth, or over-etching

during the RIE preparation step. Optimal NW growth depends on many factors, including the shape and contact angle of the seed particle with the substrate. The exact cause of the “bowl” shape at the InP/Si interface is not known, but it hints at unpredictable growth conditions for the shape of the In droplet at the start of NW growth. It is the hope of the author that through the work presented in this section, the next steps for troubleshooting this material system can be undertaken.

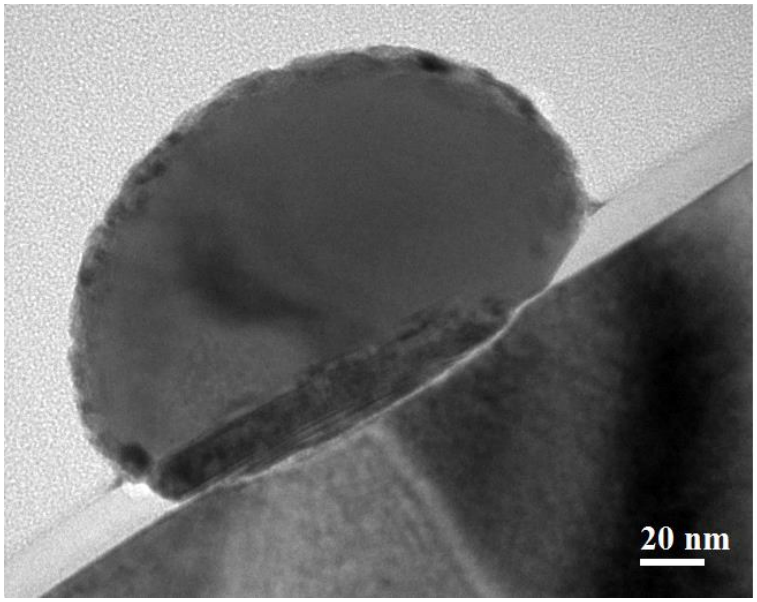

Figure 5.14: Cross-sectional TEM of In droplet showing an abnormal Si-InP interface.

6. GaAs QDs Embedded within Self-Assisted GaP NWs

Having studied the growth mechanisms of self-assisted GaP NWs on a patterned SiO_x surface, discussed in Chapter 5, attention is now turned to a QD-based device within the GaAs/GaP material system. In this work, a passivated GaP p-n junction was fabricated with and without 15 GaAs QDs within the intrinsic region. The various aspects of fabricating a NW-based p-n junction are discussed in detail, such as the passivation and contacting scheme, highlighting some of the difficulties this method presents. The NWs were studied with both SEM and TEM to reveal their structure and to help explain some of the optical and electrical results. The photocurrent as a function of illumination wavelength was measured, showing absorption within the GaAs QDs beyond the bandgap of GaP.

6.1 Introduction

GaP in the bulk form is a ZB semiconductor with a room temperature bandgap of 2.26 eV. GaP NWs can be grown using the VLS technique with either the ZB or WZ crystal structure [162], with applications in LEDs [162], electrolysis [172], and betavoltaics [173]. An attractive feature of large bandgap semiconductors is the improved performance at higher temperatures, such as a low reverse bias leakage current in a GaP p-n junction [174]. The NW architecture provides unique advantages not possible with thin film counterparts, such as growing lattice

mismatched semiconductor materials through strain relaxation in both core-shell and axial structures on inexpensive Si substrates [142,175], taking advantage of unique waveguiding effects within periodic arrays of NWs [176], and the growth of uniform QDs such as InP/InAs and GaAsP/GaAs [177] for single photon sources and detectors [178], among other applications.

Periodic arrays of NWs with a uniform diameter distribution provide a technique for growing uniform, lattice-mismatched III-V QDs, which is difficult to achieve using conventional techniques, such as solution-based techniques [89] and the SK method [66]. In addition to single photon sources and detectors, which have applications in quantum information processing, a QD-based photodetector offers several advantages over a traditional bulk absorption technique, such as lower thermal electron generation [179] and normal angle incidence. The GaAs QD, confined by a GaP barrier, provides several interband energy transitions which fall within the visible and near-infrared ranges.

We present self-assisted GaP NW arrays on a Si substrate which contain a p-n junction. In addition, we have added 15 GaAs QDs within the intrinsic region of the device. Our motivation is to characterize the behaviour of the QDs within a NW-based p-n junction to realize some of the applications presented above. To our knowledge, a NW-based GaP p-n junction has not been demonstrated prior to this work. Current-voltage (IV) and wavelength-dependent photocurrent characterization of our device demonstrate diode behaviour with absorption within the GaAs QDs, located below the bandgap of GaP.

6.2 Experimental Details

Self-assisted GaP NWs were grown on a Si (111) boron-doped substrate from Virginia Semiconductor with a resistivity of <0.001 Ω-cm. The NWs were grown using the VLS method in a gas source molecular beam epitaxy (GS-MBE) system. A pattern of holes was defined by electron beam lithography in 30 nm of SiO_x deposited by plasma-assisted chemical vapor deposition. The pattern consisted of a hexagonal arrays of holes with a pitch of 600 nm and hole diameter of 68 ± 6 nm, separated into pads of 100 μm by 100 μm area. NWs nucleated in the holes according to the self-assisted VLS growth process. The EBL patterning procedure and initial GaP NW growth is described in our previous work [15], and is used here as building blocks for a p-n junction NW device. After the EBL pattern was developed and etched (see Ref. [15] for details), the sample was dipped for 25 s in a buffered HF (10:1 DI H_2O:10%BHF) solution immediately prior to loading in the MBE chamber. Prior to MBE growth, the samples were degassed for 15 min at 300 ^oC in a preparation chamber. Surface cleaning was then performed in the MBE chamber using an inductively coupled hydrogen plasma source at a substrate temperature of 550 °C for 10 minutes. Two samples were prepared: sample A, which contained 15 GaAs quantum dots (QDs) in the middle of the intrinsic region of the p-n structure, and sample B, which did not contain QDs. The growth of both samples was initiated by setting the substrate temperature to 600 ^oC and simultaneously opening the Ga, Be and P_2 sources at a V/III flux ratio of 2 and a Ga impingement rate corresponding to an equivalent thin film growth rate of 0.125 μm/hr for 14 min, forming a p-type GaP NW base. The Be flux was

set to provide a thin film equivalent doping concentration of $5x10^{18}$ cm^{-3} as determined by Hall effect measurements. After the p-type region, an intrinsic (undoped) region was grown by terminating the Be flux, and continuing GaP growth for 24.5 min. The p-n junction was then completed by adding a Te flux and continuing growth for 3.5 min. The Te flux was set to provide a thin film equivalent doping concentration of $1x10^{19}$ cm^{-3}. The Ga droplet on top of the NW was consumed by keeping the substrate at 600 ^{o}C and reducing the P_2 flux by a factor of 3 without Ga flux for 20 min. The sample was passivated with AlP by reducing the growth temperature to 420 ^{o}C, increasing the equivalent thin film growth rate to 0.25 µm/hr, increasing the V/III flux ratio to 5, and continuing growth for 30 min. The droplet consumption step and lower growth temperature resulted in both radial and axial growth of AlP. AlP reacts with H_2O and is unstable in atmosphere, requiring a capping layer. In this work, an intrinsic GaP shell was grown at an equivalent thin film growth rate of 1 µm/hr and a V/III flux ratio of 2 for 20 min. Two samples were prepared: Sample A with 15 GaAs QDs in the intrinsic region and Sample B without QDs. The GaAs QDs were placed in the middle of the intrinsic region by replacing the P_2 flux with As_2 flux after 12 mins of intrinsic GaP growth, while keeping the Ga flux constant. Each GaAs QD was grown for 15 s at 600 ^{o}C and a V/III flux ratio of 2. The As_2 flux was then replaced with P_2 flux to grow the GaP barrier for 40 s. A total of 15 GaAs QDs and GaP barriers were added, followed by 13 min of intrinsic GaP growth. The schematic of the p-n junction devices (sample A and B) are shown in the insets of Figure 6.5.

Following NW growth, characterization by scanning electron microscopy (SEM) was performed using a JEOL 7000F operating at 5 kV. Scanning transmission electron microscopy (STEM) analysis was performed using HAADF imaging on a JEOL 2010F operating at 200 kV.

The NW array was planarized by spin-coating BCB [70]. The top of the NWs were then exposed for electrical contacting by reactive ion etching (RIE). The RIE etch was performed with a 1:1 O_2:CF_4 ratio at an operating pressure of 180 mTorr. The etch time was 5 min at 50 W, which resulted in 145 ± 21 nm of NW tips exposed above the planar surface.

A 10 min 1:1 H_3PO_4:DI H_2O wet chemical etch was used to remove the GaP capping layer and AlP passivation layer at the exposed top of the NWs. 250 nm of ITO was sputtered on top of the NWs, followed by a Ni/Ge/Au (25/50/225 nm) contact on the edge of the ITO for probe contacting. 250 nm of Al was sputtered on the rear of the Si substrate. The contacts were annealed at 400 ^{o}C for 1 min.

After the devices were fabricated, current density-voltage (J-V) characterization was performed using a Keithley 2400 source meter in a two-point probe configuration. The samples were illuminated using a broadband lamp (Newport 96000). Responsivity measurements were performed using a Newport 6333 100 W quartz tungsten halogen lamp dispersed by a Horiba Jobin Yvon iHR550 f/6.4 spectrometer, calibrated by a Newport power meter.

6.3 Results and Discussion

Figure 6.1 shows a representative 30^{o} tilted SEM image of the as-grown p-n junction with GaAs QDs (sample A) on a NW pad with a pitch of 600 nm. The average NW height was measured to be 1545 ± 68 nm, with a reverse tapered shape, having average top and bottom diameters of 266 ± 13 nm and 182 ± 12 nm, respectively (measured over 50 NWs). The NW surface appears rough, which will be discussed using TEM analysis in the next section. Unlike with our previous work with GaP growth at 600 ^{o}C [15], which showed a clean oxide surface between NWs, thin film growth between the NWs was observed in the present samples due to the low temperature growth of AlP and GaP shells on the NWs.

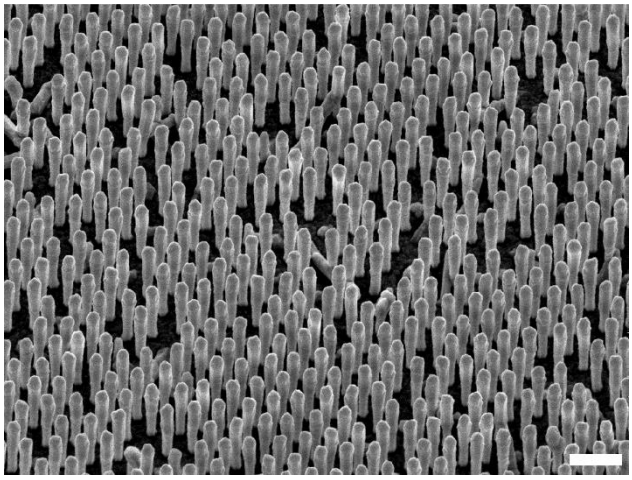

Figure 6.1: 30^{o} tilted SEM image of as-grown p-n junction devices with pitch of 600 nm and 15 GaAs QDs (sample A). Scale bar is 1 μm.

Figure 6.2a and b show HAADF STEM images of single NWs along the [011] zone axis of sample A (with QDs) and sample B (without QDs), respectively. The NW core of sample A had a uniform average diameter of 57 ± 5 nm, with a 12.0 ±

0.9 nm AlP shell (measured from 3 NWs). The NW core of sample B had a uniform average diameter of 48 ± 4 nm, with a 10.0 ± 0.6 nm AlP shell (measured from 2 NWs). The inset in Figure 6.2a contains the selective area diffraction pattern acquired in the middle of the NW, showing a ZB crystal structure with twin defects. The dark field contrast from the GaAs QDs and the AlP shell is confirmed by EDX in Figure 6.2c, showing an area map of As, P, and Al (Ga counts were excluded for clarity of image). For the NW shown, the average GaAs QD axial height is 13.3 ± 2.0 nm and the average GaP barrier height is 15.2 ± 1.4 nm. Figure 6.2d shows a high resolution TEM image of the NW from Figure 6.2c, with the growth direction indicated by the arrow. The crystal structure is ZB with stacking faults present, as shown in the inset of Figure 6.2b. Figure 6.2e shows a GaP NW from our previous work [15]. The Ga droplet was consumed using the same technique as used in this study, which resulted in a flat top. The same flat top for the NW core can be seen in Figure 6.2b, indicated by the arrow. During the droplet consumption, several stacking faults form followed by a transition to the WZ phase, which has been reported previously [180].

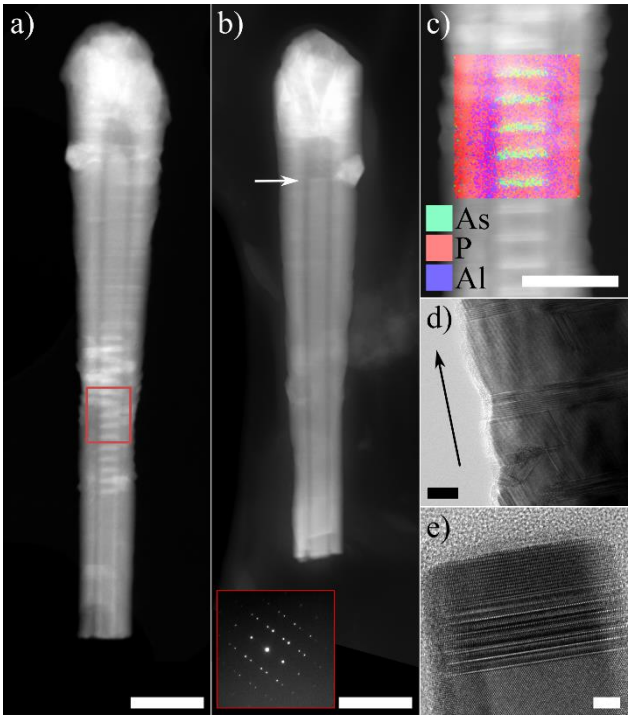

Figure 6.2: HAADF STEM images of (a) sample A with 15 GaAs QDs, and (b) sample B without 15 GaAs QDs along the [011] zone-axis. Inset shows a SAD ZB diffraction pattern from the middle of the NW. (c) EDX area scan of GaAs QD region, showing the presence of the AlP shell and the GaAs QDs. (d) High resolution TEM image of GaP NW after droplet consumption. (e) High resolution TEM image of GaP NW after Ga droplet consumption.

Dark and broadband illuminated measurements were performed for samples A and B. J-V curves for each sample are presented in Figure 6.3a and b for samples A (with QDs) and B (without QDs), respectively.

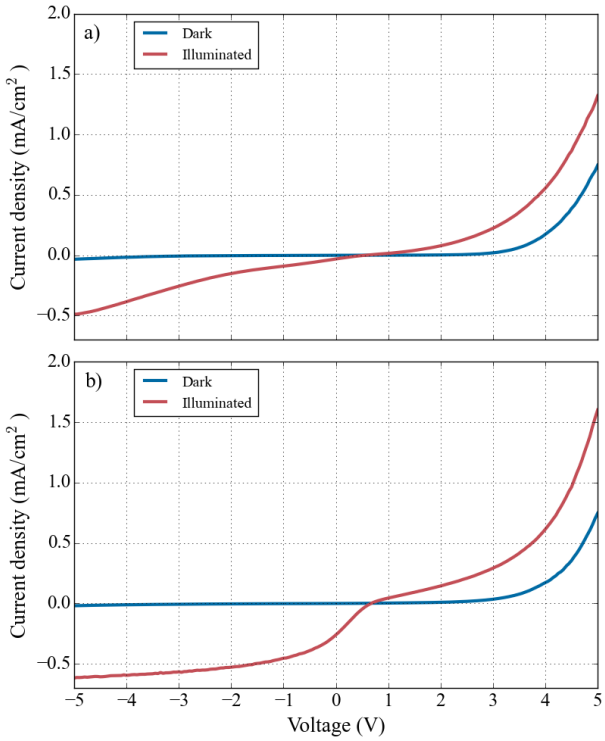

Figure 6.3: J-V plots for AlP passivated p-n junction with (a) and without (b) GaAs QDs.

The device fabrication steps relied on a 10 min 1:1 H_3PO_4:DI H_2O wet chemical etch to remove the GaP capping layer. The H_3PO_4 etch is anisotropic, etching both the exposed GaP tips, as well as the sidewalls of the NW, once it is able to penetrate along the NW edges through the BCB layer. Beyond a 10 min etch, the sample appeared to be damaged, with over-etching appearing beyond the patterned section containing the NWs. To prevent damage to the AlP passivation shell caused by over-etching, the etch time was limited to 10 min. After etching, the ITO contact layer is then deposited on the partially etched capping layers.

SEM was used to investigate the results of the etching steps (not shown here), revealing that the exposed NW tip average height was reduced by 48 nm and the

average diameter was reduced by 12 nm. This finding leads to the fact that the AlP passivation shell and GaP capping layer are not likely completely removed by the etching process. Therefore, the n-type core section of the NW is contacted through the AlP passivation shell and GaP capping layer. This issue will limit the performance of the device, because the GaP capping layer is defective, as shown in Figure 6.2d, and may provide an electrical shorting path between the top contact and the Si substrate. On the other hand, the remaining AlP and GaP may act as an electrical barrier between the ITO contact and the n-type GaP region.

Dark J-V measurements show rectification for both devices, with a large turn-on voltage. Under a reverse bias of -4V the current was measured to be 1.7 nA and 1.1 nA for sample A and B, respectively. Both samples demonstrated good rectification. Under illumination both samples show a short-circuit current, which indicates that there is a built-in electric field separating optically generated electron-hole pairs (EHPs).

Wavelength-dependent photocurrent was measured for both samples, with the absolute responsivity determined using a wavelength calibrated power meter (this setup is described in detail in Section 2.6.2). The responsivity with QDs (solid line) and without QDs (dashed line) is shown in Figure 6.4 at a reverse bias of -4V. The sample without QDs shows absorption up to approximately 550 nm, which is consistent with the room temperature indirect bandgap of GaP (548 nm).

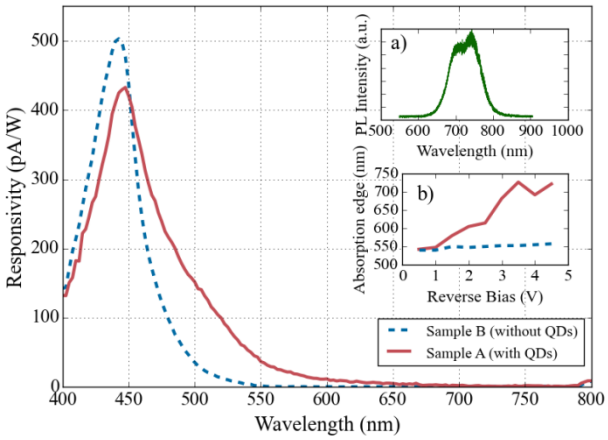

Figure 6.4: Photocurrent vs. wavelength for two p-n junctions with QDs (solid line) and without QDs (dashed line) at a bias of -4V. Inset a) contains a room temperature photoluminescence spectrum from Sample A (with GaAs QDs), showing PL emission corresponding to the QDs.

The sample with GaAs QDs shows a broad response beyond 550 nm which we attribute to absorption within the QDs. Once EHPs are generated within the QD energy levels, they can be extracted into the GaP intrinsic material under an electric field through either thermal excitation or tunneling processes, and collected.

Inset (a) in Figure 6.4 shows the room temperature photoluminescence spectrum of the device with GaAs QDs, showing a broad emission with two peaks at 707 nm and 742 nm. The transition energies were calculated by solving the 1-dimensional Schrödinger equation, with a strain model [109,181]. Using the average GaAs QD axial height of 13.3 nm, and a strained conduction band offset estimate of 0.51 eV [182], we expect 6 conduction band energy levels. The lowest energy light-hole transition is 709 nm, and the lowest energy heavy-hole transitions are 763, 747, and 715 nm, which is consistent with the RT PL

spectrum presented in the inset of Figure 6.4a. The PL emission is at a lower energy than the photocurrent response from these devices, which is consistent with our previous work with InAsP QDs within InP NWs [77]. For a QD system with multiple energy levels, as is the case here, the lowest energy levels will be most filled with excess carriers from the laser excitation source, resulting in strongest PL emission form those lowest energy transitions [73]. When detecting photocurrent from interband absorption within the QDs, the two methods of extracting the carriers from the potential wells are thermal excitation over the barrier, or tunneling through the barrier. For both of those processes, the larger the potential barrier (lower the QD energy levels), the less probable is the extraction of those carriers, which leads to the observation of higher photocurrent absorption energies compared with the lower PL emission energies. Such a difference between absorption and emission was observed in GaAs solar cells with InAs QDs in the intrinsic layer [183]. To investigate this further, the absorption edge, as defined by the wavelength at which the responsivity is 0.01% of its maximum value, for both the sample with QDs (solid line) and without QDs (dashed line) is plotted in inset (b) of Figure 6.4. The sample without QDs has an absorption edge consistent with the room temperature ZB GaP bandgap, and is invariant with the applied reverse bias voltage. The sample with QDs shows a gradual increase in the absorption edge as the applied reverse bias is increased. Under a larger electric field, it is more likely that the carriers absorbed within the deeper QD energy levels will undergo field-assisted tunneling, contributing to the responsivity of the device at longer wavelengths, which is consistent with inset (b) of Figure 6.4.

Figure 6.5 shows filled contour plots of responsivity versus voltage for different illumination wavelengths for samples (a) with QDs, and (b) without QDs. The colour map scale is the same for both Figure 6.5a and b. The dashed line represents the room temperature ZB GaAs band edge, and is used as a guide to the eye.

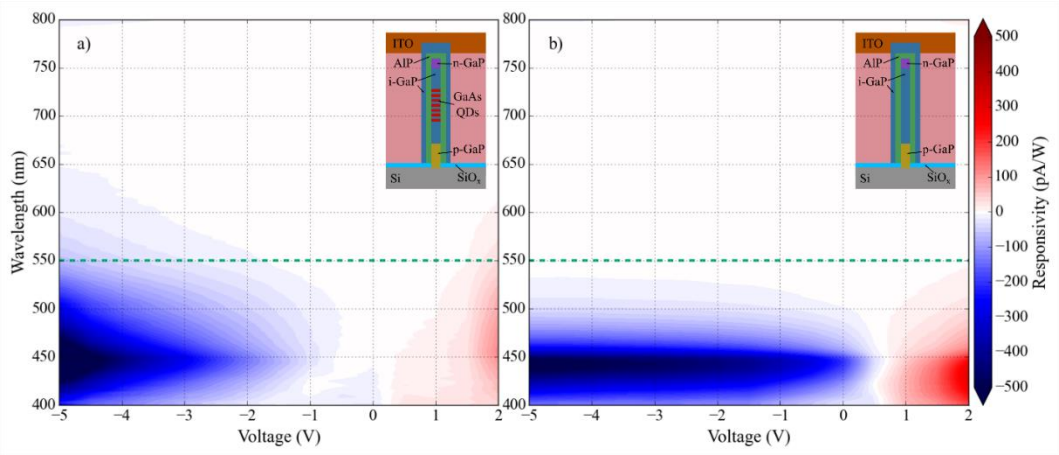

Figure 6.5: Voltage- and wavelength-dependent responsivity for (a) sample A with 15 GaAs QDs and (b) sample B without QDs. The colour map indicates the responsivity in pA/W for both plots. The insets for each plot show the schematic of each device.

6.4 Conclusion

The fabrication of a GaP NW-based p-n junction device was demonstrated on a Si substrate. Troubleshooting of the fabrication steps revealed issues with exposing the NW core for electrical contacting. The wet chemical etch step does not guarantee the removal of the passivation shell at the top of the NW, leading to a contact which has a barrier of AlP and GaP prior to the n-type GaP section. In addition to this, 15 GaAs QDs were embedded within the intrinsic region of the p-n junction, with the goal of extracting electron-hole pairs absorbed at lower

energies than the bandgap of GaP. The device demonstrated an enhanced responsivity beyond the GaP band edge, attributed to absorption within the QDs.

7. Conclusion and Future Work

7.1 Thesis Summary

The work in this thesis covered the growth and characterization of InAs/GaAs QDs embedded within InP/GaP NWs on a Si substrate. Both Au-assisted and self-assisted NWs were studied. Many challenges associated with NW growth, characterization, and device processing have been discussed.

The following conclusions are made for Au-assisted InP/InAs NWs:

a) The InAs QDs were analyzed using SEM and TEM, allowing a growth model to be developed for the VLS growth regime. Using this model, it was possible to tune the dimensions and composition of the embedded QDs. It was observed that the NWs were randomly placed with multiple growth directions and a spread in NW diameters and heights. This type of NW growth resulted in a spread of QD dimensions and composition, which reduced the performance of a QDIP device, as summarized in Chapter 1. This was overcome through the use of a patterned substrate to control the distribution of NWs.

b) The NWs were passivated using a larger bandgap material, which separated the charge carriers from recombination sites at the surface of the NW. The studies of both InP/AlInP and GaAs/GaP passivation schemes showed an improvement in the PL intensity from the bandgap emission of the NWs, demonstrating the effectiveness of this technique.

c) The composition of $InAs_xP_{1-x}$ QDs was varied from x = 100% to x = 25%, which allowed the tuning of the PL emission from both ensemble and single NW measurements. This was demonstrated at both 10 K and room temperature, showing promise towards operating a room temperature photodetector device.

d) The QD-based NW devices were contacted using ITO as the top contact and through the growth substrate as the bottom contact, allowing photocurrent measurements to be performed. The response of the devices showed peaks corresponding to interband absorption within the QDs, which were tuned using QD composition. The measurements were performed at room temperature, showing an IR response.

The growth of self-assisted InP NWs on patterned Si was studied. A very low yield of NWs was obtained. The following conclusions can be made about this study:

a) The optimal temperature and V/III flux ratio for InP NW growth were found to be 480 ^{o}C and 6, respectively. A qualitative discussion of the effects of temperature and V/III flux ratio was presented, explaining the yields of In droplet vs InP crystallites.

b) FIB was used to prepare cross-sectional samples of In droplets and crystallites. A bowl shape was discovered at the In/InP and Si interface, compared with the expected flat interface, such as that of GaP NWs on Si.

The growth of self-catalyzed GaP NWs on patterned Si was studied. The following conclusions are made:

a) The effect of V/III flux ratio on the growth of GaP NWs was studied. For the VLS growth regime in the axial direction, the NW diameter was determined by the diameter of the Ga seed particle. At a lower V/III flux ratio, there was less P_2 supplied to the Ga droplet, resulting in an excess of Ga supply, which expanded the volume of the droplet. A larger NW diameter was observed at these conditions. However, at a high V/III flux ratio, there was an excess of P_2 supplied to the Ga droplet, which reduced the droplet volume, resulting in a smaller NW diameter.

b) The growth rate of the NWs grown under various V/III flux ratios was studied using TEM analysis of GaAsP marker layers within the NWs. This analysis confirmed that the NW axial growth rate is group V limited, showing a clear dependence of the growth rate on the V/III flux ratio.

c) Through SEM analysis it was found that there were two types of NWs present within the samples: those that kept the Ga seed particle throughout the entire growth, and those that had the Ga droplet consumed part way through. The two NW populations followed different growth mechanisms, as studied through both SEM and TEM.

GaP NW p-n junction devices were fabricated, with and without GaAs QD insertions in the intrinsic region. The following conclusions are made:

a) The p-n junction devices showed diode behaviour, which is, to our knowledge, the first time a GaP NW p-n junction was demonstrated. The junction was electrically characterized in the dark and under broadband illumination.

b) The device with GaAs QDs was investigated with PL and electrical measurements at room temperature. The PL showed emission corresponding to the interband energy transition with the GaAs QDs. The wavelength-dependent photocurrent measurements showed absorption beyond the bandgap of GaP, attributed to the collection of carriers absorbed within the GaAs QDs.

7.2 Future Work

The work presented in this thesis has demonstrated the feasibility of QDIP devices within the NW architecture on a Si substrate operating at room temperature. In the case of unpatterned Au-assisted InP NW growth, presented in Chapter 3, it is deemed that the random arrangement of NWs and a distribution of diameter, height, and orientation is a detriment to the successful operation of NW-based devices, leading to a shift toward patterned NW growth. There is also a strong motivation toward self-assisted NW growth to eliminate Au from the manufacturing process, leading to the study presented in Section 5.2. The yield of patterned self-assisted InP NWs was very low, with the TEM work presented showing an anomalous bowl shape at the Si-InP interface. This is one of the likely culprits of low NW yield, and warrants further investigation. Potential solutions could involve a study of RIE etch times, HF wet etch times, or even In pre-deposition techniques.

The growth of both the Au-assisted InP NWs and the self-assisted NWs resulted in many stacking faults and twin planes, which are detrimental to electrical and optical properties of the devices. Specifically, the PL measurements of the QDs resulted in broad linewidths of the emission peaks. A detailed study of the effects of growth temperature, V/III flux ratios, growth rates, and any pre-growth processing steps (such as Ga pre-deposition, or RIE and HF etch conditions) is highly recommended in order to achieve defect free NW growth regimes, which have been demonstrated for other growth techniques. A recommended starting point would be the growth of low V/III ratio NWs, presented in Section 5.1. These NWs resulted in less stacking faults than their high V/III flux ratio counterparts, likely due to the larger Ga droplet.

If the growth of defect free NWs can be achieved, then the QD devices presented in this thesis can be studied further. A narrow linewidth emission would allow the precise mapping of the transition energies, allowing a power dependence study of excitons and bi-excitons. In addition, it would be interesting to determine how the effect of heterostructures and various passivation layers would affect the emission from these QDs. Such a study can be used to expand on the available strain models relevant to the materials and crystal structures associated with NW growth.

The most pressing issue with the GaP NW p-n junction devices is proper passivation, which can be best evaluated with a study similar to that presented in Chapter 4. It is important to determine if AlP is an effective material, with some other options available, such as AlGaP or even ZnS (this research group has

experience with chemical passivation methods, such as sulfur passivation of GaAs NW solar cells [129]). An advantage of using alternate materials to AlP is that the capping layer step can be avoided, simplifying the contacting scheme. If a suitable alternative cannot be found, then it is important to find a proper technique for exposing the NW core for contacting. One likely candidate is the use of sonication to remove the top sections of the NWs. The n-type section of the device can be made larger to extend far (> 500 nm) above the BCB polymer, allowing sonication to break off the NW tips. It would be important to have this break occur in the middle of the n-type section, and preferably limit its exposure to water by utilizing the nitrogen glove box.

Once the GaP p-n junction device is optimized electrically, it would be a suitable architecture for studying the behaviour of QDs within NWs. It would be possible to undertake temperature-dependent photocurrent measurements under varying biases to better understand which processes are responsible for the photocurrent generated.

8. References

[1] R. S. Wagner and W. C. Ellis, “Vapor-liquid-solid mechanism of single crystal growth,” *Appl. Phys. Lett.*, vol. 4, no. 5, pp. 89–90, 1964.

[2] M. C. Plante and R. R. LaPierre, “Growth mechanisms of GaAs nanowires by gas source molecular beam epitaxy,” *J. Cryst. Growth*, vol. 286, no. 2, pp. 394–399, 2006.

[3] M. S. Gudiksen, L. J. Lauhon, J. Wang, D. C. Smith, and C. M. Lieber, “Growth of nanowire superlattice structures for nanoscale photonics and electronics,” *Nature*, vol. 415, no. 6872, pp. 617–620, 2002.

[4] H. J. Joyce, J. Wong-Leung, Q. Gao, H. Hoe Tan, and C. Jagadish, “Phase perfection in zinc blende and wurtzite III-V nanowires using basic growth parameters,” *Nano Lett.*, vol. 10, no. 3, pp. 908–915, 2010.

[5] M. A. Verheijen, G. Immink, T. de Smet, M. T. Borgström, and E. P. A. M. Bakkers, “Growth kinetics of heterostructured GaP-GaAs nanowires,” *J. Am. Chem. Soc.*, vol. 128, no. 4, pp. 1353–1359, 2006.

[6] S. C. Lyu, Y. Zhang, H. Ruh, H. J. Lee, and C. J. Lee, “Synthesis of high-purity Gap nanowires using a vapor deposition method,” *Chem. Phys. Lett.*, vol. 367, no. 5–6, pp. 717–722, 2003.

[7] M. S. Gudiksen and C. M. Lieber, “Diameter-selective synthesis of semiconductor nanowires,” *J. Am. Chem. Soc.*, vol. 122, no. 36, pp. 8801–8802, 2000.

[8] H. W. Seo, S. Y. Bae, J. Park, H. Yang, and S. Kim, "Synthesis of gallium phosphide nanowires via sublimation method," *Chem. Commun.*, no. 21, pp. 2564–2565, 2002.

[9] H. Wang, M. Sun, K. Ding, M. T. Hill, and C. Z. Ning, "A top-down approach to fabrication of high quality vertical heterostructure nanowire arrays," *Nano Lett*, vol. 11, no. 4, pp. 1646–1650, 2011.

[10] B. Tian, X. Zheng, T. J. Kempa, Y. Fang, N. Yu, G. Yu, J. Huang, and C. M. Lieber, "Coaxial silicon nanowires as solar cells and nanoelectronic power sources," *Nature*, vol. 449, no. 7164, pp. 885–889, 2007.

[11] P. Nguyen, H. T. Ng, and M. Meyyappan, "Growth of individual vertical germanium nanowires," *Adv. Mater.*, vol. 17, no. 5, pp. 549–553, 2005.

[12] P. Mohan, J. Motohisa, and T. Fukui, "Controlled growth of highly uniform, axial/radial direction-defined, individually addressable InP nanowire arrays," *Nanotechnology*, vol. 16, no. 12, pp. 2903–2907, Dec. 2005.

[13] M. T. Robson, V. G. Dubrovskii, and R. R. LaPierre, "Conditions for high yield of selective-area epitaxy InAs nanowires on SiO_x/Si(111) substrates," *Nanotechnology*, vol. 26, no. 46, p. 465301, 2015.

[14] M. D. Thompson, A. Alhodaib, A. P. Craig, A. Robson, A. Aziz, A. Krier, J. Svensson, L. E. Wernersson, A. M. Sanchez, and A. R. J. Marshall, "Low Leakage-Current InAsSb Nanowire Photodetectors on Silicon," *Nano Lett.*, vol. 16, no. 1, pp. 182–187, 2016.

[15] P. Kuyanov, J. Boulanger, and R. R. LaPierre, “Control of GaP nanowire morphology by group V flux in gas source molecular beam epitaxy,” *J. Cryst. Growth*, vol. 462, pp. 29–34, 2017.

[16] S. J. Gibson, J. P. Boulanger, and R. R. LaPierre, “Opportunities and pitfalls in patterned self-catalyzed GaAs nanowire growth on silicon,” *Semicond. Sci. Technol.*, vol. 28, no. 10, p. 105025, 2013.

[17] P. Yang, H. Yan, S. Mao, R. Russo, J. Johnson, R. Saykally, N. Morris, J. Pham, R. He, and H. J. Choi, “Controlled growth of ZnO nanowires and their optical properties,” *Adv. Funct. Mater.*, vol. 12, no. 5, pp. 323–331, 2002.

[18] T. Kuykendall, P. J. Pauzauskie, Y. Zhang, J. Goldberger, D. Sirbuly, J. Denlinger, and P. Yang, “Crystallographic alignment of high-density gallium nitride nanowire arrays,” *Nat. Mater.*, vol. 3, no. 8, pp. 524–528, 2004.

[19] C. M. Haapamaki and R. R. LaPierre, “Mechanisms of molecular beam epitaxy growth in InAs/InP nanowire heterostructures,” *Nanotechnology*, vol. 22, no. 33, p. 335602, Aug. 2011.

[20] E. P. A. M. Bakkers, J. A. van Dam, S. De Franceschi, L. P. Kouwenhoven, M. Kaiser, M. Verheijen, H. Wondergem, and P. van der Sluis, “Epitaxial growth of InP nanowires on germanium,” *Nat. Mater.*, vol. 3, no. 11, pp. 769–773, 2004.

[21] P. K. Mohseni, G. Lawson, A. Adronov, and R. R. LaPierre, “Hybrid GaAs-nanowire-carbon-nanotube flexible photovoltaics,” *IEEE J. Sel. Top. Quantum Electron.*, vol. 17, no. 4, pp. 1070–1077, 2011.

[22] W. Metaferia, A. R. Persson, K. Mergenthaler, F. Yang, W. Zhang, A. Yartsev, R. Wallenberg, M. E. Pistol, K. Deppert, L. Samuelson, and M. H. Magnusson, "GaAsP Nanowires Grown by Aerotaxy," *Nano Lett.*, vol. 16, no. 9, pp. 5701–5707, 2016.

[23] T. Mårtensson, C. P. T. Svensson, B. A. Wacaser, M. W. Larsson, W. Seifert, K. Deppert, A. Gustafsson, L. R. Wallenberg, and L. Samuelson, "Epitaxial III-V nanowires on silicon," *Nano Lett.*, vol. 4, no. 10, pp. 1987–1990, 2004.

[24] K. M. Azizur-Rahman and R. R. LaPierre, "Optical design of a mid-wavelength infrared InSb nanowire photodetector," *Nanotechnology*, vol. 27, no. 31, pp. 1–8, 2016.

[25] V. Mourik, K. Zuo, S. M. Frolov, S. R. Plissard, E. P. A. M. Bakkers, and L. P. Kouwenhoven, "Signatures of Majorana Fermions in Hybrid Superconductor-Semiconductor Nanowire Devices," *Science*, vol. 336, no. 6084, pp. 1003–1007, 2012.

[26] C. Colombo, M. Heiß, M. Grätzel, and A. Fontcuberta i Morral, "Gallium arsenide p-i-n radial structures for photovoltaic applications," *Appl. Phys. Lett.*, vol. 94, no. 17, 2009.

[27] W. Wei, X. Bao, C. Soci, Y. Ding, Z. Wang, and D. Wang, "Direct Heteroepitaxy of Vertical InAs Nanowire Array on Si (111) Substrates for Broadband Photovoltaics and Photodetection," *Nano Lett.*, vol. 9, no. 8, pp. 2926–2934, 2009.

[28] H. Goto, K. Nosaki, K. Tomioka, S. Hara, K. Hiruma, J. Motohisa, and T. Fukui, "Growth of core-shell InP nanowires for photovoltaic application by selective-area metal organic vapor phase epitaxy," *Appl. Phys. Express*, vol. 2, no. 3, pp. 3–6, 2009.

[29] H. P. T. Nguyen, Y. L. Chang, I. Shih, and Z. Mi, "InN p-i-n nanowire solar cells on Si," *IEEE J. Sel. Top. Quantum Electron.*, vol. 17, no. 4, pp. 1062–1069, 2011.

[30] Y. B. Tang, Z. H. Chen, H. S. Song, C. S. Lee, H. T. Cong, H. M. Cheng, W. J. Zhang, I. Bello, and S. T. Lee, "Vertically aligned p-type single-crystalline GaN nanorod arrays on n-type Si for heterojunction photovoltaic cells," *Nano Lett.*, vol. 8, no. 12, pp. 4191–4195, 2008.

[31] J. V Holm, H. I. Jørgensen, P. Krogstrup, J. Nygård, H. Liu, and M. Aagesen, "Surface-passivated GaAsP single-nanowire solar cells exceeding 10% efficiency grown on silicon," *Nat. Commun.*, vol. 4, p. 1498, 2013.

[32] Y. Q. Bie, Z. M. Liao, H. Z. Zhang, G. R. Li, Y. Ye, Y. B. Zhou, J. Xu, Z. X. Qin, L. Dai, and D. P. Yu, "Self-powered, ultrafast, visible-blind UV detection and optical logical operation based on ZnO/GaN nanoscale p-n junctions," *Adv. Mater.*, vol. 23, no. 5, pp. 649–653, 2011.

[33] C. Yang, C. J. Barrelet, F. Capasso, and C. M. Lieber, "Single p-type / intrinsic / n-type silicon nanowires as nanoscale avalanche photodetectors," *Nano Lett.*, vol. 6, pp. 2929–34, 2006.

[34] H. Pettersson, J. Tragårdh, A. I. Persson, L. Landln, D. Hessman, and L. Samuelson, “Infrared photodetectors in heterostructure nanowires,” *Nano Lett.*, vol. 6, no. 2, pp. 229–232, 2006.

[35] X. Duan, Y. Huang, R. Agarwal, and C. M. Lieber, “Single-nanowire electrically driven lasers,” *Nature*, vol. 421, no. 6920, pp. 241–245, 2003.

[36] F. Qian, Y. Li, S. Gradečak, H.-G. Park, Y. Dong, Y. Ding, Z. L. Wang, and C. M. Lieber, “Multi-quantum-well nanowire heterostructures for wavelength-controlled lasers,” *Nat. Mater.*, vol. 7, no. 9, pp. 701–706, 2008.

[37] Y. Xiao, C. Meng, X. Wu, and L. Tong, “Single mode lasing in coupled nanowires,” *Appl. Phys. Lett.*, vol. 99, no. 2, pp. 2009–2012, 2011.

[38] E. Lai, W. Kim, and P. Yang, “Vertical nanowire array-based light emitting diodes,” *Nano Res.*, vol. 1, no. 2, pp. 123–128, 2008.

[39] K. Tomioka, J. Motohisa, S. Hara, K. Hiruma, and T. Fukui, “GaAs/AlGaAs core multishell nanowire-based light-emitting diodes on Si,” *Nano Lett.*, vol. 10, no. 5, pp. 1639–1644, 2010.

[40] E. D. Minot, F. Kelkensberg, M. van Kouwen, J. A. van Dam, L. P. Kouwenhoven, V. Zwiller, M. T. Borgström, O. Wunnicke, M. A. Verheijen, and E. P. A. M. Bakkers, “Single quantum dot nanowire LEDs,” *Nano Lett.*, vol. 7, no. 2, pp. 367–371, 2007.

[41] T. Bryllert, L.-E. Wernersson, T. Löwgren, and L. Samuelson, “Vertical wrap-gated nanowire transistors,” *Nanotechnology*, vol. 17, no. 11, pp. S227–S230, 2006.

[42] M. Egard, S. Johansson, A. C. Johansson, K. M. Persson, A. W. Dey, B. M. Borg, C. Thelander, L. E. Wernersson, and E. Lind, “Vertical InAs nanowire wrap gate transistors with ft> 7 GHz and fmax > 20 GHz,” *Nano Lett.*, vol. 10, no. 3, pp. 809–812, 2010.

[43] Q. Qing, Z. Jiang, L. Xu, R. Gao, L. Mai, and C. M. Lieber, “Free-standing kinked nanowire transistor probes for targeted intracellular recording in three dimensions,” *Nat. Nanotechnol.*, vol. 9, no. 2, pp. 142–147, 2013.

[44] G. Bulgarini, M. E. Reimer, M. B. Bavinck, K. D. Jöns, D. Dalacu, P. J. Poole, E. P. A. M. Bakkers, and V. Zwiller, “Nanowire waveguides launching single photons in a Gaussian mode for ideal fiber coupling,” *Nano Letters*, vol. 14, no. 7. pp. 4102–4106, 2014.

[45] M. A. M. Versteegh, M. E. Reimer, K. D. Jöns, D. Dalacu, P. J. Poole, A. Gulinatti, A. Giudice, and V. Zwiller, “Observation of strongly entangled photon pairs from a nanowire quantum dot,” *Nat. Commun.*, vol. 5, p. 5298, 2014.

[46] R. R. LaPierre, M. Robson, K. M. Azizur-Rahman, and P. Kuyanov, “A review of III–V nanowire infrared photodetectors and sensors,” *J. Phys. D. Appl. Phys.*, vol. 50, no. 12, p. 123001, 2017.

[47] R. R. LaPierre, A. C. E. Chia, S. J. Gibson, C. M. Haapamaki, J. Boulanger, R. Yee, P. Kuyanov, J. Zhang, N. Tajik, N. Jewell, and K. M. A. Rahman, “III–V

nanowire photovoltaics: Review of design for high efficiency," *Phys. Status Solidi RRL*, vol. 7, no. 10, pp. 815-830, 2013.

[48] A. Orieux, M. A. M. Versteegh, K. D. Jöns, and S. Ducci, "Semiconductor devices for entangled photon pair generation: a review," *Rep. Prog. Phys.*, vol. 80, p. 076001, 2017.

[49] A. I. Persson, M. W. Larsson, S. Stenström, B. J. Ohlsson, L. Samuelson, and L. R. Wallenberg, "Solid-phase diffusion mechanism for GaAs nanowire growth," *Nat. Mater.*, vol. 3, no. 10, pp. 677–681, 2004.

[50] M. C. Plante and R. R. Lapierre, "Control of GaAs nanowire morphology and crystal structure," *Nanotechnology*, vol. 19, no. 49, p. 495603, Dec. 2008.

[51] S. A. Fortuna and X. Li, "Metal-catalyzed semiconductor nanowires: a review on the control of growth directions," *Semicond. Sci. Technol.*, vol. 25, p. 24005, 2010.

[52] J. Wang, S. R. Plissard, M. A. Verheijen, L. F. Feiner, A. Cavalli, and E. P. A. M. Bakkers, "Reversible switching of InP nanowire growth direction by catalyst engineering," *Nano Lett.*, vol. 13, no. 8, pp. 3802–3806, 2013.

[53] T. I. Kamins, R. S. Williams, Y. Chen, Y. L. Chang, and Y. A. Chang, "Chemical vapor deposition of Si nanowires nucleated by TiSi2 islands on Si," *Appl. Phys. Lett.*, vol. 76, no. 5, pp. 562–564, 2000.

[54] K. Kang, D. A. Kim, H. S. Lee, C. J. Kim, J. E. Yang, and M. H. Jo, "Low-temperature deterministic growth of Ge nanowires using Cu solid catalysts," *Adv. Mater.*, vol. 20, no. 24, pp. 4684–4690, 2008.

[55] Y. Wang, V. Schmidt, S. Senz, and U. Gösele, "Epitaxial growth of silicon nanowires using an aluminium catalyst," *Nat. Nanotechnol.*, vol. 1, no. 3, pp. 186–189, 2006.

[56] E. C. Garnett, W. Liang, and P. Yang, "Growth and electrical characteristics of platinum-nanoparticle-catalyzed silicon nanowires," *Adv. Mater.*, vol. 19, no. 19, pp. 2946–2950, 2007.

[57] S. Dubois, O. Palais, M. Pasquinelli, S. Martinuzzi, and C. Jaussaud, "Influence of substitutional metallic impurities on the performances of p -type crystalline silicon solar cells: The case of gold," *J. Appl. Phys.*, vol. 100, p.123502, 2006.

[58] S. Breuer, C. Pfüller, T. Flissikowski, O. Brandt, H. T. Grahn, L. Geelhaar, and H. Riechert, "Suitability of Au- and self-assisted GaAs nanowires for optoelectronic applications," *Nano Lett.*, vol. 11, no. 3, pp. 1276–1279, 2011.

[59] T. Mårtensson, P. Carlberg, M. Borgström, L. Montelius, W. Seifert, and L. Samuelson, "Nanowire arrays defined by nanoimprint lithography," *Nano Lett.*, vol. 4, no. 4, pp. 699–702, 2004.

[60] S. Plissard, G. Larrieu, X. Wallart, and P. Caroff, "High yield of self-catalyzed GaAs nanowire arrays grown on silicon via gallium droplet positioning," *Nanotechnology*, vol. 22, no. 27, p. 275602, 2011.

[61] A. Rogalski, "HgCdTe infrared detector material: history, status and outlook," *Reports Prog. Phys.*, vol. 68, no. 10, pp. 2267–2336, 2005.

[62] A. Rogalski, "Infrared Detectors for the future," *ACTA Phys. Pol. A*, vol. 116, no. 3, 2009.

[63] P. Norton, "HgCdTe Infrared Detectors," *Opto-Electronics Rev.*, vol. 10, no. 3, pp. 159–174, 2002.

[64] L. J. Kozlowski, G. M. Williams, G. J. Sullivan, C. W. Farley, R. J. Anderson, J. Chen, A. Member, D. T. Cheung, W. E. Tennant, S. Member, and R. E. Dewames, "LWIR 128 X 128 GaAs / AlGaAs Multiple Quantum Well Hybrid Focal Plane Array," *IEEE Trans. Electron Devices*, vol. 38, 1991.

[65] A. D. Stiff-Roberts, "Quantum-dot infrared photodetectors: a review," *J. Nanophotonics*, vol. 3, no. 1, p. 31607, 2009.

[66] J. X. Chen, a. Markus, a. Fiore, U. Oesterle, R. P. Stanley, J. F. Carlin, R. Houdré, M. Ilegems, L. Lazzarini, L. Nasi, M. T. Todaro, E. Piscopiello, R. Cingolani, M. Catalano, J. Katcki, and J. Ratajczak, "Tuning InAs/GaAs quantum dot properties under Stranski-Krastanov growth mode for 1.3 μm applications," *J. Appl. Phys.*, vol. 91, no. 10, pp. 6710-6716, 2002.

[67] K. Dick, J. Bolinsson, B. Borg, and J. Johansson, "Controlling the abruptness of axial heterojunctions in III–V nanowires: Beyond the reservoir effect," *Nano Lett.*, vol. 12, pp. 3200-3206, 2012.

[68] H. Pettersson, J. Trägårdh, A. I. Persson, L. Landin, D. Hessman, and L. Samuelson, "Infrared photodetectors in heterostructure nanowires," *Nano Lett.*, vol. 6, pp. 229-232, 2006.

[69] W. Wei, X. Bao, C. Soci, Y. Ding, Z. Wang, and D. Wang, "Direct heteroepitaxy of vertical InAs nanowires on Si substrates for broad band photovoltaics and photodetection," *Nano Lett.*, vol. 9, pp. 2926-2934, 2009.

[70] A. C. E. Chia and R. R. LaPierre, "Contact planarization of ensemble nanowires," *Nanotechnology*, vol. 22, no. 24, p. 245304, 2011.

[71] J. Svensson, N. Anttu, and N. Vainorius, "Diameter-dependent photocurrent in InAsSb nanowire infrared photodetectors," *Nano Lett.*, vol. 13, no. 3, pp. 1380-1385, 2013.

[72] M. Tchernycheva, G. E. Cirlin, G. Patriarche, L. Travers, V. Zwiller, U. Perinetti, and J.-C. Harmand, "Growth and characterization of InP nanowires with InAsP insertions," *Nano Lett.*, vol. 7, no. 6, pp. 1500–1504, 2007.

[73] M. H. M. van Weert, N. Akopian, U. Perinetti, M. P. van Kouwen, R. E. Algra, M. A. Verheijen, P. A. M. B. Erik, L. P. Kouwenhoven, and V. Zwiller, "Selective excitation and detection of spin states in a single nanowire quantum dot," *Nano Lett.*, vol. 9, no. 5, pp. 1989–1993, 2009.

[74] S. N. Dorenbos, H. Sasakura, M. P. Van Kouwen, N. Akopian, S. Adachi, N. Namekata, M. Jo, J. Motohisa, Y. Kobayashi, K. Tomioka, T. Fukui, S. Inoue, H. Kumano, C. M. Natarajan, R. H. Hadfield, T. Zijlstra, T. M. Klapwijk, V. Zwiller,

and I. Suemune, “Position controlled nanowires for infrared single photon emission,” *Appl. Phys. Lett.*, vol. 97, no. 17, pp. 10–13, 2010.

[75] D. Dalacu, K. Mnaymneh, X. Wu, J. Lapointe, G. C. Aers, P. J. Poole, and R. L. Williams, “Selective-area vapor-liquid-solid growth of tunable InAsP quantum dots in nanowires,” *Appl. Phys. Lett.*, vol. 98, no. 25, p. 251101, 2011.

[76] J.-C. Harmand, F. Jabeen, L. Liu, G. Patriarche, K. Gauthron, P. Senellart, D. Elvira, and A. Beveratos, “InP1−xAsx quantum dots in InP nanowires: A route for single photon emitters,” *J. Cryst. Growth*, vol. 378, no. 31, pp. 519–523, 2013.

[77] P. Kuyanov and R. R. LaPierre, “Photoluminescence and photocurrent from InP nanowires with InAsP quantum dots grown on Si by molecular beam epitaxy,” *Nanotechnology*, vol. 26, no. 31, p. 315202, 2015.

[78] A. Darbandi, O. Salehzadeh, P. Kuyanov, R. R. LaPierre, and S. P. Watkins, “Surface passivation of tellurium-doped GaAs nanowires by GaP: Effect on electrical conduction,” *J. Appl. Phys.*, vol. 115, no. 23, p. 234305, 2014.

[79] T. Mårtensson and P. Carlberg, “Nanowire arrays defined by nanoimprint lithography,” *Nano Lett.*, vol. 4, no. 4, pp. 699–702, 2004.

[80] S. J. Gibson, J. P. Boulanger, and R. R. LaPierre, “Opportunities and pitfalls in patterned self-catalyzed GaAs nanowire growth on silicon,” *Semicond. Sci. Technol.*, vol. 28, no. 10, p. 105025, 2013.

[81] D. B. Williams and C. B. Carter, *Transmission Electron Microscopy*. Boston, MA: Springer US, 2009.

[82] M. Knoll and E. Ruska, "Das Elektronenmikroskop," *Zeitschrift fur Phys.*, vol. 79, no. 9–10, p. 699, 1932.

[83] E. Ruska, "The Development of the Electron Microscope and of Electron Microscopy (Nobel Lecture)," *Angew. Chemie*, vol. 26, no. 7, pp. 595–706, 1987.

[84] A. Bogner, P. H. Jouneau, G. Thollet, D. Basset, and C. Gauthier, "A history of scanning electron microscopy developments: Towards 'wet-STEM' imaging," *Micron*, vol. 38, no. 4, pp. 390–401, 2007.

[85] J. I. Goldstein, D. E. Newbury, P. Echlin, D. C. Joy, C. E. Lyman, E. Lifshin, L. Sawyer, and J. R. Michael, *Scanning Electron Microscopy and X-ray Microanalysis*. Boston, MA: Springer US, 2003.

[86] M. C. Plante and R. R. LaPierre, "Au-assisted growth of GaAs nanowires by gas source molecular beam epitaxy: Tapering, sidewall faceting and crystal structure," *J. Cryst. Growth*, vol. 310, no. 2, pp. 356–363, 2008.

[87] P. Kuyanov and R. R. LaPierre, "Photoluminescence and photocurrent from InP nanowires with InAsP quantum dots grown on Si by molecular beam epitaxy," *Nanotechnology*, vol. 26, no. 31, p. 315202, 2015.

[88] A. Rogalski, J. Antoszewski, and L. Faraone, "Third-generation infrared photodetector arrays," *J. Appl. Phys.*, vol. 105, p. 91101, 2009.

[89] G. Konstantatos, I. Howard, A. Fischer, S. Hoogland, J. Clifford, E. Klem, L. Levina, and E. H. Sargent, "Ultrasensitive solution-cast quantum dot photodetectors," *Nature*, vol. 442, pp. 180–183, 2006.

[90] A. Vasanelli, R. Ferreira, and G. Bastard, "Continuous Absorption Background and Decoherence in Quantum Dots," *Phys. Rev. Lett.*, vol. 89, no. 21, p. 216804, 2002.

[91] K. Tateno, G. Zhang, H. Gotoh, and T. Sogawa, "VLS growth of alternating InAsP/InP heterostructure nanowires for multiple-quantum-dot structures," *Nano Lett.*, vol. 12, no. 6, pp. 2888–2893, 2012.

[92] S. N. Dorenbos, H. Sasakura, M. P. Van Kouwen, N. Akopian, S. Adachi, N. Namekata, M. Jo, J. Motohisa, Y. Kobayashi, K. Tomioka, T. Fukui, S. Inoue, H. Kumano, C. M. Natarajan, R. H. Hadfield, T. Zijlstra, T. M. Klapwijk, V. Zwiller, and I. Suemune, "Position controlled nanowires for infrared single photon emission," *Appl. Phys. Lett.*, vol. 97, no. 17, pp. 13–16, 2010.

[93] G. Zhang, K. Tateno, M. D. Birowosuto, M. Notomi, T. Sogawa, and H. Gotoh, "Controlled 1.1-1.6 μm luminescence in gold-free multi-stacked InAs/InP heterostructure nanowires," *Nanotechnology*, vol. 26, no. 11, p. 115704, 2015.

[94] D. Dalacu, K. Mnaymneh, J. Lapointe, X. Wu, P. J. Poole, G. Bulgarini, V. Zwiller, and M. E. Reimer, "Ultraclean emission from InAsP quantum dots in defect-free wurtzite InP nanowires," *Nano Lett.*, vol. 12, no. 11, pp. 5919–5923, 2012.

[95] J. C. Harmand, F. Jabeen, L. Liu, G. Patriarche, K. Gauthron, P. Senellart, D. Elvira, and A. Beveratos, "InP1-xAsx quantum dots in InP nanowires: A route for single photon emitters," *J. Cryst. Growth*, vol. 378, no. 31, pp. 519–523, 2013.

[96] M. T. Borgström, V. Zwiller, E. Müller, and A. Imamoglu, "Optically bright quantum dots in single nanowires," *Nano Lett.*, vol. 5, no. 7, pp. 1439–1443, 2005.

[97] M. E. Reimer, G. Bulgarini, N. Akopian, M. Hocevar, M. B. Bavinck, M. a Verheijen, E. P. a M. Bakkers, L. P. Kouwenhoven, and V. Zwiller, "Bright single-photon sources in bottom-up tailored nanowires," *Nat. Commun.*, vol. 3, p. 737, 2012.

[98] N. Sköld, M. E. Pistol, K. A. Dick, C. Pryor, J. B. Wagner, L. S. Karlsson, and L. Samuelson, "Microphotoluminescence studies of tunable wurtzite InAs0.85 P0.15 quantum dots embedded in wurtzite InP nanowires," *Phys. Rev. B - Condens. Matter Mater. Phys.*, vol. 80, no. 4, pp. 15–18, 2009.

[99] M. P. van Kouwen, M. H. M. van Weert, M. E. Reimer, N. Akopian, U. Perinetti, R. E. Algra, E. P. A. M. Bakkers, L. P. Kouwenhoven, and V. Zwiller, "Single quantum dot nanowire photodetectors," *Appl. Phys. Lett.*, vol. 97, no. 11, p. 113108, 2010.

[100] C. M. Haapamaki, J. Baugh, and R. R. LaPierre, "Facilitating growth of InAs–InP core–shell nanowires through the introduction of Al," *J. Cryst. Growth*, vol. 345, no. 1, pp. 11–15, 2012.

[101] M. R. Ramdani, J. C. Harmand, F. Glas, G. Patriarche, and L. Travers, "Arsenic Pathways in Self-Catalyzed Growth of GaAs Nanowires," *Cryst. Growth Des.*, vol. 13, no. 1, pp. 91–96, 2013.

[102] S. J. Gibson and R. R. LaPierre, “Model of patterned self-assisted nanowire growth,” *Nanotechnology*, vol. 25, no. 41, p. 415304, 2014.

[103] A. C. E. Chia, M. Tirado, F. Thouin, R. Leonelli, D. Comedi, and R. R. LaPierre, “Surface depletion and electrical transport model of AlInP-passivated GaAs nanowires,” *Semicond. Sci. Technol.*, vol. 28, no. 10, p. 105026, 2013.

[104] M. Montazeri, M. Fickenscher, L. M. Smith, H. E. Jackson, J. Yarrison-Rice, J. H. Kang, Q. Gao, H. H. Tan, C. Jagadish, Y. Guo, J. Zou, M.-E. Pistol, and C. E. Pryor, “Direct measure of strain and electronic structure in GaAs/GaP core-shell nanowires,” *Nano Lett.*, vol. 10, no. 3, pp. 880–886, 2010.

[105] L. S. Karlsson, M. W. Larsson, M. Pistol, W. Seifert, and J. Tra, “Growth and Optical Properties of Strained GaAs − Ga x In 1 - x P Core − Shell Nanowires,” *Nano Lett.*, vol. 5, no. 10, pp. 1943-1947, 2005.

[106] P. Parkinson, H. J. Joyce, Q. Gao, H. H. Tan, X. Zhang, J. Zou, C. Jagadish, L. M. Herz, and M. B. Johnston, “Carrier Lifetime and Mobility Enhancement in Nearly Defect-Free Core-Shell Nanowires Measured Using Time-Resolved Terahertz Spectroscopy,” *Nano Lett.*, vol. 9, no. 9, pp. 3349–3353, 2009.

[107] N. Tajik, C. M. Haapamaki, and R. R. LaPierre, “Photoluminescence model of sulfur passivated p-InP nanowires,” *Nanotechnology*, vol. 23, no. 31, p. 315703, 2012.

[108] P. Liu, H. Huang, X. Liu, M. Bai, D. Zhao, Z. Tang, X. Huang, J. Y. Kim, and J. Guo, “Core-shell nanowire diode based on strain-engineered bandgap,” *Phys. Status Solidi Appl. Mater. Sci.*, vol. 212, no. 3, pp. 617–622, 2015.

[109] M. Beaudoin and A. Bensaada, “Self-consistent determination of the band offsets in InAs x P 1 x / InP strained-layer quantum wells and the bowing parameter of bulk InAs x P 1 x,” *Phys. Rev. B.*, vol. 53, no. 4, pp. 1990–1996, 1996.

[110] R. R. LaPierre, A. Gustafsson, P. Kuyanov, C. M. Haapamaki, “Novel Luminescent Materials Based on Semiconductor Nanowires,” *ECS Trans*, vol. 61, no. 5, pp. 3–8, 2014.

[111] I. Vurgaftman, J. R. Meyer, and L. R. Ram-Mohan, “Band parameters for III–V compound semiconductors and their alloys,” *J. Appl. Phys.*, vol. 89, p. 5815, 2001.

[112] J. Miao, W. Hu, N. Guo, Z. Lu, X. Zou, L. Liao, S. Shi, P. Chen, Z. Fan, J. C. Ho, T. X. Li, X. S. Chen, and W. Lu, “Single InAs nanowire room-temperature near-infrared photodetectors,” *ACS Nano*, vol. 8, no. 4, pp. 3628–3635, 2014.

[113] Z. Liu, T. Luo, B. Liang, G. Chen, G. Yu, X. Xie, D. Chen, and G. Shen, “High-detectivity InAs nanowire photodetectors with spectral response from ultraviolet to near-infrared,” *Nano Res.*, vol. 6, no. 11, pp. 775–783, 2013.

[114] J. Svensson, N. Anttu, N. Vainorius, B. M. Borg, and L. E. Wernersson, “Diameter-dependent photocurrent in InAsSb nanowire infrared photodetectors,” *Nano Lett.*, vol. 13, no. 4, pp. 1380–1385, 2013.

[115] A. Maharjan, K. Pemasiri, P. Kumar, a. Wade, L. M. Smith, H. E. Jackson, J. M. Yarrison-Rice, a. Kogan, S. Paiman, Q. Gao, H. H. Tan, and C. Jagadish,

"Room temperature photocurrent spectroscopy of single zincblende and wurtzite InP nanowires," *Appl. Phys. Lett.*, vol. 94, no. 2009, p. 193115, 2009.

[116] E. D. Minot, F. Kelkensberg, M. Van Kouwen, J. A. Van Dam, L. P. Kouwenhoven, V. Zwiller, M. T. Borgström, O. Wunnicke, M. A. Verheijen, and E. P. A. M. Bakkers, "Single quantum dot nanowire LEDs," *Nano Lett.*, vol. 7, no. 2, pp. 367–371, 2007.

[117] F. Qian, S. Gradečak, Y. Li, C. Y. Wen, and C. M. Lieber, "Core/multishell nanowire heterostructures as multicolor, high-efficiency light-emitting diodes," *Nano Lett.*, vol. 5, no. 11, pp. 2287–2291, 2005.

[118] L. Tsakalakos, "Nanostructures for photovoltaics," *Mater. Sci. Eng. R Reports*, vol. 62, no. 6, pp. 175–189, 2008.

[119] M. A. Green, *Third generation photovoltaics : advanced solar energy conversion*. Springer, 2006.

[120] E. C. Garnett, M. L. Brongersma, Y. Cui, and M. D. McGehee, "Nanowire Solar Cells," *Annu. Rev. Mater. Res.*, vol. 41, no. 1, pp. 269–295, 2011.

[121] Y. Hu, R. R. LaPierre, M. Li, K. Chen, and J. J. He, "Optical characteristics of GaAs nanowire solar cells," *J. Appl. Phys.*, vol. 112, p.104311, 2012.

[122] C. Thelander, P. Agarwal, S. Brongersma, J. Eymery, L. F. Feiner, A. Forchel, M. Scheffler, W. Riess, B. J. Ohlsson, U. Gosele, and L. Samuelson, "Nanowire-based one-dimensional electronics," *Mater. Today*, vol. 9, no. 10, pp. 28–35, 2006.

[123] A. Gu, Y. Huo, S. Hu, T. Sarmiento, E. Pickett, D. Liang, S. Li, A. Lin, S. Thombare, Z. Yu, S. Fan, P. Mclntyre, Y. Cui, and J. Harris, "Design and growth of III-V nanowire solar cell arrays on low cost substrates," *Conf. Rec. IEEE Photovolt. Spec. Conf.*, pp. 2034–2037, 2010.

[124] B. M. Kayes, H. A. Atwater, and N. S. Lewis, "Comparison of the device physics principles of planar and radial p-n junction nanorod solar cells," *J. Appl. Phys.*, vol. 97, p. 114302, 2005.

[125] S. M. Sze and K. K. Ng, *Physics of semiconductor devices*. Wiley-Interscience, 2007.

[126] B. S. Simpkins, M. A. Mastro, C. R. Eddy, and P. E. Pehrsson, "Surface depletion effects in semiconducting nanowires," *J. Appl. Phys.*, vol. 103, p.104313, 2008.

[127] O. Salehzadeh, K. L. Kavanagh, and S. P. Watkins, "Controlled axial and radial Te-doping of GaAs nanowires," *J. Appl. Phys.*, vol. 112, p.054324, 2012.

[128] J. Lloyd-Hughes, S. K. E. Merchant, L. Fu, H. H. Tan, C. Jagadish, E. Castro-Camus, and M. B. Johnston, "Influence of surface passivation on ultrafast carrier dynamics and terahertz radiation generation in GaAs," *Appl. Phys. Lett.*, vol. 89, no. 23, 2006.

[129] N. Tajik, Z. Peng, P. Kuyanov, and R. R. LaPierre, "Sulfur passivation and contact methods for GaAs nanowire solar cells.," *Nanotechnology*, vol. 22, no. 22, p. 225402, 2011.

[130] O. Demichel, M. Heiss, J. Bleuse, H. Mariette, and I. A. Fontcuberta Morral, "Impact of surfaces on the optical properties of GaAs nanowires," *Appl. Phys. Lett.*, vol. 97, no. 20, pp. 1–4, 2010.

[131] C.-C. Chang, C.-Y. Chi, M. Yao, N. Huang, C.-C. Chen, J. Theiss, A. W. Bushmaker, S. Lalumondiere, T.-W. Yeh, M. L. Povinelli, C. Zhou, P. D. Dapkus, and S. B. Cronin, "Electrical and optical characterization of surface passivation in GaAs nanowires," *Nano Lett.*, vol. 12, no. 9, pp. 4484–4489, 2012.

[132] O. Salehzadeh, M. X. Chen, K. L. Kavanagh, and S. P. Watkins, "Rectifying characteristics of Te-doped GaAs nanowires," *Appl. Phys. Lett.*, vol. 99, no. 18, pp. 2009–2012, 2011.

[133] O. Salehzadeh and S. P. Watkins, "Control of GaAs nanowire morphology by group III precursor chemistry," *J. Cryst. Growth*, vol. 325, no. 1, pp. 5–9, 2011.

[134] O. Salehzadeh, K. L. Kavanagh, and S. P. Watkins, "Geometric limits of coherent III-V core/shell nanowires," *J. Appl. Phys.*, vol. 114, p. 054301, 2013.

[135] A. C. E. Chia, M. Tirado, Y. Li, S. Zhao, Z. Mi, D. Comedi, and R. R. LaPierre, "Electrical transport and optical model of GaAs-AlInP core-shell nanowires," *J. Appl. Phys.*, vol. 111, p. 094319, 2012.

[136] O. D. D. Couto, D. Sercombe, J. Puebla, L. Otubo, I. J. Luxmoore, M. Sich, T. J. Elliott, E. A. Chekhovich, L. R. Wilson, M. S. Skolnick, H. Y. Liu, and A. I. Tartakovskii, "Effect of a GaAsP shell on the optical properties of self-catalyzed

GaAs nanowires grown on silicon," *Nano Lett.*, vol. 12, no. 10, pp. 5269–5274, 2012.

[137] J. Wallentin, N. Anttu, D. Asoli, M. Huffman, I. Aberg, M. H. Magnusson, G. Siefer, P. Fuss-Kailuweit, F. Dimroth, B. Witzigmann, H. Q. Xu, L. Samuelson, K. Deppert, and M. T. Borgstrom, "InP Nanowire Array Solar Cells Achieving 13.8% Efficiency by Exceeding the Ray Optics Limit," *Science*, vol. 339, no. 6123, pp. 1057–1060, 2013.

[138] I. Aberg, G. Vescovi, D. Asoli, U. Naseem, J. P. Gilboy, C. Sundvall, A. Dahlgren, K. E. Svensson, N. Anttu, M. T. Bjork, and L. Samuelson, "A GaAs nanowire array solar cell with 15.3% efficiency at 1 sun," *IEEE J. Photovoltaics*, vol. 6, no. 1, pp. 185–190, 2016.

[139] X. Yan, B. Li, Y. Wu, X. Zhang, and X. Ren, "A single crystalline InP nanowire photodetector," *Appl. Phys. Lett.*, vol. 109, no. 5, p. 53109, 2016.

[140] H. Zhang, A. Messanvi, C. Durand, J. Eymery, P. Lavenus, A. Babichev, F. H. Julien, and M. Tchernycheva, "InGaN/GaN core/shell nanowires for visible to ultraviolet range photodetection," *Phys. Status Solidi Appl. Mater. Sci.*, vol. 940, no. 4, pp. 936–940, 2016.

[141] X. Dai, S. Zhang, Z. Wang, G. Adamo, H. Liu, Y. Huang, C. Couteau, and C. Soci, "GaAs/AlGaAs nanowire photodetector," *Nano Lett.*, vol. 14, no. 5, pp. 2688–2693, 2014.

[142] T. Mårtensson and C. Svensson, "Epitaxial III-V nanowires on silicon," *Nano Lett.*, vol. 4, no. 10, pp. 1987-1990, 2004.

[143] V. G. Dubrovskii, G. E. Cirlin, I. P. Soshnikov, A. A. Tonkikh, N. V. Sibirev, Y. B. Samsonenko, and V. M. Ustinov, "Diffusion-induced growth of GaAs nanowhiskers during molecular beam epitaxy: Theory and experiment," *Phys. Rev. B - Condens. Matter Mater. Phys.*, vol. 71, no. 20, pp. 5–7, 2005.

[144] M. C. Plante and R. R. LaPierre, "Growth mechanisms of GaAs nanowires by gas source molecular beam epitaxy," *J. Cryst. Growth*, vol. 286, no. 2, pp. 394–399, 2006.

[145] J. Bao, D. C. Bell, F. Capasso, J. B. Wagner, T. Mårtensson, J. Trägårdh, and L. Samuelson, "Optical properties of rotationally twinned InP nanowire heterostructures," *Nano Lett.*, vol. 8, no. 3, pp. 836–841, 2008.

[146] K. Tomioka, Y. Kobayashi, J. Motohisa, S. Hara, and T. Fukui, "Selective-area growth of vertically aligned GaAs and GaAs/AlGaAs core-shell nanowires on Si(111) substrate," *Nanotechnology*, vol. 20, no. 14, p. 145302, 2009.

[147] B. Bauer, A. Rudolph, M. Soda, A. Fontcuberta i Morral, J. Zweck, D. Schuh, and E. Reiger, "Position controlled self-catalyzed growth of GaAs nanowires by molecular beam epitaxy," *Nanotechnology*, vol. 21, no. 43, p. 435601, 2010.

[148] A. R. Madaria, M. Yao, C. Chi, N. Huang, C. Lin, R. Li, M. L. Povinelli, P. D. Dapkus, and C. Zhou, "Toward optimized light utilization in nanowire arrays using scalable nanosphere lithography and selected area growth," *Nano Lett.*, vol. 12, no. 6, pp. 2839–2845, 2012.

[149] J. Noborisaka, J. Motohisa, and T. Fukui, "Catalyst-free growth of GaAs nanowires by selective-area metalorganic vapor-phase epitaxy," *Appl. Phys. Lett.*, vol. 86, no. 21, p. 213102, 2005.

[150] P. Krogstrup, H. I. Jørgensen, E. Johnson, M. H. Madsen, C. B. Sørensen, A. F. I. Morral, M. Aagesen, J. Nygård, and F. Glas, "Advances in the theory of III–V nanowire growth dynamics," *J. Phys. D. Appl. Phys.*, vol. 46, no. 31, p. 313001, 2013.

[151] G. Priante, S. Ambrosini, V. G. Dubrovskii, a. Franciosi, and S. Rubini, "Stopping and resuming at will the growth of GaAs nanowires," *Cryst. Growth Des.*, vol. 13, no. 9, pp. 3976–3984, 2013.

[152] M. Heiss, E. Russo-Averchi, a. Dalmau-Mallorquí, G. Tütüncüoğlu, F. Matteini, D. Rüffer, S. Conesa-Boj, O. Demichel, E. Alarcon-Lladó, and a. Fontcuberta i Morral, "III-V nanowire arrays: growth and light interaction," *Nanotechnology*, vol. 25, no. 1, p. 014015, 2014.

[153] Y. Zhang, J. Wu, M. Aagesen, J. Holm, S. Hatch, M. Tang, S. Huo, and H. Liu, "Self-catalyzed ternary core-shell gaasp nanowire arrays grown on patterned si substrates by molecular beam epitaxy," *Nano Lett.*, vol. 14, no. 8, pp. 4542–4547, 2014.

[154] A. M. Munshi, D. L. Dheeraj, V. T. Fauske, D.-C. Kim, J. Huh, J. F. Reinertsen, L. Ahtapodov, K. Lee, B. Heidari, A. van Helvoort, B.-O. Fimland, and H. Weman, "Position Controlled Uniform GaAs Nanowires on Silicon using Nanoimprint Lithography," *Nano Lett.*, vol. 14, no. 2, pp. 960–966, 2014.

[155] W. S. Shi, Y. F. Zheng, N. Wang, C. S. Lee, and S. T. Lee, "Synthesis and microstructure of gallium phosphide nanowires," *J. Vac. Sci. Technol. B Microelectron. Nanom. Struct.*, vol. 19, no. 4, p. 1115, 2001.

[156] K. Hiruma, M. Yazawa, T. Katsuyama, K. Ogawa, K. Haraguchi, M. Koguchi, and H. Kakibayashi, "Growth and optical properties of nanometer-scale GaAs and InAs whiskers," *J. Appl. Phys.*, vol. 77, pp. 447–462, 1995.

[157] M. Borgström, K. Deppert, L. Samuelson, and W. Seifert, "Size- and shape-controlled GaAs nano-whiskers grown by MOVPE: A growth study," *J. Cryst. Growth*, vol. 260, no. 1–2, pp. 18–22, 2004.

[158] K. A. Dick, K. Deppert, T. Mårtensson, W. Seifert, and L. Samuelson, "Growth of GaP nanotree structures by sequential seeding of 1D nanowires," *J. Cryst. Growth*, vol. 272, no. 1–4 SPEC. ISS., pp. 131–137, 2004.

[159] C. P. T. Svensson, W. Seifert, M. W. Larsson, L. R. Wallenberg, J. Stangl, G. Bauer, and L. Samuelson, "Epitaxially grown GaP/GaAs 1− x P x / GaP double heterostructure nanowires for optical applications," *Nanotechnology*, vol. 16, no. 6, pp. 936–939, 2005.

[160] M. A. Verheijen, G. Immink, T. De Smet, M. T. Borgström, and E. P. A. M. Bakkers, "Growth kinetics of heterostructured GaP-GaAs nanowires," *J. Am. Chem. Soc.*, vol. 128, no. 4, pp. 1353–1359, 2006.

[161] P. K. Mohseni, C. Maunders, G. A. Botton, and R. R. LaPierre, "GaP/GaAsP/GaP core–multishell nanowire heterostructures on (111) silicon," *Nanotechnology*, vol. 18, no. 44, p. 445304, 2007.

[162] S. Assali, I. Zardo, S. Plissard, D. Kriegner, M. A. Verheijen, G. Bauer, A. Meijerink, A. Belabbes, F. Bechstedt, J. E. M. Haverkort, and E. P. A. M. Bakkers, "Direct band gap wurtzite gallium phosphide nanowires," *Nano Lett.*, vol. 13, no. 4, pp. 1559–1563, 2013.

[163] A. Pierret, M. Hocevar, S. L. Diedenhofen, R. E. Algra, E. Vlieg, E. C. Timmering, M. A. Verschuuren, G. W. G. Immink, M. A. Verheijen, and E. P. A. M. Bakkers, "Generic nano-imprint process for fabrication of nanowire arrays," *Nanotechnology*, vol. 21, no. 6, p. 65305, 2010.

[164] J. P. Boulanger and R. R. LaPierre, "Patterned gold-assisted growth of GaP nanowires on Si," *Semicond. Sci. Technol.*, vol. 27, no. 3, p. 35002, 2012.

[165] J. Tatebayashi, A. Lin, P. S. Wong, R. F. Hick, and D. L. Huffaker, "Visible light emission from self-catalyzed GaInP/GaP core-shell double heterostructure nanowires on silicon," *J. Appl. Phys.*, vol. 108, p.034315, 2010.

[166] G. Priante, G. Patriarche, F. Oehler, F. Glas, and J.-C. Harmand, "Abrupt GaP/GaAs Interfaces in Self-Catalyzed Nanowires," *Nano Lett.*, vol. 15, no. 9, pp. 6036–6041, 2015.

[167] M. T. Robson and R. R. LaPierre, "InAs nanowire growth modes on Si (111) by gas source molecular beam epitaxy," *J. Cryst. Growth*, vol. 436, pp. 1–11, 2016.

[168] J. P. Boulanger and R. R. LaPierre, "Unveiling transient GaAs/GaP nanowire growth behavior using group V oscillations," *J. Cryst. Growth*, vol. 388, pp. 116–123, 2014.

[169] S. Plissard, K. a Dick, G. Larrieu, S. Godey, A. Addad, X. Wallart, and P. Caroff, "Gold-free growth of GaAs nanowires on silicon: arrays and polytypism," *Nanotechnology*, vol. 21, no. 38, p. 385602, 2010.

[170] Q. Gao, V. G. Dubrovskii, P. Caroff, J. Wong-Leung, L. Li, Y. Guo, L. Fu, H. H. Tan, and C. Jagadish, "Simultaneous Selective-Area and Vapor-Liquid-Solid Growth of InP Nanowire Arrays," *Nano Lett.*, vol. 16, no. 7, pp. 4361–4367, 2016.

[171] M. C. Plante and R. R. LaPierre, "Analytical description of the metal-assisted growth of III-V nanowires: Axial and radial growths," *J. Appl. Phys.*, vol. 105, p. 114304, 2009.

[172] A. Standing, S. Assali, L. Gao, M. A. Verheijen, D. van Dam, Y. Cui, P. H. L. Notten, J. E. M. Haverkort, and E. P. A. M. Bakkers, "Efficient water reduction with gallium phosphide nanowires," *Nat. Commun.*, vol. 6, p. 7824, 2015.

[173] P. E. Sims, L. C. DiNetta, K. D. Cavanagh, and M. A. Goetz, "Gallium Phosphide energy converters," *Proc. Fourteenth Sp. Photovolt. Res. Technol. Conf. (SPRAT XIV)*, p. 231, 1995.

[174] T. E. Zipperian, R. J. Chaffin, and L. R. Dawson, "Recent Advances in Gallium Phosphide Junction Devices for High-Temperature Electronic Applications," *IEEE Trans. Ind. Electron.*, vol. IE-29, no. 2, pp. 129–136, 1982.

[175] S. Raychaudhuri and E. T. Yu, "Calculation of critical dimensions for wurtzite and cubic zinc blende coaxial nanowire heterostructures," *J. Vac. Sci. Technol. B Microelectron. Nanom. Struct.*, vol. 24, no. 4, p. 2053, 2006.

[176] J. Zhang, N. Dhindsa, A. C. E. Chia, J. Boulanger, I. Khodadad, S. Saini, and R. R. LaPierre, "Multi-spectral optical absorption in substrate-free nanowire arrays," *Appl. Phys. Lett.*, vol. 105, no. 12, 2014.

[177] J. Wu, A. Ramsay, A. Sanchez, Y. Zhang, D. Kim, F. Brossard, X. Hu, M. Benamara, M. E. Ware, Y. I. Mazur, G. J. Salamo, M. Aagesen, Z. Wang, and H. Liu, "Defect-Free Self-Catalyzed GaAs/GaAsP Nanowire Quantum Dots Grown on Silicon Substrate," *Nano Lett.*, vol. 16, no. 1, pp. 504-511, 2015.

[178] L. Yang, J. Motohisa, J. Takeda, M. Benyoucef, S. M. Ulrich, P. Michler, S. Yanase, H. Sasakura, S. Hara, and J. Motohisa, "Single-photon emission from InAsP quantum dots embedded in density-controlled InP nanowires Single-photon emission from InAsP quantum dots embedded in density-controlled InP nanowires," *Jap. Jour. of App. Phys.*, vol. 56, p. 04CP04, 2017.

[179] P. Martyniuk and A. Rogalski, "Quantum-dot infrared photodetectors: Status and outlook," *Prog. Quantum Electron.*, vol. 32, pp. 89–120, 2008.

[180] M. H. T. Dastjerdi, J. P. Boulanger, P. Kuyanov, M. Aagesen, and R. R. LaPierre, "Methods of Ga droplet consumption for improved GaAs nanowire solar cell efficiency," *Nanotechnology*, vol. 27, no. 47, p. 475403, 2016.

[181] F. H. Pollak, "Chapter 2 Effects of Homogeneous Strain on the Electronic and Vibrational Levels in Semiconductors," 1990, pp. 17–53.

[182] M. E. Pistol and C. Pryor, "Band structure of segmented semiconductor nanowires," *Phys. Rev. B*, vol. 80, no. 3, p. 35316, 2009.

[183] Y. Okada, T. Morioka, K. Yoshida, R. Oshima, Y. Shoji, T. Inoue, and T. Kita, “Increase in photocurrent by optical transitions via intermediate quantum states in direct-doped InAs/GaNAs strain-compensated quantum dot solar cell,” *J. Appl. Phys.*, vol. 109, p. 024301, 2011.

9. Appendix

This appendix contains the full data set of NW diameter visualization from Section 5.1.3. The data for each pitch is presented for each V/III flux ratio.

9.1 V/III Flux Ratio of 1

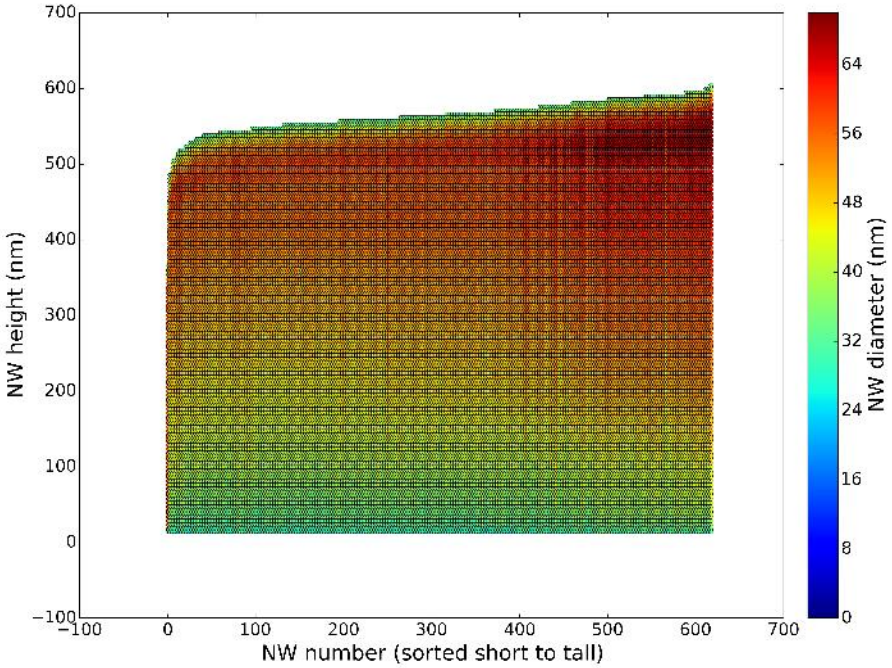

Figure 9.1: V/III flux ratio = 1, pitch = 360.

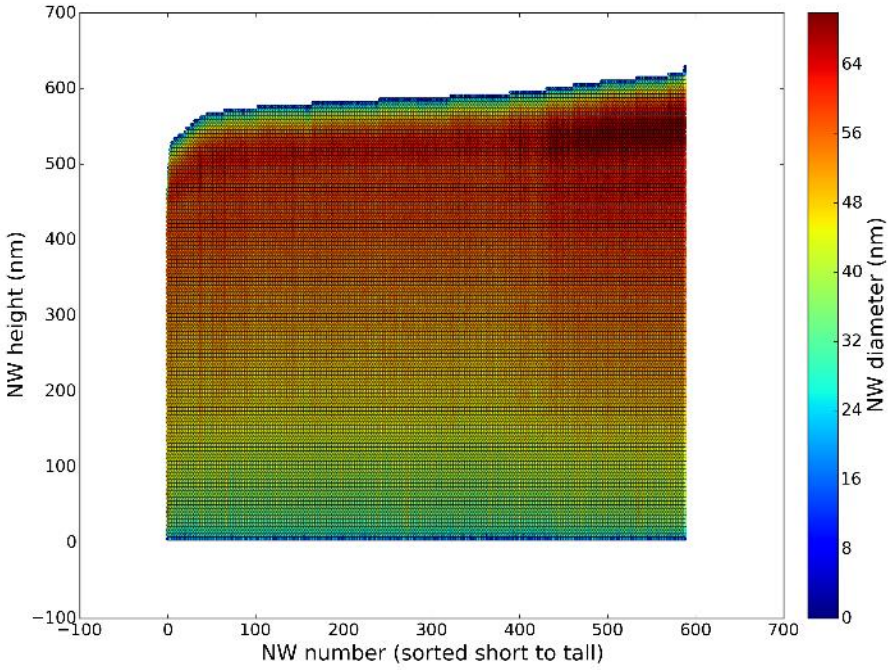

Figure 9.2: V/III flux ratio = 1, pitch = 440.

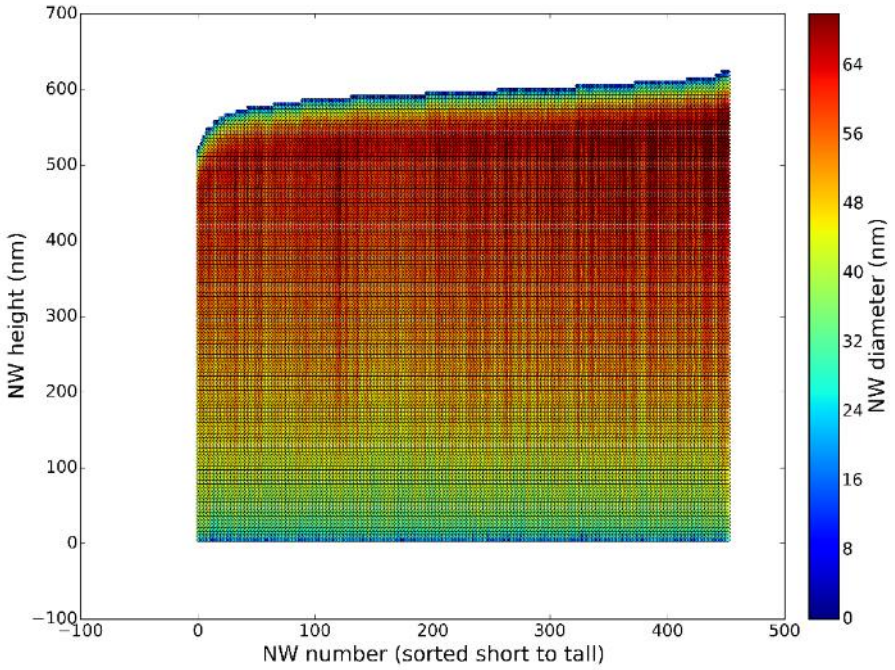

Figure 9.3: V/III flux ratio = 1, pitch = 520.

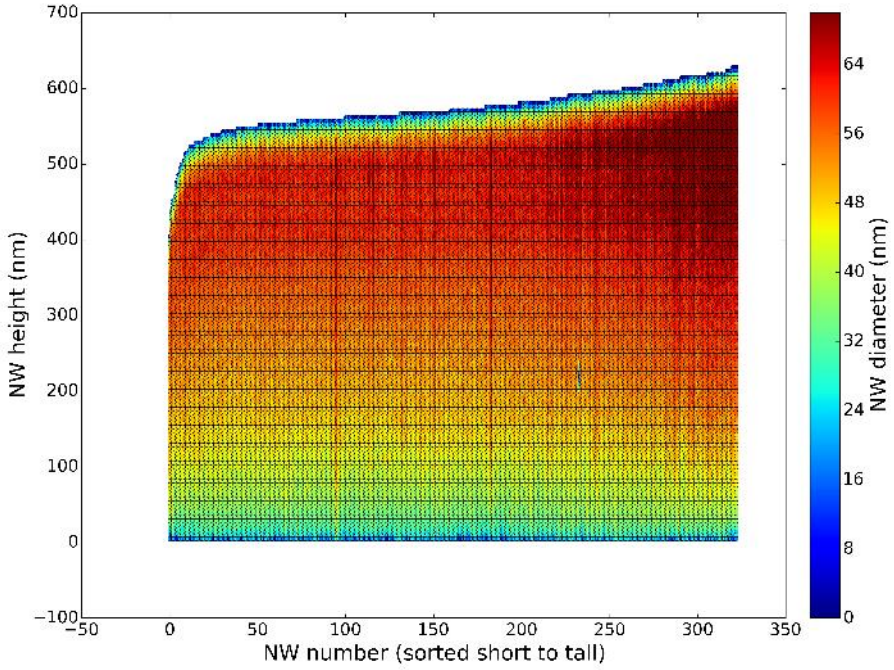

Figure 9.4: V/III flux ratio = 1, pitch = 600 nm.

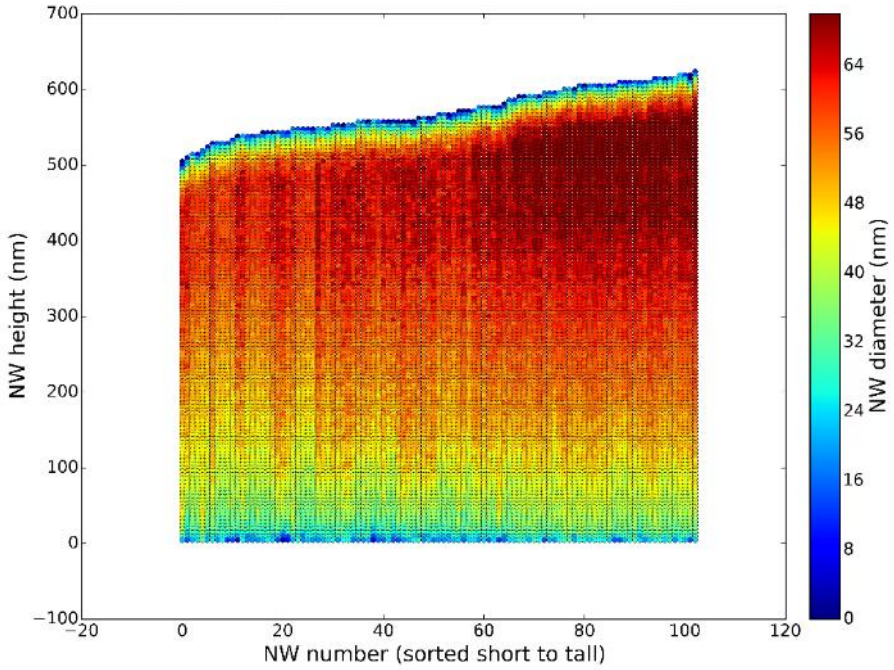

Figure 9.5: V/III flux ratio = 1, pitch = 1000 nm.

9.2 V/III Flux Ratio of 3

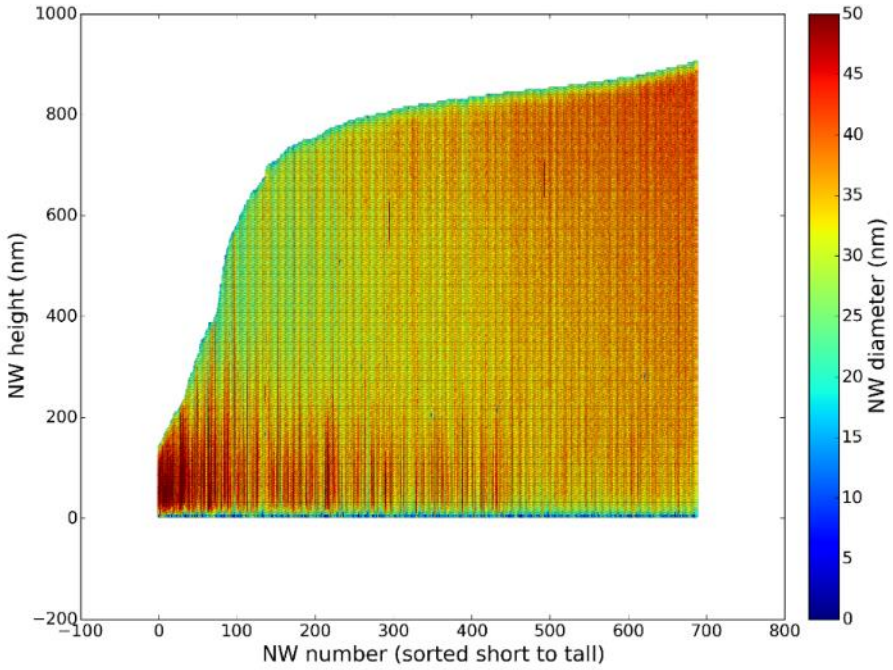

Figure 9.6: V/III flux ratio = 3, pitch = 360 nm.

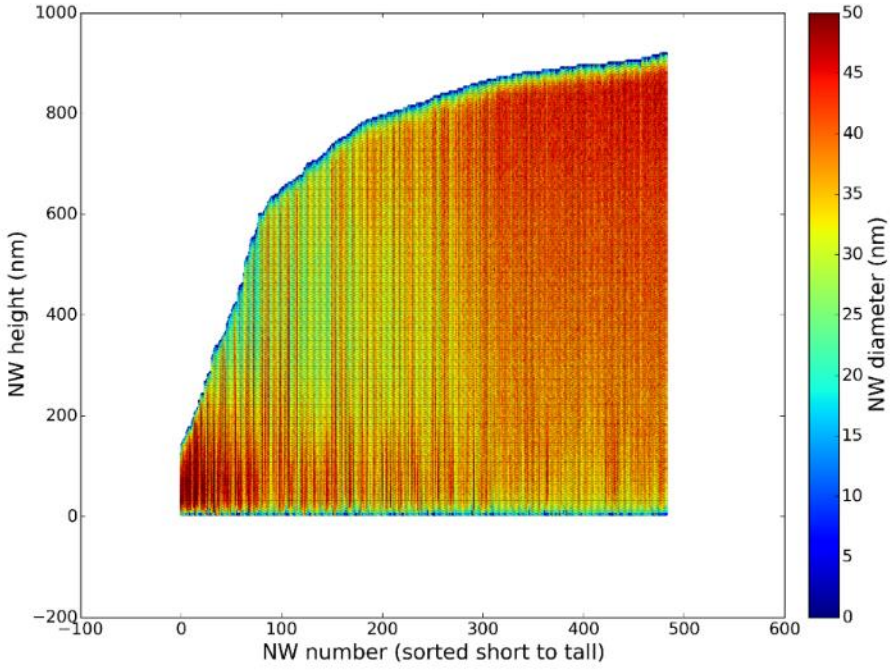

Figure 9.7: V/III flux ratio = 3, pitch = 440 nm.

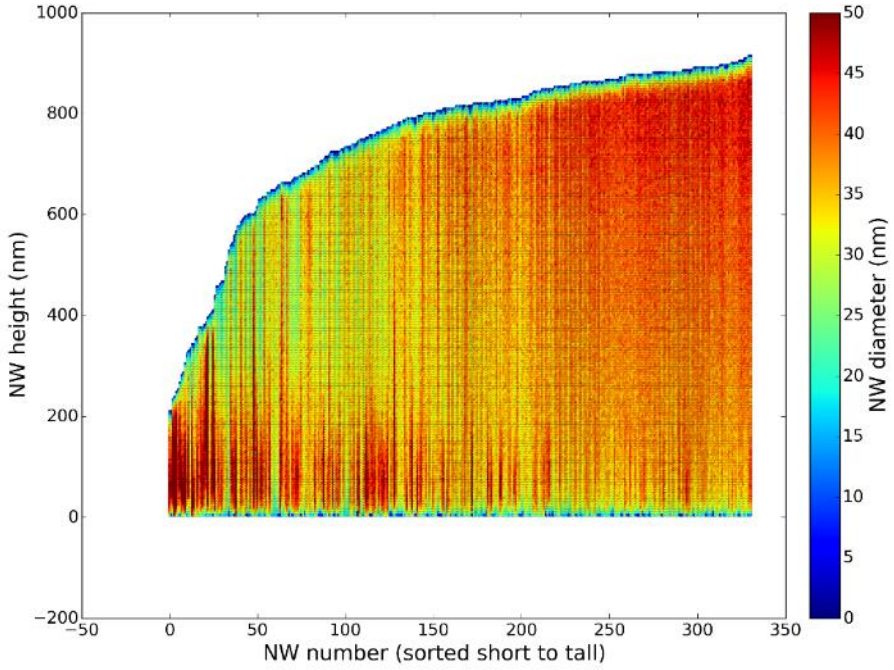

Figure 9.8: V/III flux ratio = 3, pitch = 520 nm.

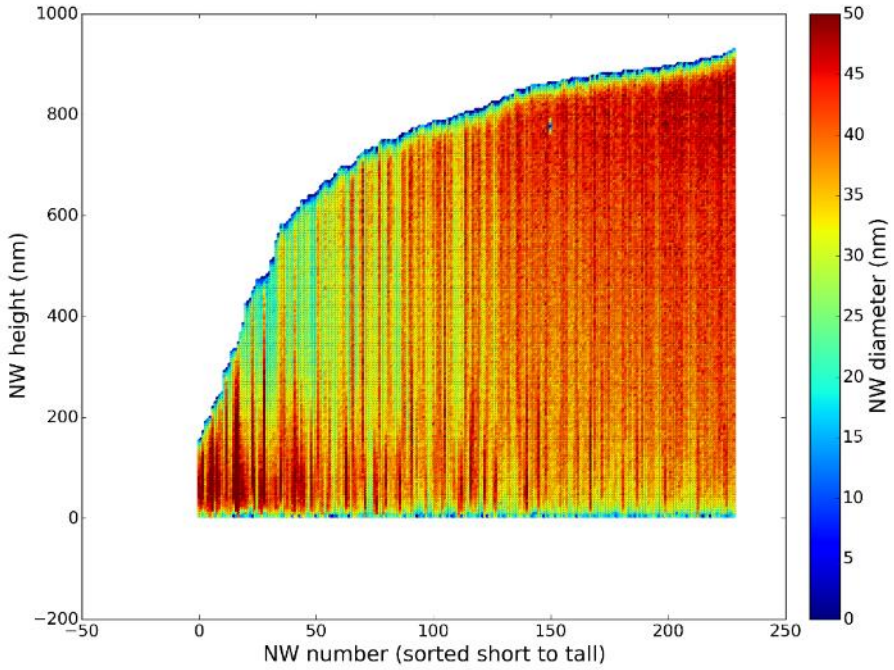

Figure 9.9: V/III flux ratio = 3, pitch = 600 nm.

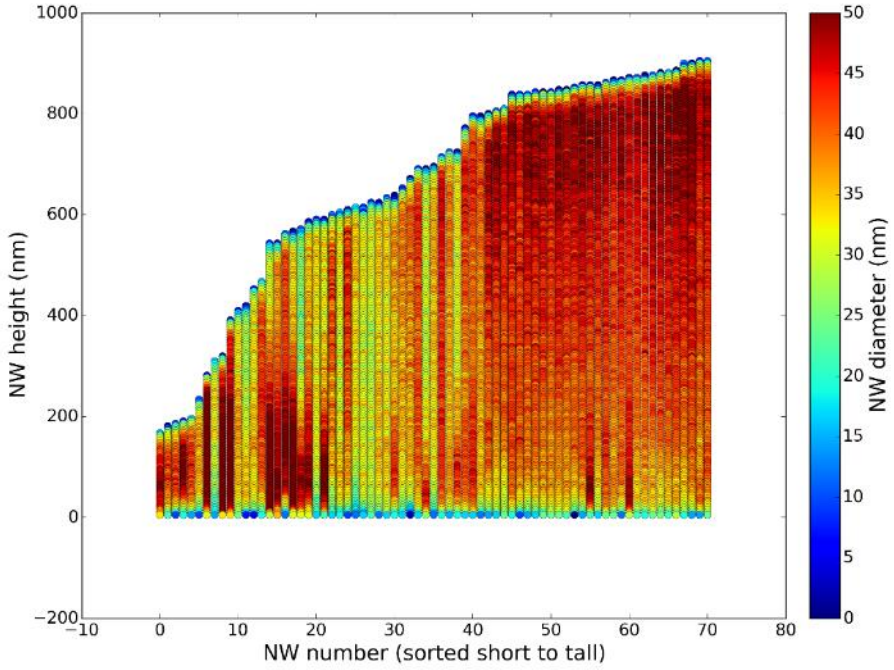

Figure 9.10: V/III flux ratio = 3, pitch = 1000 nm.

9.3 V/III Flux Ratio of 4

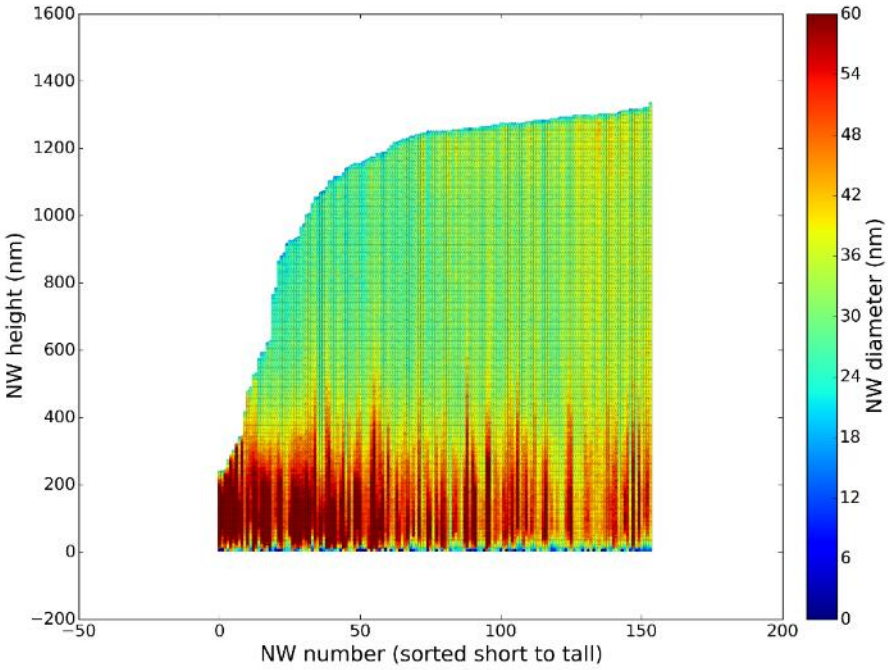

Figure 9.11: V/III flux ratio = 4, pitch = 360 nm.

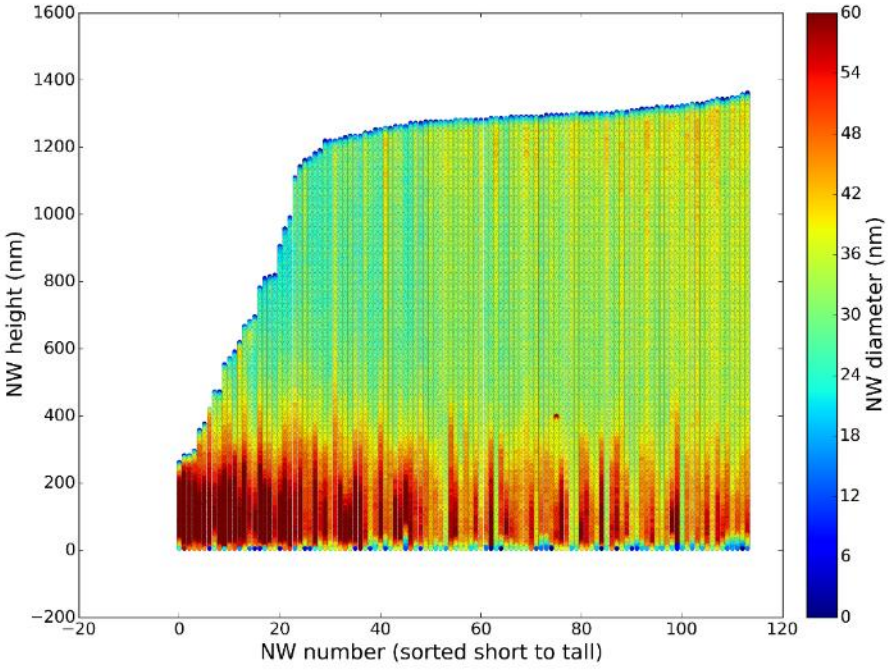

Figure 9.12: V/III flux ratio = 4, pitch = 440 nm.

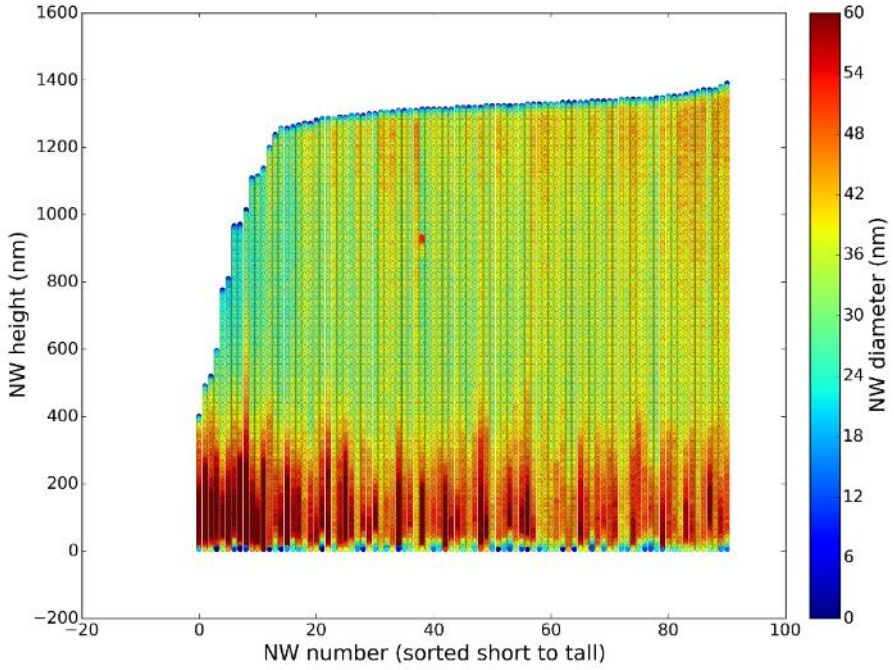

Figure 9.13: V/III flux ratio = 4, pitch = 520 nm.

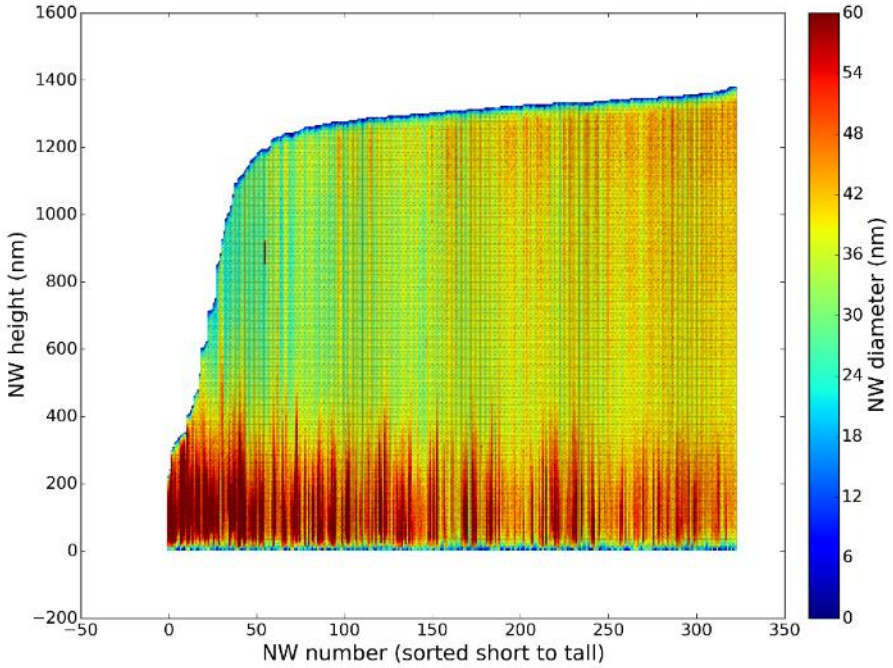

Figure 9.14: V/III flux ratio = 4, pitch = 600 nm.

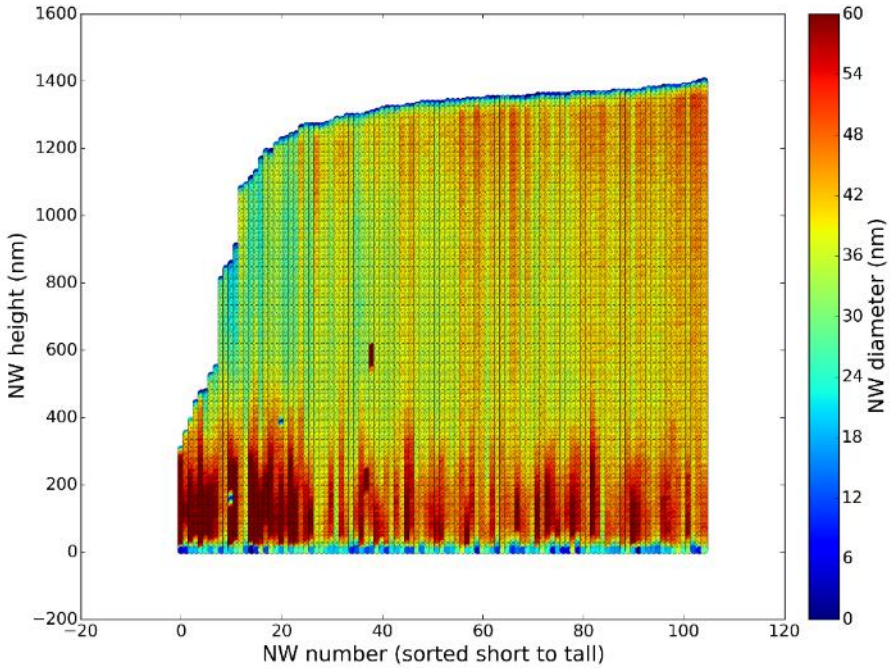

Figure 9.15: V/III flux ratio = 4, pitch = 1000 nm.

9.4 V/III Flux Ratio of 5

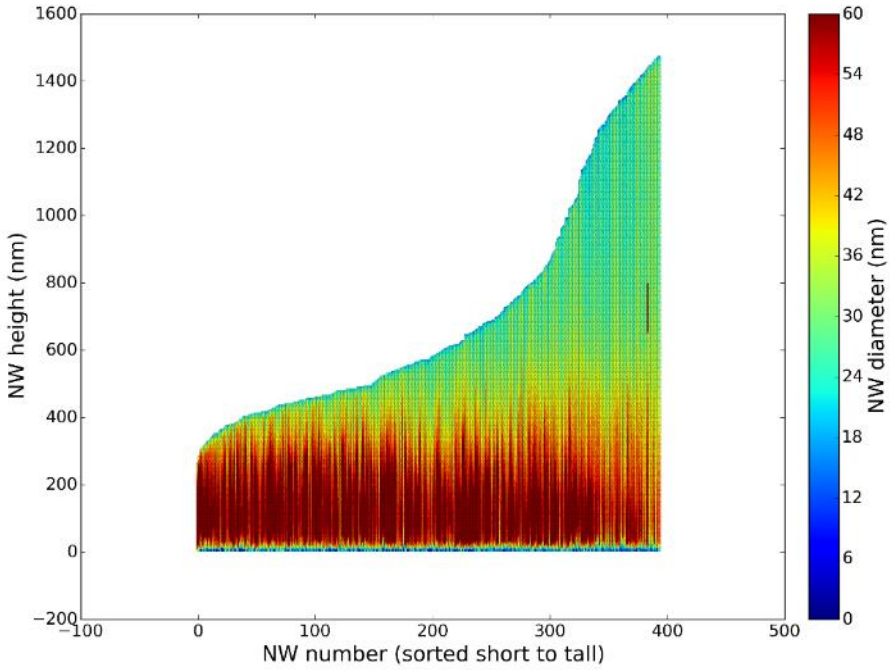

Figure 9.16: V/III flux ratio = 5, pitch = 360 nm.

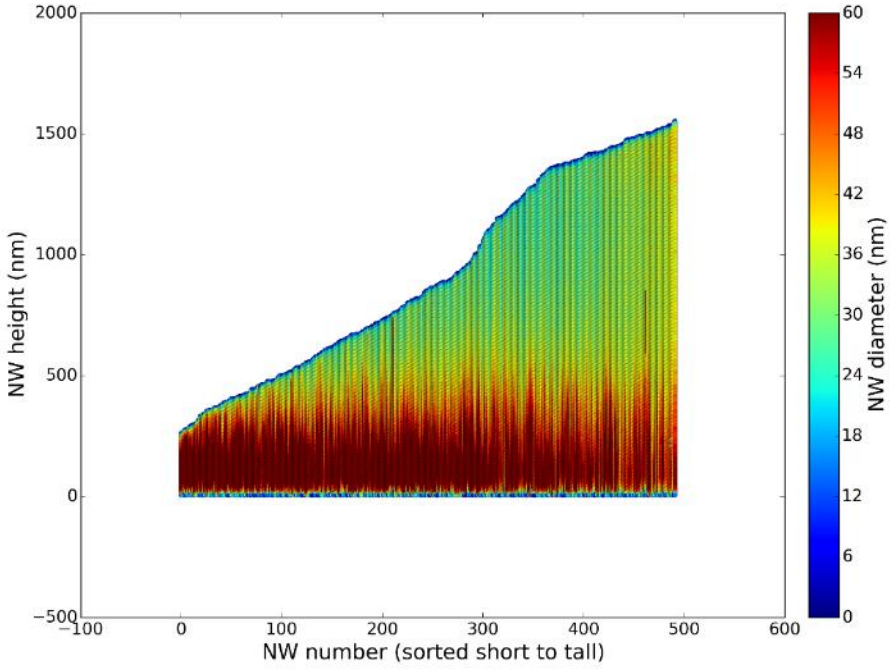

Figure 9.17: V/III flux ratio = 5, pitch = 440 nm.

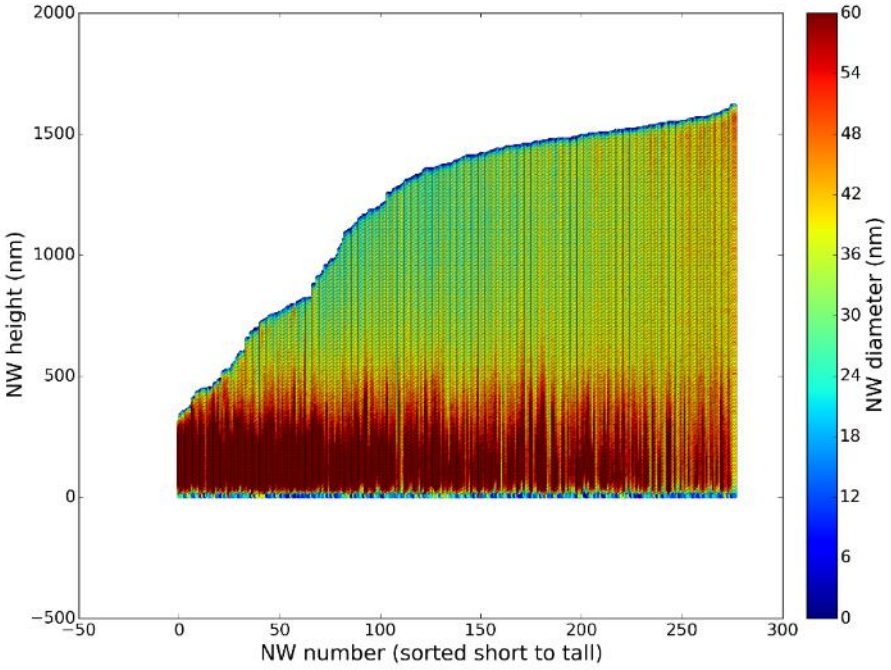

Figure 9.18: V/III flux ratio = 5, pitch = 520 nm.

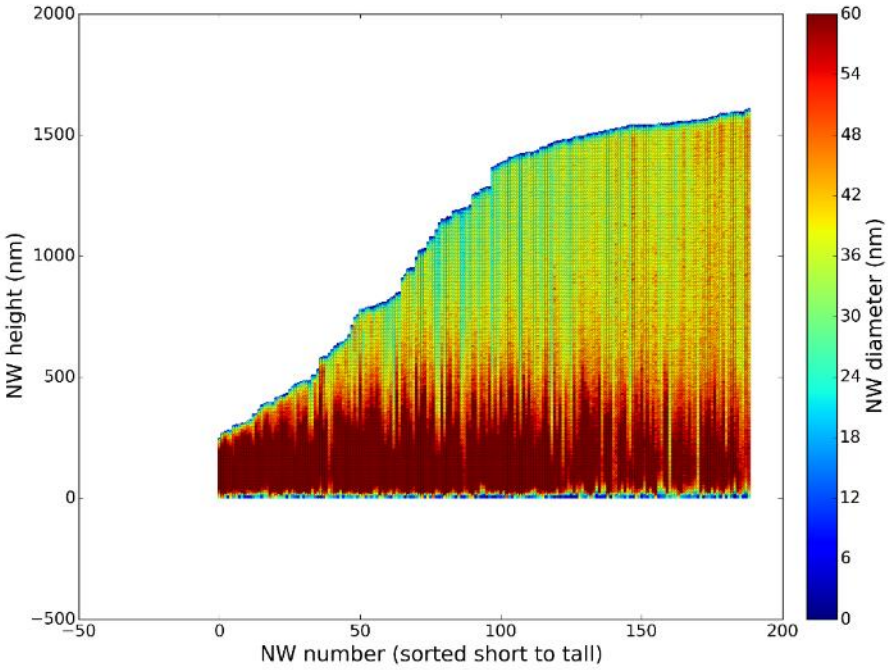

Figure 9.19: V/III flux ratio = 5, pitch = 600 nm.

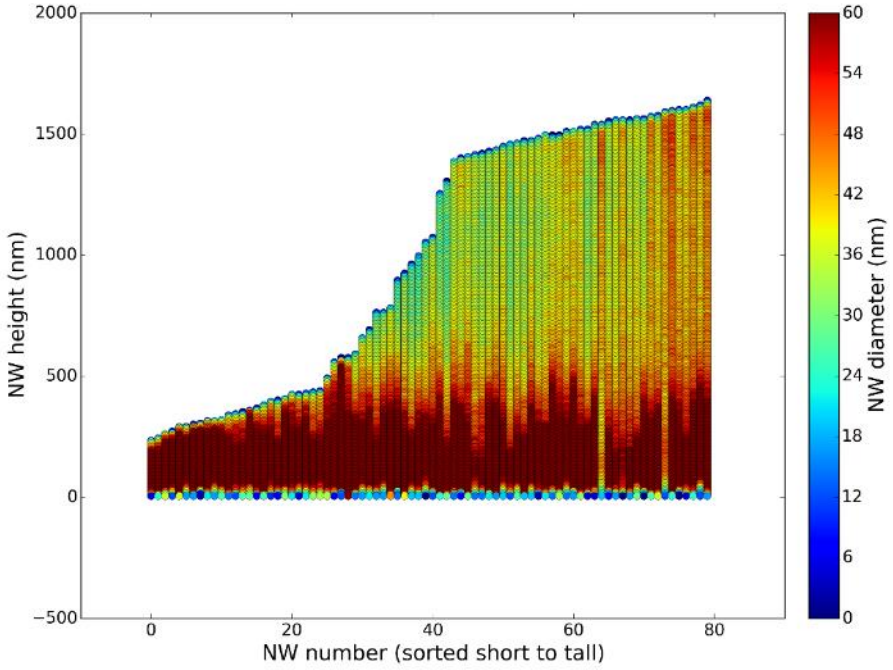

Figure 9.20: V/III flux ratio = 5, pitch = 1000 nm.

9.5 V/III Flux Ratio of 6

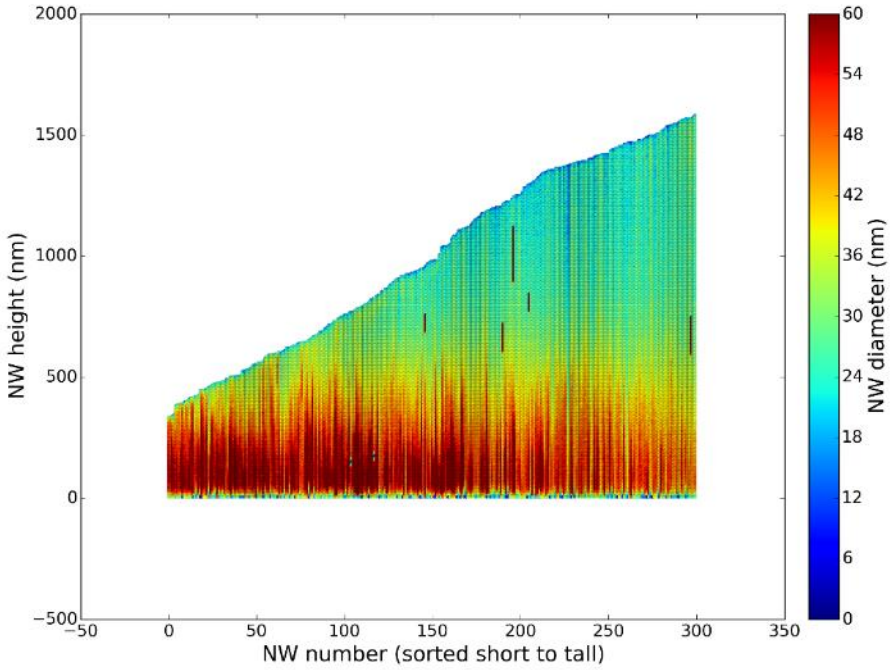

Figure 9.21: V/III flux ratio = 6, pitch = 360 nm.

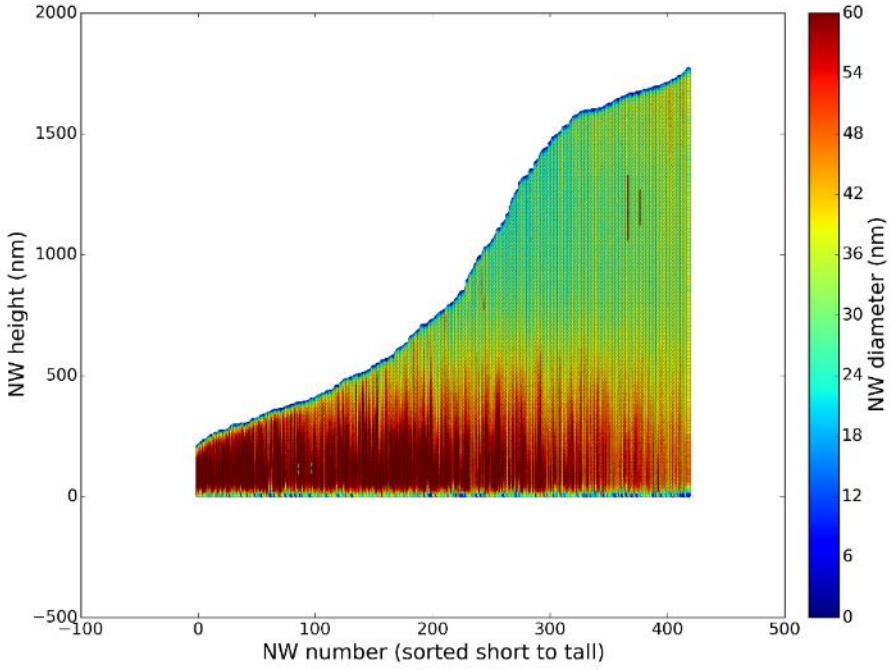

Figure 9.22: V/III flux ratio = 6, pitch = 440 nm.

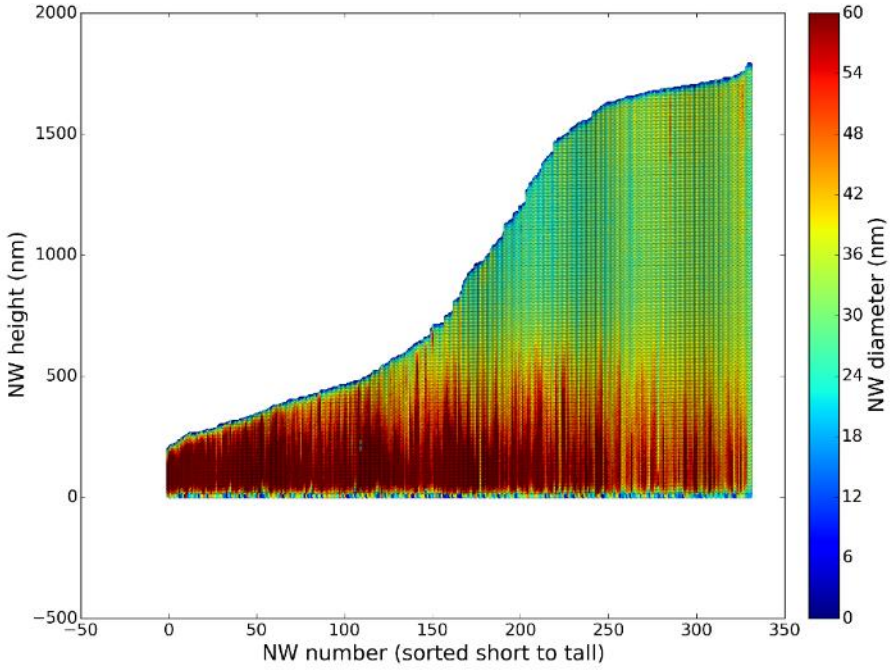

Figure 9.23: V/III flux ratio = 6, pitch = 520 nm.

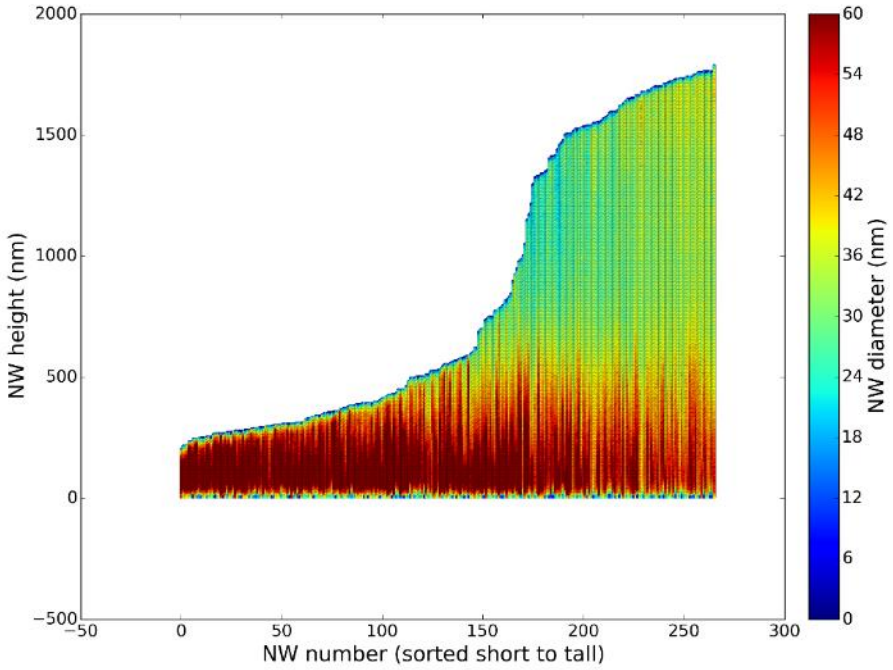

Figure 9.24: V/III flux ratio = 6, pitch = 600 nm.

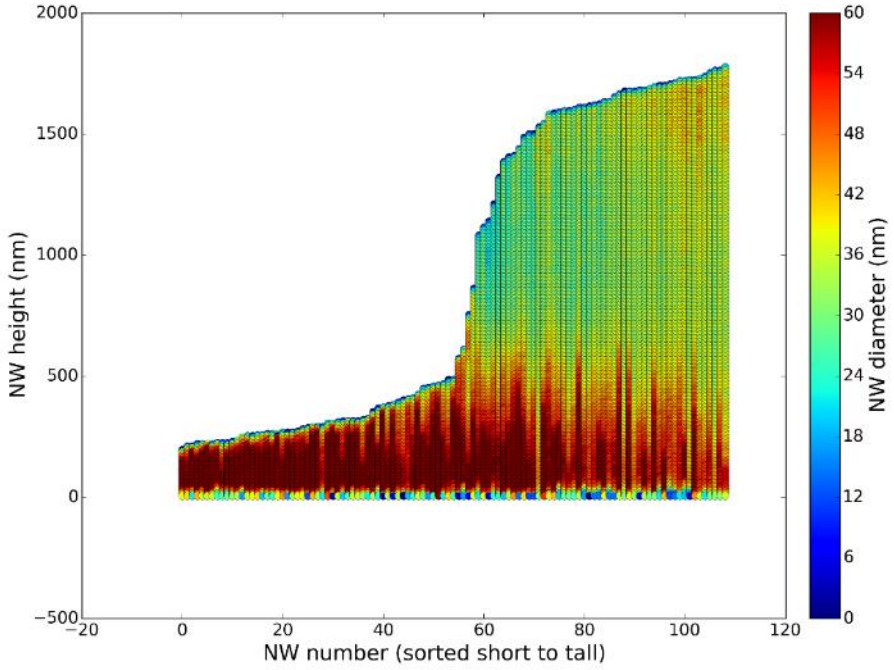

Figure 9.25: V/III flux ratio = 6, pitch = 1000 nm.